TAMPEREEN TEKNILLINEN YLIOPISTO
TAMPERE UNIVERSITY OF TECHNOLOGY

Léo Turquet

Manipulation and Verification of Longitudinal Electric Fields for Nonlinear Optical Microscopy

Julkaisu 1591 • Publication 1591

Tampere 2018

Tampereen teknillinen yliopisto. Julkaisu 1591
Tampere University of Technology. Publication 1591

Léo Turquet

Manipulation and Verification of Longitudinal Electric Fields for Nonlinear Optical Microscopy

Thesis for the degree of Doctor of Science in Technology to be presented with due permission for public examination and criticism in Sähkötalo Building, Auditorium SA203, at Tampere University of Technology, on the 16th of November 2018, at 12 noon.

Tampereen teknillinen yliopisto - Tampere University of Technology
Tampere 2018

Doctoral candidate: Léo Turquet
Laboratory of Photonics
Faculty of Natural Sciences
Tampere University of Technology
Finland

Supervisor: Prof. Martti Kauranen
Laboratory of Photonics
Faculty of Natural Sciences
Tampere University of Technology
Finland

Instructor: Dr. Godofredo Bautista
Laboratory of Photonics
Faculty of Natural Sciences
Tampere University of Technology
Finland

Pre-examiners: Prof. Cornelia Denz
Institute of Applied Physics
University of Münster
Germany

Prof. Kimani Toussaint
Department of Mechanical Science & Engineering
University of Illinois at Urbana-Champaign
USA

Opponent: Dr. Alexandre Bouhelier
Laboratoire Interdisciplinaire Carnot de Bourgogne
CNRS UMR 6303
University of Bourgogne Franche-Comté
France

ISBN 978-952-15-4242-8 (printed)
ISBN 978-952-15-4247-3 (PDF)
ISSN 1459-2045

ABSTRACT

Polarization, which is a fundamental property of light, describes the direction of oscillation of the electric component of the optical field. It is often assumed to be transverse to the direction of propagation of the optical wave. This is, for instance, the case for paraxial, i.e., collimated or weakly focused, laser beams. For non-paraxial, i.e., tightly focused, laser beams, however, the polarization of such beams shows a three-dimensional behavior as manifested by the generation of non-vanishing fields directed along the longitudinal direction, within the focal volume. These longitudinal fields have tremendous effects in the context of optical microscopy, and especially nonlinear microscopy because of the tensorial and symmetry dependence of the nonlinear response. So far, techniques able to precisely tailor the longitudinal field components at focus have relied on cumbersome setups and have seen their capabilities hindered by the lack of appropriate probes that can be used to unambiguously and directly detect such longitudinal fields.

This Thesis aims to meet this challenge and to provide new ways to control and probe longitudinal electric fields at the focus of a high numerical aperture objective. Relying on state-of-the-art spatial phase-shaping techniques of an incident optical field, we manage to control various parameters of the longitudinal electric field within the focal volume, including its transverse spatial distribution and depth of field, demonstrated by collection of second-harmonic generation from vertically aligned GaAs nanowires. The results presented in this Thesis suggest that the strength and spatial distribution of longitudinal fields can be generally controlled but also probed using our techniques. This work also opens up new opportunities for better understanding optical responses at the nanoscale and is expected to provide alternative imaging techniques for different types of nanostructures and possibly later for biological samples. Finally, our phase-shaping techniques provide alternative tools towards more advanced control of polarization in three-dimensions at focus.

PREFACE

The work presented in this Thesis was performed in the Nonlinear Optics group, which is part of the Laboratory of Photonics at Tampere University of Technology (TUT). My doctoral studies were funded mainly by the TUT Graduate School for which I am grateful. I joined the Laboratory of Photonics in 2014 for an internship in order to complete my Master's degree in Engineering started in Lannion (ENSSAT), France. The successful work and the unconditional trust given by Professor Martti Kauranen convinced me to apply for a doctoral position. Four years later, here we are.

I would like to sincerely thank Professor Martti Kauranen for the trust and constant availability, and for being a rather flawless supervisor who always asked the right questions. I am also very grateful to Dr. Godofredo Bautista for advising me since the beginning of my research. His dedicated work and knowledge significantly contributed to the quality of the work achieved in this Thesis. I would also like to thank Dr. Xiaorun Zang for the computational work and collaborators at Aalto University.

The friendly spirit reigning in the lab was also a good reason for me to pursue doctoral studies. In this view, I would like to thank the good fellas who welcomed me, including Caroline, Johan, Samu, Kalle, Piotr, rock-stars Jan and Kim, my road sidekick Mikko, and partners in crime Goëry and Juha. A special thank-you goes to my pal Antti, for the friendship and valuable off-work company. I would like to thank my dear friend Caleb for the good time spent in Finland, along with Kristen and Santiago, and for introducing me to the beauty of the United States. I do not forget my buddy José, who made these first years in Finland full of good memories. Special kisses go to Ida, for so many reasons. Finally, I would like to thank my loving parents and sisters for the unconditional support and for being my primary source of motivation.

"You miss 100% of the shots you don't take."

—Wayne Gretzky
—Michael Scott
—Léo Turquet

CONTENTS

Abstract iii

Preface v

List of symbols and abbreviations ix

List of publications xi

Author's contribution xiii

1. Introduction 1

    1.1 Aims and scope of this work 3

    1.2 Structure of the Thesis 4

2. Polarization and vector beams 5

    2.1 Wave equation 5

    2.2 States of polarization 7

    2.3 Generation and applications of vector beams 13

3. Tight focusing of vector beams 19

    3.1 Angular spectrum representation 19

    3.2 Tight focusing and longitudinal fields 20

    3.3 Tailoring and verification of electric field components at focus 28

4. Role of longitudinal fields in nonlinear optical microscopy 31

    4.1 Nonlinear wave equation 31

    4.2 Second-harmonic generation 32

    4.3 Vector beams in nonlinear microscopy 36

5. Manipulation and verification of longitudinal electric fields 41

    5.1 General setup 41

    5.2 Phase-shaping techniques 42

    5.3 Verification of longitudinal electric fields 47

6. Transverse distribution control of longitudinal electric fields 51
6.1 Experimental results 51
6.2 Discussion 54
7. Control of the depth of field of longitudinal electric fields 57
7.1 Experimental results 57
7.2 Discussion 62
8. Conclusions and outlook 65
References 67
Original papers 83
Paper I 85
Paper II 97
Paper III 107
Paper IV 115

LIST OF SYMBOLS AND ABBREVIATIONS

α	Relative phase between transverse electric field component
α_x, α_y	Phase of the transverse electric field components
$\boldsymbol{B}$	Magnetic flux density
β	Scaling parameter
c	Speed of light in vacuum
$\boldsymbol{D}$	Electric displacement
ϵ_0	Permittivity of vacuum
$\boldsymbol{E}$	Electric field
$\boldsymbol{E}_\infty$	Electric far-field
f_ω	Apodization
f_0	Filling factor
$\boldsymbol{H}$	Magnetic field
$\boldsymbol{J}$	Free current density
J_n	nth-order Bessel function
$\chi^{(n)}_{ijk}$	nth-order susceptibility
$\boldsymbol{k}$	Wave vector
k	Wave number
λ	Wavelength
$\boldsymbol{M}$	Magnetization
μ	Permeability of vacuum
n	Index of refraction
$\boldsymbol{P}$	Polarization
q	Complex beam parameter
$\boldsymbol{r}$	Position vector
ω	Angular frequency
ρ	Free charge density
R	Ratio between transverse electric field components
t	Time
φ	Gouy phase
w	Beam size
x, y, z	Cartesian coordinates
r, θ, ϕ	Spherical coordinates
ρ, ϕ, z	Cylindrical coordinates

∇	Gradient
$\nabla\cdot$	Divergence
$\nabla\times$	Curl
∇^2	Laplacian
$\|.\|$	Norm of a vector
$\tilde{.}$	Fast varying quantity in time
$\hat{.}$	Fourier transform
$\frac{\partial f}{\partial n}$	Derivative of function f with respect to n
3D	Three-dimension/Three-dimensional
AP	Azimuthally polarized
APBG	Azimuthally polarized Bessel Gauss
ASR	Angular spectrum representation
BG	Bessel-Gaussian
CARS	Coherent anti-Stokes Raman scattering
FWHM	Full width at half maximum
HG_{mn}	Hermite-Gaussian mode of order mn
LC	Liquid-crystal
LCD	Liquid-crystal display
LG_{lp}	Laguerre-Gaussian mode of order lp
LP	Linearly polarized
LPBG	Linearly polarized Bessel Gauss
NA	Numerical aperture
RP	Radially polarized
RPBG	Radially polarized Bessel Gauss
SEM	Scanning electron microscopy
SHG	Second-harmonic generation
SLM	Spatial light modulator
NSOM	Near-field scanning optical microscopy
SOP	State of polarization
TEM	Transmission electron microscopy
THG	Third-harmonic generation
TPF	Two-photon excited fluorescence
TPL	Two-photon excited luminescence

LIST OF PUBLICATIONS

I. Léo Turquet, Joona-Pekko Kakko, Xiaorun Zang, Liisa Naskali, Lasse Karvonen, Hua Jiang, Teppo Huhtio, Esko Kauppinen, Harri Lipsanen, Martti Kauranen, and Godofredo Bautista, "Tailorable second-harmonic generation from an individual nanowire using spatially phase-shaped beams," *Laser & Photonics Reviews*, vol. 11, no. 1, p. 1600175, 2017

II. Léo Turquet, Joona-Pekko Kakko, Hua Jiang, Tero J. Isotalo, Teppo Huhtio, Tapio Niemi, Esko Kauppinen, Harri Lipsanen, Martti Kauranen, and Godofredo Bautista, "Nonlinear imaging of nanostructures using beams with binary phase modulation," *Optics Express*, vol. 25, no. 9, pp. 10441-10448, 2017

III. Léo Turquet, Joona-Pekko Kakko, Lasse Karvonen, Hua Jiang, Esko Kauppinen, Harri Lipsanen, Martti Kauranen and Godofredo Bautista, "Probing the longitudinal electric field of Bessel beams using second-harmonic generation from nano-objects, " *Journal of Optics*, vol. 19, no. 8, p. 084011, 2017

IV. Léo Turquet, Xiaorun Zang, Joona-Pekko Kakko, Harri Lipsanen, Godofredo Bautista, and Martti Kauranen,"Demonstration of longitudinally polarized optical needles, " *Optics Express*, vol. 26, no. 21, pp. 27572-27584, 2018 .

AUTHOR'S CONTRIBUTION

This Thesis is based on four original publications where the author was significantly involved, all related to the control and probing of longitudinal electric fields as demonstrated by second-harmonic generation (SHG) from GaAs nanowires. The author of this Thesis contributed significantly to the experiments and to the reporting of the work. More detailed contributions are provided below:

Paper I: This paper introduces the phase-shaping scheme for a Hermite-Gaussian 10 (HG_{10}) mode to control the spatial distribution and strength of the longitudinal electric field distribution at the focus of a microscope objective. The scheme was verified by collecting SHG from single GaAs nanowires. The author and G. Bautista designed and built the experimental setup. The author collected the data and G. Bautista provided additional data in the supplementary material. X. Zang performed the numerical simulations for the focal fields using a custom algorithm. GaAs nanowires were grown and characterized by J.-P. Kakko and colleagues at Aalto University. All co-authors participated to the writing of the manuscript, with significant contributions from the author. G. Bautista and M. Kauranen supervised the work.

Paper II: This paper deals with binary and local phase-shaping of an HG_{10} mode for controlling the longitudinal electric field distribution at the focus of a microscope objective. The scheme was verified by collecting SHG from single GaAs nanowires. The author and G. Bautista proposed and designed the setup. The author built the experimental setup, collected and analyzed the data. T. J. Isotalo and T. Niemi designed and built the phase plate used for generating the HG_{10} mode. GaAs nanowires were grown and characterized by J.-P. Kakko and colleagues at Aalto University. All authors contributed to the writing of the manuscript, with significant contributions from the author. G. Bautista and M. Kauranen supervised the work.

Paper III: This paper focuses on the generation of a linearly polarized Bessel Gauss (LPBG) beams for controlling the depth of field of the longitudinal field at the focus of a microscope objective verified by collection of SHG from single GaAs nanowires. The author and G. Bautista proposed and designed the setup. The author built the experimental setup, collected, and analyzed the data. GaAs nanowires were grown by J.-P. Kakko at Aalto University. All authors contributed to the writing of

the manuscript, with significant contributions from the author, and co-authors G. Bautista and M. Kauranen.

Paper IV: This paper demonstrates experimentally the generation of longitudinally polarized optical needles, using radially polarized Bessel Gauss (RPBG) beams, verified by collection of SHG from single GaAs nanowires. The author and G. Bautista proposed and designed the setup. The author built the experimental setup, collected, and analyzed the data. X. Zang performed the numerical simulations for the focal fields using a custom algorithm. GaAs nanowires were grown and characterized by J.-P. Kakko and colleagues at Aalto University. All authors contributed to the writing of the manuscript, with significant contributions from the author. G. Bautista and M. Kauranen supervised the work.

1. INTRODUCTION

Among all the fundamental properties of light, polarization has often appeared as the ugly duckling, neglected in front of other parameters like intensity and wavelength. A majority of the existing light sources indeed emit unpolarized light, that is to say, the direction of oscillation of the electric field is random in time. In addition, this direction does not affect the total intensity perceived by conventional detectors or the human eye. However, whenever light is reflected or transmitted through a material, it may acquire a certain degree of polarization. Some materials can even absorb, reflect, or discriminate specific states of polarization (SOPs). Many innovations have emerged using polarization-sensitive materials: television, computer and smart-phone displays, polarized sunglasses, camera filters, or even three-dimensional (3D) cinema technology, all exploit the polarizing properties of various materials for the control of light intensity. Polarization is also a rich source of information itself. Optical microscopy has, for instance, greatly benefited from the study and control of polarized light sources and subsequent polarization analysis of the collected signals. In fact, polarized white-light microscopy has been commonly used in geology, materials science, biology and forensics to identify anisotropic regions of microscopic specimen structures [1].

The introduction of laser as excitation source has had a tremendous impact on light microscopy, especially through the study of novel linear and nonlinear optical phenomena. The high density of photons at the focus of a laser beam has enabled, for instance, various nonlinear effects to be the main source of contrast for label-free imaging and characterization of biological specimens and non-biological, i.e., artificial and subwavelength-sized, nano-objects [2–6]. Due to the tensorial character of nonlinear effects [7], responses from materials can be strongly influenced by the material crystal structure, composition and geometry of the material, and the polarization structure of the impinging light.

The propagation of light is often described by solving the scalar Helmholtz wave equation that can be used to describe the propagation of a linearly polarized (LP) input field or one component of an arbitrary vector field. However, when polarization is of major concern, one needs to find the solutions of the vector Helmholtz equation to describe the propagation of optical field where the whole transverse electric field is considered [8]. Such optical fields, solutions of the vector Helmholtz equation and possessing a spatially more complicated polarization, are called vector beams. This description is important especially in microscopy where vector beams plays a major role when focused by a high numerical aperture (NA) objective. Indeed, under strong focusing, and depending on the polarization of the input beam and focusing conditions, a significant part of the electric field might be directed along axes which are orthogonal to the polarization of the input beam, called longitudinal direction [9–13]. Therefore, the polarization of a strongly focused beam shows a 3D behavior, with spatial distributions and strengths dependent on the input polarization.

Common SOPs like linear or circular polarizations have been used in nonlinear microscopy to obtain new information about various objects or biological entities [14–22]. However, such SOPs have quickly found their limitations in terms of imaging capabilities, considering that linearly and circularly polarized light have only limited uses for sample architectures with increasing complexity. This explains the recent interest given to the generation of laser beams possessing more exotic SOPs, and that have already enabled further breakthroughs in linear [23–26] and nonlinear microscopy [27–31]. Due to the spatially varying SOP across the beam section, vector beams allow for more sensitive characterization of nano-objects [30, 32, 33]. Then, due to possible strong focusing conditions, some nano-structures and even biological entities can be really sensitive to strong longitudinal fields and therefore the contrast in nonlinear microscopy can be further enhanced [34–36].

It appears now obvious that controlling and verifying polarization at focus, and especially longitudinal electric fields, is important especially in the context of nonlinear microscopy. The polarization at focus being closely linked to the amplitude, phase, and polarization of the input beam, research has been aiming towards better and more local control of such parameters to obtain designed 3D focal fields [37–42]. Such techniques have, however, seen their capabilities hindered by the complexity and often indirect methods available for characterizing transverse and longitudinal electric field components at focus [23, 43–47].

As of today, better control of 3D polarization at focus and methods to independently and directly probe focal electric field components seems crucial to foster further advances in this field. This Thesis is in line with these aspects and aims to bring alternative techniques for the control but also verification of longitudinal electric fields at focus.

1.1 Aims and scope of this work

This Thesis aims to provide ways to tailor the spatial distribution and strength of longitudinal electric fields at the focus of a microscope objective and to verify their properties using SHG microscopy from single nano-objects. Using state-of-the-art beam shaping devices, we tailor the excitation beam and image nano-objects that are mainly sensitive to longitudinal fields in the focal volume.

SHG is a process extremely sensitive to the symmetry properties of the material or the geometry of the nano-object imaged, but also highly dependent on the polarization of the excitation beam at focus. Colleagues at the Laboratory of Photonics started first investigating the SHG properties of vertically aligned GaAs nanowires using common vector beams. They noticed that the distribution of SHG from these nanowires was highly dependent on the input beam polarization. By comparing SHG using beams showing weak or strong longitudinal electric field components at focus, they noticed the strong preference of such nanowires for longitudinal field excitation.

From these experiments originated the goal to develop techniques suitable for controlling the polarization at focus, especially its longitudinal component at focus. The 3D polarization at focus being dependent on the input beam amplitude, phase, and polarization, we investigated ways to control parameters, that is to say, the strength and spatial distribution in 3D, of longitudinal electric fields through control of the input beam. With a view to develop techniques capable of providing a high degree of precision and programmablility, our interest was drawn to spatial phase shaping of common vector beams using, for instance, spatial light modulators (SLMs). We would then directly probe the longitudinal electric field in 3D using SHG from vertically aligned GaAs nanowires.

The first idea was to apply an additional phase from 0 to 2π on one lobe of an HG_{10} mode to control the distribution of the longitudinal field at focus in the transverse

plane. The second idea involved a similar scheme but using π phase delay over only part of one lobe of the HG_{10} mode. In order to extend our work to 3D, we investigated the properties of vector Bessel beams to tune the extent of the longitudinal electric field along the overall direction of propagation of the beam.

1.2 Structure of the Thesis

This Thesis is composed of 8 chapters. An introduction and three chapters of theoretical background give a general overview of the topic, required to understand the work. The methods used in this work are presented in Chapter 5 and the results are separated into Chapters 6 and 7. Conclusions are presented in Chapter 8.

In Chapter 2, an introduction to polarization and vector beams is given. In particular, the state-of-the-art techniques for generating and manipulating vector beams are provided, especially focusing on the ones used in this Thesis. The most common applications of such vector beams are also described. We then introduce in Chapter 3 the tools used to describe the tight focusing of vector beams. In this context, the existing techniques used to control and probe focal electric-field components are presented. An overview of SHG and the importance of vector beams for nonlinear microscopy is highlighted in Chapter 4.

Chapter 5 describes the phase-shaping techniques used to control but also to verify the spatial distribution of longitudinal electric fields at the focus of a microscope objective. After introducing the general experimental setup, we detail the phase-shaping techniques used for the control of longitudinal electric fields. The verification using SHG signals from vertically aligned GaAs nanowires is then presented.

Chapter 6 presents the results obtained by spatially phase-shaping a LP HG_{10} mode using a SLM. After confirming the distribution of longitudinal electric fields of well-known vector beams, we present the results obtained by gradually tuning the phase of one lobe of an HG_{10} mode or by applying sections of π additional phase over the same lobe. The results are then discussed. Chapter 7 is then dedicated to the investigation of the longitudinal electric fields of vector Bessel beams in order to gain control over the depth of field of longitudinal electric fields. We first report on the extended longitudinal electric fields observed using a LPBG. We then generate an optical needle using an RPBG beam. The results are then discussed.

Chapter 8 provides a general summary and outlook of the work.

2. POLARIZATION AND VECTOR BEAMS

Manipulation of longitudinal fields at the focus of a microscope objective requires the introduction of essential background information. In this Chapter, the concept of polarization and the equations ruling the propagation of light are first presented. They form the basis for introducing vector beams and their known applications.

2.1 Wave equation

The propagation of light, as an electromagnetic wave, can be described using a set of equations, known as **Maxwell's equations**. First presented by James Clerk Maxwell [48] in 1865, they were formulated in a more condensed form by Oliver Heaviside starting in 1884 [49]. These equations take the following form in SI units using the notation of Boyd's book [7]:

$$\nabla \cdot \tilde{\boldsymbol{D}} = \tilde{\rho} \tag{2.1}$$

$$\nabla \cdot \tilde{\boldsymbol{B}} = 0 \tag{2.2}$$

$$\nabla \times \tilde{\boldsymbol{E}} = -\frac{\partial \tilde{\boldsymbol{B}}}{\partial t} \tag{2.3}$$

$$\nabla \times \tilde{\boldsymbol{H}} = \frac{\partial \tilde{\boldsymbol{D}}}{\partial t} + \tilde{\boldsymbol{J}} \tag{2.4}$$

where $\tilde{\boldsymbol{E}}$ and $\tilde{\boldsymbol{H}}$ represent respectively the electric and magnetic field of light, $\tilde{\boldsymbol{D}}$ and $\tilde{\boldsymbol{B}}$, respectively, stand for the electric displacement field and magnetic-flux density. The other quantities, $\tilde{\rho}$ and $\tilde{\boldsymbol{J}}$, respectively, stand for the free charge and the free current density and are therefore related to the medium in which light propagates. In this Thesis, the symbol $\tilde{\cdot}$ represents a quantity varying rapidly in time. Two constitutive relations are useful to link the electric and magnetic quantities mentioned

above:

$$\tilde{\boldsymbol{D}} = \epsilon_0 \tilde{\boldsymbol{E}} + \tilde{\boldsymbol{P}} \tag{2.5}$$

$$\tilde{\boldsymbol{B}} = \mu_0(\tilde{\boldsymbol{H}} + \tilde{\boldsymbol{M}}) \tag{2.6}$$

where ϵ_0 and μ_0, respectively, represent the scalar permittivity and permeability of vacuum and $\tilde{\boldsymbol{P}}$ and $\tilde{\boldsymbol{M}}$, respectively, represent the induced polarization and magnetization. In the context of our work, we are first interested in the description of light beams propagating in free space. Their interaction with a nonlinear medium will be described later. Therefore, we can consider that neither free charges nor current densities are involved:

$$\tilde{\rho} = 0 \tag{2.7}$$

$$\tilde{\boldsymbol{J}} = 0 \tag{2.8}$$

We can also neglect induced polarization or magnetization in free space:

$$\tilde{\boldsymbol{P}} = 0 \tag{2.9}$$

$$\tilde{\boldsymbol{M}} = 0 \tag{2.10}$$

From this point, we can modify Maxwell's equations to retrieve the equation governing the propagation of light in free space. First, we take the curl of Eq.(2.3). By interchanging the order of space and time derivatives, we can then plug the right side of Eq.(2.4) into Eq.(2.3) to obtain:

$$\nabla \times (\nabla \times \tilde{\boldsymbol{E}}) + \frac{1}{c^2}\frac{\partial^2 \tilde{\boldsymbol{E}}}{\partial t^2} = 0 \tag{2.11}$$

where $c = \frac{1}{\sqrt{\epsilon_0 \mu_0}}$ is the speed of light in vacuum. This equation is a general formulation of the electromagnetic wave equation in free space. Now, we can use the identity $\nabla \times (\nabla \times \tilde{\boldsymbol{E}}) = \nabla(\nabla \cdot \tilde{\boldsymbol{E}}) - \nabla^2 \tilde{\boldsymbol{E}}$. The first term on the right side cancels using Eqs. 2.1, 2.5, 2.7, and 2.9. Therefore, Eq.(2.11) can be expressed in a simplified form:

$$\nabla^2 \tilde{\boldsymbol{E}} - \frac{1}{c^2}\frac{\partial^2 \tilde{\boldsymbol{E}}}{\partial t^2} = 0 \tag{2.12}$$

Common solutions of this equation are transverse plane waves and can be formulated as follows:

$$\tilde{\boldsymbol{E}}(r,t) = \boldsymbol{E_0}(r) e^{i(\boldsymbol{k}\cdot\boldsymbol{r} - \omega t)} \tag{2.13}$$

with ω being the frequency of the optical wave and $\boldsymbol{k}$ being the wave vector and $\boldsymbol{r}$ the position vector. In addition to this, $|\boldsymbol{k}| = k = \frac{\omega}{c} = \frac{2\pi}{\lambda}$ represents the magnitude of wave vector for plane waves in free space and is the scalar wave number. In Cartesian coordinates, for a plane wave propagating in the positive z direction, Eq.(2.13) takes the following form:

$$\tilde{\boldsymbol{E}}(z,t) = \boldsymbol{E_0}(z)e^{i(kz-\omega t)} \tag{2.14}$$

The electric field $\boldsymbol{E_0}$ is defined by its amplitude distribution but also by its oscillation direction, which is represented by polarization.

2.2 States of polarization

2.2.1 Fundamentals of polarization

The direction of oscillation of the electric field of light is called polarization. If this direction of oscillation fluctuates randomly in time, light is said to be unpolarized. This is the case for sunlight or light coming from a basic incandescent light bulb. In this Thesis, we use lasers that often have polarized beams as their outputs. Using the fact that the electric field is oscillating in the plane transverse (xy) to the direction of propagation (z) and the mathematical description of a plane wave in Eq.(2.14), we can decompose the electric field vector into its x and y components:

$$\tilde{\boldsymbol{E}}(z,t) = \begin{pmatrix} \tilde{E}_x(z,t) \\ \tilde{E}_y(z,t) \\ 0 \end{pmatrix} = \begin{pmatrix} E_{0x}e^{i(kz-\omega t+\alpha_x)} \\ E_{0y}e^{i(kz-\omega t+\alpha_y)} \\ 0 \end{pmatrix} = \begin{pmatrix} E_{0x}e^{i(\alpha_x)} \\ E_{0y}e^{i(\alpha_y)} \\ 0 \end{pmatrix} e^{i(kz-\omega t)} \tag{2.15}$$

with α_x and α_y, respectively, representing the phase of the x and y components of the electric field. This set of equations represents the basis of the **Jones** formalism, with $\begin{pmatrix} E_{0x}e^{i(\alpha_x)} \\ E_{0y}e^{i(\alpha_y)} \end{pmatrix}$ being known as the **Jones vector**. Besides being a powerful tool for treating fully polarized light, this representation helps to show the important parameters at stake when dealing with polarized optical beams. We can see that the **amplitude**, the **phase** and the **polarization** of light are intertwined parameters which define the vectorial nature of light. This means that modifying the amplitude and/or phase of one of the transverse components will change the resulting vector

direction and magnitude of the total electric field, that is to say, the polarization. Based on this, it seems that spatially phase shaping an optical beam can constitute an appropriate way to control polarization, and further to control longitudinal fields at the focus of a microscope objective, as will be shown later. We can also mention that another formalism exists to represent the polarization of light, called *Stokes parameters* [50]. Compared to the Jones formalism, the Stokes parameters are a set of intensity values determined experimentally that extend to partially coherent and partially polarized light. In the first part of this Thesis, we deal with collimated and fully polarized beams propagating in free space. The Jones formalism is then interesting for describing the polarization of our laser beam, as it describes directly the parameters that we are going to manipulate later and already mentioned before: the Cartesian electric field components and their respective amplitude and phase.

Depending on the ratio $R = \frac{E_{0x}}{E_{0y}}$ and the relative phase $\alpha = \alpha_y - \alpha_x$ between the transverse components of the electric field, a plane wave can possess three different types of polarization: **elliptical**, **linear**, or **circular**. It is important to note that linearly and circularly polarized light are special cases of the general case of elliptically polarized light. Let us summarize the three cases :

- If $\alpha = 0$, then light is *linearly polarized* (LP). The ratio R determines then the direction of oscillation. For instance, if $R = 1$, that is to say $E_{0x} = E_{0y}$, light is LP at 45° with respect to x axis. If $R = -1$, that is to say $E_{0x} = -E_{0y}$, light is LP at 135° with respect to x axis.
- If $\alpha = \delta\pi/2 + 2\eta\pi$, ($\delta = \pm 1$ and $\eta \in \mathbb{Z}$) and $R = 1$, that is to say $E_{0x} = E_{0y}$, then light is *circularly polarized*. Here, the sign of δ determines the handedness of polarization, which tells whether the electric field rotates clockwise or counter-clockwise over propagation due to the vector summation of E_{0x} and E_{0y} to form E. If the the electric field rotates clockwise, the polarization is right-hand circular and if the electric field rotates counter-clockwise, the polarization is left-hand circular.
- In the most general case, if α and R are constant values over time but do not fall within the two previous cases, light is *elliptically polarized*. Here again, depending on the phase difference α, light can be right-hand or left-hand elliptically polarized.

Such SOPs are represented in Fig. 2.1 and can be manipulated using specific optical

components. Most of them use birefringent crystals where transverse components of the electric field experience different indices of refraction. Linear *polarizers* can be used to convert unpolarized light into LP light. They can also be used to control the power of a LP laser beam according to Malus' law. Wave plates, like *half-wave plates* or *quarter-wave plates*, use birefringence to rotate the polarization of LP light or to transform LP light into circularly or elliptically polarized light.

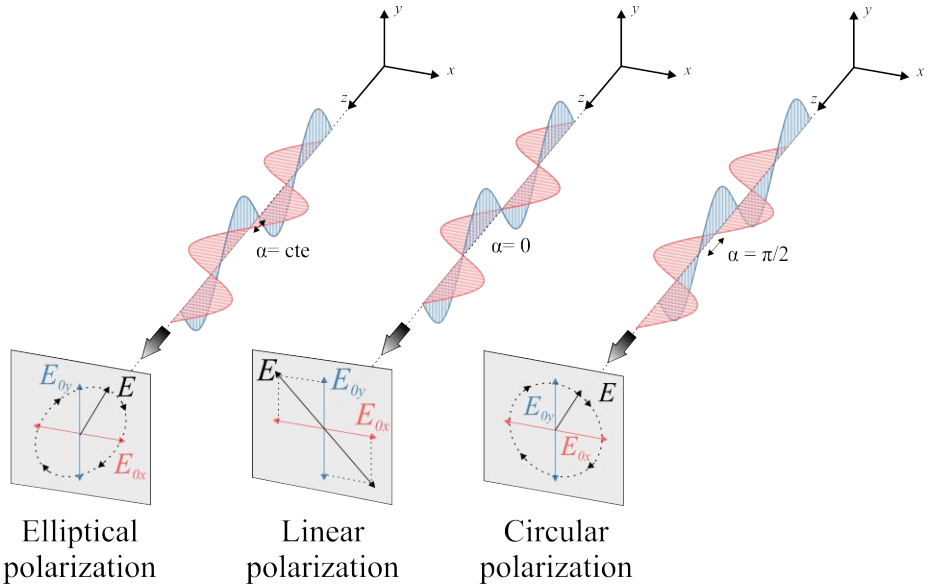

Figure 2.1 *Schematic of E_x and E_y forming elliptical, linear, or circular polarization.*

2.2.2 Homogeneous states of polarization

In free space, the typical beams having spatially homogeneous, i.e., uniform, polarization are obtained by solving the scalar **Helmholtz** equation:

$$(\nabla^2 + k^2)E = 0 \tag{2.16}$$

This equation is directly linked to the wave equation in free space (see Eq 2.12) and is derived by applying the technique of separation of variables over the electric field expression. Here, it is considered that the state of polarization does not depend on the observation point over the beam cross-section, hence the use of the term spatially homogeneous polarization.

Assuming propagation along z direction and for a finite beam-like paraxial solution, the general form of the electric field for homogeneous polarization in Cartesian

coordinates takes the following form:

$$E(x,y,z,t) = E_0(x,y,z)e^{i(kz-\omega t)} \tag{2.17}$$

The goal is now to determine the form of $E_0(x,y,z)$. A first family of **modes** can be obtained by applying the slowly varying envelope approximation ($\frac{\partial^2 E_0}{\partial z^2} \ll k^2 E_0$ and $\frac{\partial^2 E_0}{\partial z^2} \ll k\frac{\partial E_0}{\partial z}$) and by separating the variables x and y. The solutions obtained are the so-called **Hermite-Gaussian HG_{mn}** modes and take the following mathematical form [51]:

$$E_0(x,y,z) = A_0 H_m\left(\sqrt{2}\frac{x}{w(z)}\right) H_n\left(\sqrt{2}\frac{y}{w(z)}\right)\frac{w_0}{w(z)}e^{-i\varphi_{mn}(z)}e^{i\frac{k}{2q(z)}r^2} \tag{2.18}$$

with $H_m(x)$ known as the Hermite polynomials that obey the following differential equation:

$$\frac{\mathrm{d}^2 H_m}{\mathrm{d}x^2} - 2x\frac{\mathrm{d}H_m}{\mathrm{d}x} + 2mH_m = 0 \tag{2.19}$$

In addition, A_0 represents the amplitude of the electric field, $w(z)$ the beam size, w_0 the beam size at waist, $q(z) = z - iz_0$ the complex beam parameter and $\varphi_{mn}(z) = (m+n+1)\arctan(z/z_0)$ the Gouy phase with $z_0 = \pi w_0^2/\lambda$ being the Rayleigh range. When $m = n = 0$, we end up with the fundamental Gaussian beam HG_{00} which is used to approximate the spatial intensity distribution of the fundamental mode of a laser output:

$$E_0(r,z) = A_0\frac{w_0}{w(z)}e^{-i\varphi(z)}e^{i\frac{k}{2q(z)}r^2} \tag{2.20}$$

and we have $\varphi(z) = \arctan(z/z_0)$ for the Gouy phase. Such modes will be used in the two first publications included in this Thesis, that is to say, **Paper I** and **Paper II**.

In the cylindrical coordinate system, the electric field can be formulated by:

$$E(r,\phi,z,t) = E_0(r,\phi,z)e^{i(kz-\omega t)} \tag{2.21}$$

and by solving the Helmholtz equation similarly as for HG modes, we obtain a new family of solutions known as **Laguerre-Gaussian LG_{pl}** modes, which take the following form:

$$E_0(r,\phi,z) = A_0\left(\sqrt{2}\frac{r}{w(z)}\right)^l L_p^l\left(2\frac{r^2}{w(z)^2}\right)\frac{w_0}{w(z)}e^{-i\varphi_{pl}(z)}e^{i\frac{k}{2q(z)}r^2}e^{il\phi} \tag{2.22}$$

with $\varphi_{pl}(z) = (2p + l + 1)\arctan(z/z_0)$ the Gouy phase shift and $L_p^l(x)$ representing the Laguerre polynomials which satisfy the following differential equation:

$$x\frac{\mathrm{d}^2 L_p^l}{\mathrm{d}x^2} - (l + 1 - x)\frac{\mathrm{d}L_p^l}{\mathrm{d}x} + pL_p^l = 0 \tag{2.23}$$

Here again, for $l = p = 0$, we recover the well-known fundamental Gaussian beam.

A last family of rotationally symmetric modes that does not depend on the azimuthal angle ϕ can be obtained by solving the scalar Helmholtz equation. They are known as **Bessel-Gaussian *BG*** modes and are expressed as follows:

$$E_0(r, z) = A_0\frac{w_0}{w(z)}e^{-i\varphi(z)}e^{i\frac{k}{2q(z)}r^2}J_0\left(\frac{\beta r}{1 + iz/z_0}\right)e^{-\frac{\beta^2 z/(2k)}{1+iz/z_0}} \tag{2.24}$$

with $J_0(x)$ the zeroth-order Bessel function of the first kind and β a constant scale parameter. For $\beta = 0$, the solution reduces to the expression of the fundamental Gaussian beam. Such beam will be created and used in **Paper III**. Overall, several of the mode families mentioned above will be used in this Thesis and a representation of such beams can be found in Fig. 2.2.

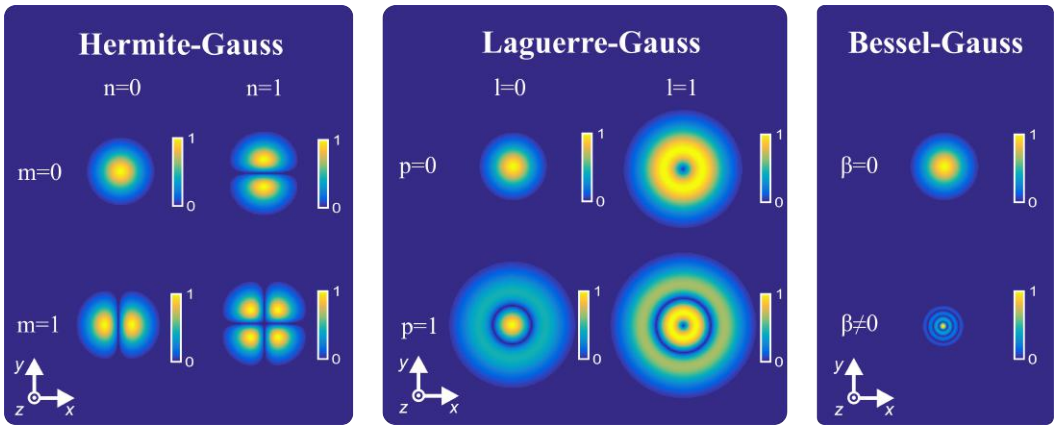

***Figure** 2.2 Representations of HG, LG and BG modes of lower orders.*

2.2.3 Inhomogeneous states of polarization

The previous section presented the different beam profiles emerging from solving the scalar Helmholtz equation with no consideration for inhomogeneous polarization across the beam section. When polarization is a crucial parameter, like in this Thesis, it has to be taken into account in the electric field description and in the

wave equation. Therefore, the full vector wave equation needs to be considered:

$$\nabla \times (\nabla \times \boldsymbol{E}) - k^2 \boldsymbol{E} = 0 \tag{2.25}$$

For simplicity and considering the type of beams to be manipulated in this Thesis, we will focus on beams with circularly symmetric SOPs that are called **cylindrical vector beams**. For instance, a beam with a polarization following the azimuthal direction should take the form:

$$\boldsymbol{E}(r,z) = E_0(r,z)e^{i(kz-\omega t)}\boldsymbol{e}_\phi \tag{2.26}$$

where $\boldsymbol{e}_\phi$ is the unit vector of the electric field, which here follows the azimuthal direction about the beam center. By substituting Eq.(2.26) into Eq.(2.25) and by again applying the paraxial and slowly varying envelope approximation, an **azimuthally polarized** (AP) beam then takes the following form:

$$\boldsymbol{E}(r,z) = A_0 J_1\left(\frac{\beta r}{1+iz/z_0}\right) e^{-\frac{i\beta^2 z/(2k)}{1+iz/z_0}} HG_{00}(r,z)e^{i(kz-\omega t)}\boldsymbol{e}_\phi \tag{2.27}$$

where $HG_{00}(r,z)$ represents the fundamental Gaussian beam, whose expression can be found in Eq.(2.20), and $J_1(x)$ is the first-order Bessel function of the first kind. Similarly, a solution where the polarization follows the radial direction can be found where the electric field $\boldsymbol{E}(r,z)$ oscillates in the radial direction, forming a **radially polarized** (RP) beam:

$$\boldsymbol{E}(r,z) = A_0 J_1\left(\frac{\beta r}{1+iz/z_0}\right) e^{-\frac{i\beta^2 z/(2k)}{1+iz/z_0}} HG_{00}(r,z)e^{i(kz-\omega t)}\boldsymbol{e}_r \tag{2.28}$$

where $\boldsymbol{e}_r$ represents the unit vector of the electric field in the radial direction.

It is worth noting here that such solutions correspond to **vector BG beams**, term used for beams used in **Paper IV**. They are the closest approximations and physically achievable beam-like solutions of vector Bessel beams. Due to the restriction on polarization (azimuthal or radial), Eq.(2.27) and Eq.(2.28) contain the first order J_1 Bessel function, whereas Eq.(2.24) contains the zeroth-order J_0 Bessel function. This fact explains the bright spot on the optical axis for a BG beam and the dark spot on the optical axis for an azimuthally polarized Bessel Gauss (APBG) and RPBG beam. Another interesting point is the fact that when the parameter β is very small, for instance for beams with large cross sections, the AP and RP beams

as we usually know them are approximated by a LG_{01} intensity distribution and are often called AP and RP doughnut beam due to their doughnut-shaped intensity distributions, as seen on Fig. 2.3. It is also possible to show that AP and RP beams can be expressed as a superposition of homogeneous SOPs using Eqs. 2.18 and 2.22:

$$\boldsymbol{E}_r = HG_{10}\boldsymbol{e}_x + HG_{01}\boldsymbol{e}_y \tag{2.29}$$

$$\boldsymbol{E}_\phi = HG_{01}\boldsymbol{e}_x + HG_{10}\boldsymbol{e}_y \tag{2.30}$$

where $\boldsymbol{E}_r$ and $\boldsymbol{E}_\phi$ represent, respectively, RP and AP electric fields and $\boldsymbol{e}_x$ and $\boldsymbol{e}_y$ the unit transverse Cartesian vectors. This superposition appears in Fig. 2.3. The above representation of AP and RP beams is interesting because it suggests that collinearly interfering HG_{10} and HG_{01} modes can be used to generate RP or AP beams [52]. It also indicates that HG_{10} and HG_{01} modes can be obtained straightforwardly by putting a linear polarizer (analyzer) after an RP or AP beam.

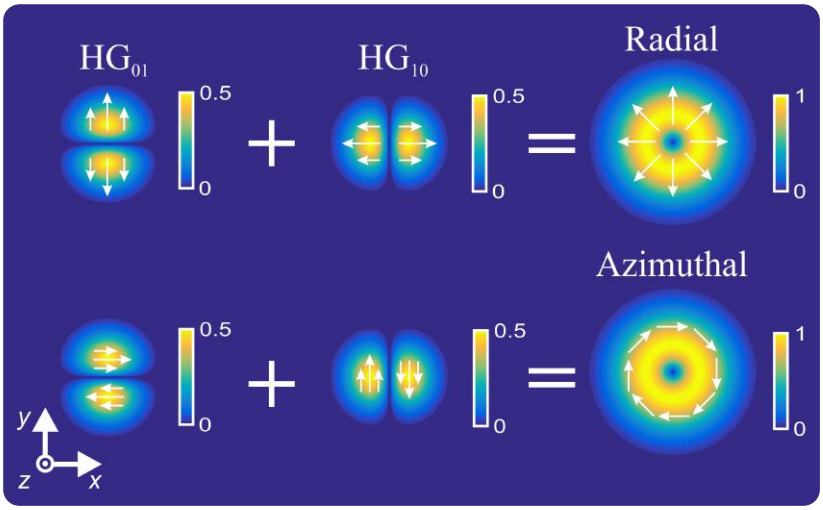

***Figure** 2.3 Formation of RP and AP beams obtained by superposition of orthogonally polarized HG modes. White arrows represent the instantaneous electric vector fields.*

2.3 Generation and applications of vector beams

In this Section, we shall present the existing techniques used to generate vector beams. We shall especially focus on the ones used in this Thesis that are cylindrical vector beams and vector Bessel beams. However, it is important to mention that several of the techniques mentioned below can achieve the generation of more exotic vector beams or vector fields, the latter not being initially beam-like solutions of the

vector Helmholtz equation. Many vector fields can, however, become vector beams through spatial filtering or in propagation [53].

2.3.1 Common vector beams

There are nowadays various ways to generate cylindrical vector beams. They can be categorized into two groups: active and passive methods. Active methods consist of generating vector beams already in the laser cavity, and are therefore called intra-cavity techniques [51, 54–59]. Due to the fact that additional optical components need to be placed within the laser cavity, active methods cannot be easily implemented and are therefore not commonly used for vector beam generation. Passive techniques have been more often used as they allow for the conversion of the common Gaussian output beam of a laser to a more exotic form of vector beam. Once again, passive methods are nowadays various, but only a few are regularly implemented in optical setups [60–64].

Among the techniques available for generating cylindrical vector beams, or more exotic vector fields, one can also make the distinction between interferometric and non-interferometric techniques. Interferometric techniques were developed first to generate vector beams because they often rely on the interference of low-order modes with homogeneous polarizations [52, 65–69]. Reliance on interference, however, is a source of instabilities within an optical setup. Moreover, the versatility of such techniques might be limited. However, such configurations remain low-cost and efficient, and can possibly be combined with more advanced beam shaping devices.

Non-interferometric techniques are often favored over the interferometric ones, because of their stability and versatility, even if they usually require more expensive devices. They also appear to be often more compact systems. The first method, already commercially available and also used in this Thesis, consists of locally rotating the state of polarization of a LP input beam using twisted nematic liquid crystal (LC) molecules [60, 70]. The latter, enclosed between two linearly and circularly rubbed plates, will locally rotate the state of polarization of the input beam. Because of the combination of linear and circular symmetry, the LC cell is called a θ cell. The working principle of this device is based on the fact that in conventional twisted LC devices with a twist angle α between entrance and exit alignment, the input LP light, which is oriented parallel or perpendicular to the rubbing direction of the first alignment plate, is rotated by the same twist angle α. Depending on

whether this input beam is horizontally or vertically polarized, the output beam will be azimuthally or radially polarized. Such device produces high quality output vector beams, however, the latter are limited to the two SOPs mentioned above. Another device can be built to produce higher order vector beams by changing the rubbing direction of the two plates.

Another technique relies on the principle of optical spin-to-orbital angular momentum conversion of a light beam [71]. Using specially patterned LC plates, called q-plates, with birefringence retardation δ and topological charge q, one can modify the orbital angular momentum of an optical field [72]. The q-plate is said to be tuned when δ is set to π. This tuning is wavelength dependent but can be controlled electrically or thermally [73, 74]. For instance, a tuned plated with a topological charge of $q = 1/2$ allows for the creation of AP and RP beams from a horizontally and vertically LP beam input, respectively [64, 75].

Another method relies on nanogratings generated by ultrashort pulses within a slab of glass [63, 76], so-called s-waveplates. Due to the spatially varying birefrigence of the optical element created, it allows for conversion of circularly polarized light into cylindrical vector beams. The handedness of the input beam dictates whether the output beam is RP or AP. It also shows a high damage threshold compared to previously mentioned LC devices. However, each s-waveplate must be fabricated for a specific wavelength, which limits its versatility. Such plates are now also commercially available.

A more versatile method used to generate vector beams relies on SLMs. By combining two SLMs and a quarter-wave plate, one can in principle generate any arbitrary vector beam [77–79]. The first SLM applies a desired phase pattern, while the quarter-wave plate and second SLM act as a local polarization rotator. In principle, the polarization orientation of an input beam can be controlled pixel-by-pixel. More details about SLM technology will be discussed later. Other less common methods have been suggested to generate cylindrical vector beams and are well-reviewed by Zhan [12]. More recently, studies have suggested the use of designed metasurfaces composed of individual subwavelength nanostructures for highly efficient and versatile generation of vector beams [80].

Cylindrical vector beams have found applications in various fields of optics ranging from optical manipulation [81, 82] to laser cutting [83]. Optical telecommunication could also benefit from cylindrical and more complex vector beams to increase the

possible bandwidth of data transmission [84]. However, linear [24–26] and nonlinear imaging [31] have benefited the most from such vector beams due to their interesting focusing properties that will be described later in this Thesis.

2.3.2 Vector Bessel beams

Bessel beams are diffraction-free solutions of the Helmholtz equation presented in Eq.(2.24) with theoretical properties first described by Colin Sheppard [85] and later by Jim Durnin [86]. In principle, such beams show an infinite depth of field, that is to say, the energy is confined close to the optical axis over an infinite distance. They also show what is called a self-healing property, which represents their capabilities to regenerate after meeting an obstacle. However, due to optical sources having finite energy and optical components having limited apertures, one can synthesize only approximate Bessel beams in the laboratory, so-called quasi-Bessel beams or BG beams, with formulation presented earlier in Eq.(2.24). For the sake of simplicity, the possible use of the term Bessel beam in experimental conditions will always refer to a quasi-Bessel beam, or BG beam. Even though the generated beams are approximations of the perfect cases, they already show the interesting properties of Bessel beams. Such beams with homogeneous polarizations are usually created using passive elements.

First, using a circular, also called annular, aperture in front of a Gaussian beam and then focusing the ring formed allows for the generation a Bessel beam [85, 87]. To create an ideal Bessel beam, this ring should in principle be infinitely thin and contain an infinite amount of energy and therefore only approximations of such beams are generated. The quality of the Bessel beam generated is also dependent on the quality of the annular aperture used and such amplitude filtering is not efficient.

The most common method relies on axicons [88–90]. Due to their focusing geometry, they allow for the conversion of a Gaussian beam into a Bessel beam. Even though such method is efficient, axicons are expensive and imperfections in their fabrication can quickly distort the quality of the Bessel beam [91].

Finally, SLMs offer more versatility for generating Bessel beams from a Gaussian beam [92, 93] and has become a valuable alternative to other optical components. The phase displayed is an axicon phase wrapped between 0 and 2π. Even though a SLM is more expensive, it offers the possibility to simulate axicons with various

apex angles. SLMs are, however, less efficient. Generally speaking, it is important to note that the parameters of the generated Bessel beam, especially the extent of the depth of field, depends on the parameters of the optical component used [94, 95]. In **Paper III**, we used a SLM to generate a LPBG beam. This choice can be justified for two main reasons: first, the LP of the beam made the use of the SLM rather straightforward. Then, the software of the SLM (Holoeye) gave us the possibility to quickly generate axicon phases with tunable parameters. We could then easily tune, for instance, the size of the ring to be focused by the microscope objective.

On the other hand, vector Bessel beams represent the non-diffractive solutions to the full vectorial Helmholtz wave equation [96, 97]. They constitute the extension of Bessel beams with homogeneous SOPs, obtained through the scalar wave equation, to optical beams with inhomogeneous SOPs. In principle, vector Bessel beams, similarly to Bessel beams, show an infinite depth of field and a self-healing property. However, their best physical approximations are vector BG beams, with formulation presented earlier in Eq.(2.27) and Eq.(2.28). Similarly, the use of the term vector Bessel beams in experimental conditions will refer to vector BG beams. Several methods exist to generate vector Bessel beams that involve the original techniques used to create Bessel beams. These include using SLMs [98–100] and axicons [101, 102]. In **Paper IV**, we switched from using a SLM to using an axicon. This choice can be explained by the limitation of the SLM to LP and by low conversion efficiency we would have encountered by using both a radial converter and a SLM to generate the APBG or RPBG beam. Combining such devices is, however, an option to create an APBG or RPBG beam [100].

Bessel beams have found extensive uses in various fields like micromanipulation [103], micromachining [104], and even telecommunications [105]. The characteristic properties of Bessel beams have also been used in volumetric imaging of 3D samples in the context of linear [106, 107] and nonlinear optics [108–110]. The extended depth of field of such beams indeed allows for fast imaging of thick samples without having to perform sequential axial scans using a beam with short depth of field.

3. TIGHT FOCUSING OF VECTOR BEAMS

After having described and presented the different modes of optical beams and their respective SOPs, it is now important to introduce the tools used for beam propagation and tight focusing. From this description will arise the importance of polarization before focusing and the origin of longitudinal electric fields at focus. In this Section, we will mostly use the formalism introduced by Richards and Wolf [9] and summarized by Novotny and Hecht [111].

3.1 Angular spectrum representation

The **angular spectrum representation** (ASR) is a powerful tool for precisely modeling the propagation and tight focusing of laser beams. The idea of this method is to decompose a light beam into a series of plane waves and evanescent waves propagating in different directions and with different amplitudes. Following this and considering the electric field of light at a fixed plane orthogonal to the direction z, we can express the two-dimensional **Fourier transform** of the electric field $\boldsymbol{E}$ in this fixed plane as:

$$\hat{\boldsymbol{E}}(k_x, k_y; z) = \frac{1}{4\pi^2} \iint_{-\infty}^{+\infty} \boldsymbol{E}(x, y, z) e^{-i(k_x x + k_y y)} \, dx \, dy \tag{3.1}$$

with $\hat{\cdot}$ being the symbol of the Fourier transform and $\boldsymbol{E} = (E_x, E_y, E_z)$ and $\hat{\boldsymbol{E}} = (\hat{E}_x, \hat{E}_y, \hat{E}_z)$ being vectors. For completeness, we can also define the inverse Fourier transform of Eq.(3.1):

$$\boldsymbol{E}(x, y, z) = \iint_{-\infty}^{+\infty} \hat{\boldsymbol{E}}(k_x, k_y; z) e^{i(k_x x + k_y y)} \, dk_x \, dk_y \tag{3.2}$$

Now, if we consider free-space propagation of a light beam, its electric field obeys the vector Helmholtz equation presented before in this work in Eq.(2.25). From there, and by defining $k_z \equiv \sqrt{(k^2 - k_x^2 - k_y^2)}$, we find that the Fourier spectrum evolves in propagation as follows:

$$\hat{\boldsymbol{E}}(k_x, k_y; z) = \hat{\boldsymbol{E}}(k_x, k_y; 0) e^{\pm i k_z z} \tag{3.3}$$

This equation means that the Fourier transform of the electric field at any given plane z can be simply obtained by knowing the Fourier transform at the plane $z = 0$ and by multiplying the latter by the **propagator** $e^{\pm i k_z z}$. The electric field in the image plane can then be obtained by taking the inverse Fourier transform of Eq.(3.3):

$$\boldsymbol{E}(x, y, z) = \iint_{-\infty}^{+\infty} \hat{\boldsymbol{E}}(k_x, k_y; 0) e^{i(k_x x + k_y y \pm k_z z)} \, dk_x \, dk_y \tag{3.4}$$

This equation embodies the ASR. In many practical cases, light diverges only slowly from the direction of propagation. This is typically the case for laser beam propagation. On the basis of this, an assumption can be made that simplifies greatly the analytical treatment of Eq.(3.4) and is known as the **paraxial approximation**. It suggests that the contribution of transverse wavevectors (k_x, k_y) is negligible compared to k, which allows for Taylor expansion of k_z in the exponential :

$$k_z = k\sqrt{1 - (k_x^2 + k_y^2)/k^2} \approx k - \frac{(k_x^2 + k_y^2)}{2k} \tag{3.5}$$

This approximation can be used, for example, in the treatment of weakly focused laser beams with homogeneous or inhomogeneous polarizations. However, this assumption does not apply anymore in the case of tight focusing, where light rays emerge or converge with large angles with respect to the overall direction of propagation. In this Thesis, and depending on the input polarization, significant longitudinal electric fields might arise by tightly focusing the laser beam through a high NA microscope objective. Therefore, the full ASR shall be considered in the following chapters of this work.

3.2 Tight focusing and longitudinal fields

ASR is an appropriate tool for showing that tight focusing of an optical beam through a high NA microscope objective allows for the generation of strong longitu-

dinal fields within the focal volume depending on the input polarization. For this, we consider a far-field entering the microscope objective and want to know the full electric field distribution within the focal volume. The far-field is evaluated at a point situated at infinite distance from the object plane. In order to use the ASR method, the far-field distribution of the optical field needs to be expressed in terms of its Fourier spectrum. It can be shown that they are linked through the following equation:

$$\hat{\boldsymbol{E}}(k_x, k_y; 0) = \frac{ire^{-ikr}}{2\pi k_z} \boldsymbol{E}_\infty(k_x, k_y) \tag{3.6}$$

which can be plugged back into Eq.(3.4) of the ASR:

$$\boldsymbol{E}(x, y, z) = \frac{ire^{-ikr}}{2\pi} \iint\limits_{(k_x^2+k_y^2)\leq k^2} \boldsymbol{E}_\infty(k_x, k_y) e^{i(k_x x + k_y y \pm k_z z)} \frac{1}{k_z}\, dk_x\, dk_y \tag{3.7}$$

The integration is limited to $(k_x^2 + k_y^2) \leq k^2$ because exponentially decaying evanescent fields do not contribute to the far-field. It is also interesting to see that if we take $k_z \approx k$, Eq.(3.7) becomes a perfect Fourier transform which therefore shows the limits of *Fourier optics*.

We can now describe the tight focusing of a paraxial optical field by an aplanatic lens of focal length f, that is to say a lens free from spherical aberration and coma. The following formalism was established by Richards and Wolf [9] and we will follow the notation presented by Novotny and Hecht [111]. Fig. 3.1 helps visualize the optical system composed of an aplanatic lens, which models the high NA microscope objective used in our experiments. In principle, a microscope objective is composed of several optical elements. However, the theoretical derivation of focal fields and the simulations of focal fields presented later are based on the focusing of the input field by the aplanatic lens, which gives a good approximation of the focusing of light by a more complex microscope objective. The dotted red line represents the optical axis, that is to say, the line passing through the center of the microscope objective and parallel to the main direction of propagation of the beam. We set that $(x_\infty, y_\infty, z_\infty)$ represent the coordinates of a point on a reference sphere, centered on the focal point of the aplanatic lens and of radius f, and (x, y, z) represents the coordinates of a point near the focus. In the spherical coordinate system, they take the form (f, θ, ϕ) and (r, ν, φ), respectively. It is also relevant to introduce a series of unit vectors to describe the refraction at the reference sphere: the couple $(\boldsymbol{n}_\rho, \boldsymbol{n}_\phi)$ represents the unit vectors of a cylindrical coordinate system whereas the couple

$(\boldsymbol{n}_\theta, \boldsymbol{n}_\phi)$ represents the unit vectors of a spherical coordinate system.

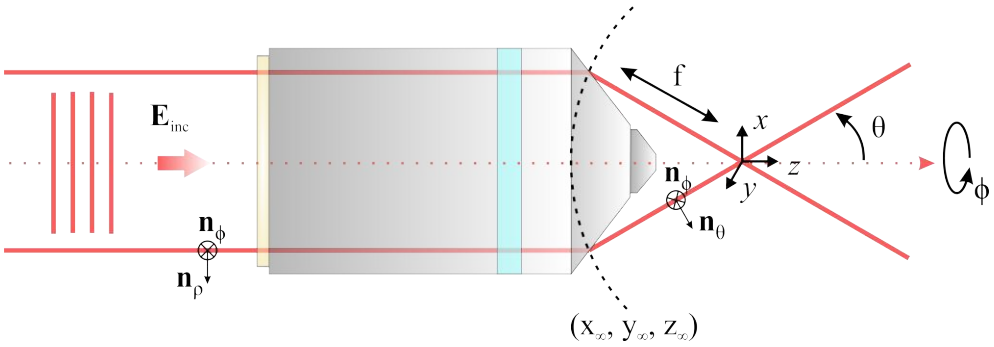

Figure 3.1 *Representation of a microscope objective modeled by an aplanatic lens system and its coordinates for tight focusing.*

An optical electric field $\boldsymbol{E}_{inc}$ incident on the aplanatic lens can then be described by its (s) and (p) polarization, the components perpendicular and parallel to the plane of incidence, respectively. Such components can be expressed as follows:

$$\boldsymbol{E}_{inc}^{(s)} = [\boldsymbol{E}_{inc} \cdot \boldsymbol{n}_\phi]\, \boldsymbol{n}_\phi \tag{3.8}$$

$$\boldsymbol{E}_{inc}^{(p)} = [\boldsymbol{E}_{inc} \cdot \boldsymbol{n}_\rho]\, \boldsymbol{n}_\rho \tag{3.9}$$

Due to refraction, the unit vectors mentioned above experience geometrical transformations: the azimuthal unit vector n_ϕ remains the same but the radial component n_ρ is transformed into n_θ. The total refracted field $\boldsymbol{E}_\infty$ can then be expressed by:

$$\boldsymbol{E}_\infty = [t^s\, [\boldsymbol{E}_{inc} \cdot \boldsymbol{n}_\phi]\, \boldsymbol{n}_\phi + t^p\, [\boldsymbol{E}_{inc} \cdot \boldsymbol{n}_\rho]\, \boldsymbol{n}_\theta] \sqrt{\frac{n_1}{n_2}} (cos\theta)^{1/2} \tag{3.10}$$

with n_1 and n_2 being the refractive index of the medium before and after the aplanatic lens respectively, and $t^{(s,p)}$ representing the Fresnel transmission coefficients. The term $\sqrt{\frac{n_1}{n_2}}(\cos\theta)^{1/2}$ appears as an energy conservation factor.

In order to later obtain the 3D components of the focal fields, it is important to express the unit vectors previously mentioned in terms of Cartesian coordinates:

$$\begin{aligned} \boldsymbol{n}_\rho &= \cos\phi \boldsymbol{n}_x + \sin\phi \boldsymbol{n}_y \\ \boldsymbol{n}_\phi &= -\sin\phi \boldsymbol{n}_x + \cos\phi \boldsymbol{n}_y \\ \boldsymbol{n}_\theta &= \cos\theta\cos\phi \boldsymbol{n}_x + \cos\theta\sin\phi \boldsymbol{n}_y - \sin\theta \boldsymbol{n}_z \end{aligned} \tag{3.11}$$

Let us now insert these vectors into Eq.(3.10) to get the Cartesian components of the field $\boldsymbol{E}_\infty$ just at the right of the aplanatic lens, but evaluated far away from the

focus $(x, y, z) = (0, 0, 0)$:

$$\begin{aligned}\boldsymbol{E}_\infty(\theta,\phi) =& t^s(\theta)\left[\boldsymbol{E}_{inc}(\theta,\phi)\cdot\begin{pmatrix}-\sin\phi\\ \cos\phi\\ 0\end{pmatrix}\right]\begin{pmatrix}-\sin\phi\\ \cos\phi\\ 0\end{pmatrix}\sqrt{\frac{n_1}{n_2}}(cos\theta)^{1/2}\\ &+ t^p(\theta)\left[\boldsymbol{E}_{inc}(\theta,\phi)\cdot\begin{pmatrix}\cos\phi\\ \sin\phi\\ 0\end{pmatrix}\right]\begin{pmatrix}\cos\phi\cos\theta\\ \sin\phi\cos\theta\\ -\sin\theta\end{pmatrix}\sqrt{\frac{n_1}{n_2}}(cos\theta)^{1/2}\end{aligned} \tag{3.12}$$

In order to use the ASR, we need to express $\boldsymbol{E}_\infty$ in terms of its spatial frequencies knowing that:

$$\begin{aligned}k_x &= k\sin\theta\cos\phi\\ k_y &= k\sin\theta\sin\phi\\ k_z &= k\cos\theta\end{aligned} \tag{3.13}$$

Due to the symmetry of the problem, it is more convenient to express the ASR in terms of θ and ϕ. By using the relations 3.13 and performing a change of variables for a double integral, we get that:

$$\frac{1}{k_z}dk_x dk_y = k\sin\theta d\theta d\phi \tag{3.14}$$

If we now consider the transformation of the Cartesian coordinates $x = \rho\cos\varphi$ and $y = \rho\sin\varphi$, the ASR of the focal field can be expressed as follows:

$$\boldsymbol{E}(\rho,\varphi,z) = \frac{ikfe^{-ikf}}{2\pi}\int_0^{\theta_{max}}\int_0^{2\pi}\boldsymbol{E}_\infty(\theta,\phi)e^{ikz\cos\theta}e^{ik\rho\sin\theta\cos(\phi-\varphi)}\sin\theta\, d\theta\, d\phi \tag{3.15}$$

The limits of the double integral come from the finite dimensions of the physical system. We can link θ_{max} to the NA of the lens, or microscope objective, with the relation $NA = n\sin\theta_{max}$, with $n = n_2$ the refractive index after the lens. We also decided to restrict our study to a field propagating in the forward direction, therefore retaining only the + sign in Eq.(3.7).

It is important to see that Eq.(3.15) directly links the 3D spatial distribution of the optical field at focus to its far-field spatial distribution right after the lens. Therefore, we can now study the tight focusing of several laser modes mentioned in Section 2.2. By doing so, we shall see that the distribution and strength of longitudinal fields at

focus are highly dependent on the input state of polarization of $\boldsymbol{E}_{inc}$.

We will focus here on the tight focusing by a high NA microscope objective of LP modes like HG_{00}, HG_{10}, HG_{10}, and later emphasize their combinations to form RP and AP beams. Let us start with an optical field polarized along the horizontal direction:

$$\boldsymbol{E}_{inc} = E_{inc}\boldsymbol{n}_x \tag{3.16}$$

For simplicity, we assume that the objective is highly transmissive at the wavelength considered, hence $t^s(\theta) = t^p(\theta) = 1$. By plugging this back into Eq.(3.12), we get:

$$\begin{aligned}\boldsymbol{E}_\infty(\theta,\phi) &= E_{inc}(\theta,\phi)[\cos\phi\boldsymbol{n}_\theta - \sin\phi\boldsymbol{n}_\phi]\sqrt{\frac{n_1}{n_2}}(cos\theta)^{1/2} \\ &= \frac{E_{inc}(\theta,\phi)}{2}\begin{pmatrix}(1+\cos\theta)-(1-\cos\theta)\cos 2\phi \\ -(1-\cos\theta)\sin 2\phi \\ -2\cos\phi\sin\theta\end{pmatrix}\sqrt{\frac{n_1}{n_2}}(cos\theta)^{1/2}\end{aligned} \tag{3.17}$$

It is now time to define the amplitude distribution of the input beam defined by E_{inc}. For the first three lowest order HG modes, their amplitude profiles can be expressed in Cartesian and spherical coordinates as:

$$E_{inc}(HG_{00}) = A_0 e^{-(x_\infty^2+y_\infty^2)/w_0^2} = A_0 e^{-f^2\sin^2\theta/w_0^2} \tag{3.18}$$

$$E_{inc}(HG_{10}) = \frac{2A_0 x_\infty}{w_0} e^{-(x_\infty^2+y_\infty^2)/w_0^2} = \frac{2A_0 f}{w_0}\sin\theta\cos\phi e^{-f^2\sin^2\theta/w_0^2} \tag{3.19}$$

$$E_{inc}(HG_{01}) = \frac{2A_0 y_\infty}{w_0} e^{-(x_\infty^2+y_\infty^2)/w_0^2} = \frac{2A_0 f}{w_0}\sin\theta\sin\phi e^{-f^2\sin^2\theta/w_0^2} \tag{3.20}$$

with w_0 representing the waist of the mode before focusing. The **apodization function** $f_w(\theta) = e^{-\frac{1}{f_0^2}\frac{\sin^2\theta}{\sin^2\theta_{max}}}$, similar to a pupil filter, shall be used in the next steps, where θ_{max} represents the maximum focusing angle, and $f_0 = \frac{w_0}{f\sin\theta_{max}}$ being the filling factor. The integration over ϕ can be performed analytically using the following relations:

$$\int_0^{2\pi}\cos n\phi e^{ix\cos(\phi-\varphi)}\,d\phi = 2\pi(i^n)J_n(x)\cos n\varphi \tag{3.21}$$

$$\int_0^{2\pi}\sin n\phi e^{ix\cos(\phi-\varphi)}\,d\phi = 2\pi(i^n)J_n(x)\sin n\varphi \tag{3.22}$$

with, as seen previously in Section 2.2, $J_n(x)$ being the nth-order Bessel function. For the sake of being concise, we also define the following integrals appearing along the calculation:

$$I_{00} = \int_0^{\theta_{max}} f_w(\theta)(\cos\theta)^{1/2}\sin\theta(1+\cos\theta)J_0(k\rho\sin\theta)e^{ikz\cos\theta}\,d\theta \tag{3.23}$$

$$I_{01} = \int_0^{\theta_{max}} f_w(\theta)(\cos\theta)^{1/2}\sin^2\theta J_1(k\rho\sin\theta)e^{ikz\cos\theta}\,d\theta \tag{3.24}$$

$$I_{02} = \int_0^{\theta_{max}} f_w(\theta)(\cos\theta)^{1/2}\sin\theta(1-\cos\theta)J_2(k\rho\sin\theta)e^{ikz\cos\theta}\,d\theta \tag{3.25}$$

$$I_{10} = \int_0^{\theta_{max}} f_w(\theta)(\cos\theta)^{1/2}\sin^3\theta J_0(k\rho\sin\theta)e^{ikz\cos\theta}\,d\theta \tag{3.26}$$

$$I_{11} = \int_0^{\theta_{max}} f_w(\theta)(\cos\theta)^{1/2}\sin^2\theta(1+3\cos\theta)J_1(k\rho\sin\theta)e^{ikz\cos\theta}\,d\theta \tag{3.27}$$

$$I_{12} = \int_0^{\theta_{max}} f_w(\theta)(\cos\theta)^{1/2}\sin^2\theta(1-\cos\theta)J_1(k\rho\sin\theta)e^{ikz\cos\theta}\,d\theta \tag{3.28}$$

$$I_{13} = \int_0^{\theta_{max}} f_w(\theta)(\cos\theta)^{1/2}\sin^3\theta J_2(k\rho\sin\theta)e^{ikz\cos\theta}\,d\theta \tag{3.29}$$

$$I_{14} = \int_0^{\theta_{max}} f_w(\theta)(\cos\theta)^{1/2}\sin^2\theta(1-\cos\theta)J_3(k\rho\sin\theta)e^{ikz\cos\theta}\,d\theta \tag{3.30}$$

This set of abbreviations allows us to finally give a compact form of the focal electric fields for each mode considered and for each of their Cartesian components (x, y, z):

$\boldsymbol{HG}_{00}$:

$$\boldsymbol{E}(\rho,\varphi,z) = \frac{ikf}{2}\sqrt{\frac{n_1}{n_2}}A_0 e^{-ikf}\begin{pmatrix} I_{00}+I_{02}\cos 2\varphi \\ I_{02}\sin 2\varphi \\ -2iI_{01}\cos\varphi \end{pmatrix} \tag{3.31}$$

$\boldsymbol{HG}_{10}$:

$$\boldsymbol{E}(\rho,\varphi,z) = \frac{ikf^2}{2w_0}\sqrt{\frac{n_1}{n_2}}A_0 e^{-ikf}\begin{pmatrix} iI_{11}\cos\varphi + iI_{14}\cos 3\varphi \\ -iI_{12}\sin\varphi + iI_{14}\sin 3\varphi \\ -2I_{10} + 2I_{13}\cos 2\varphi \end{pmatrix} \tag{3.32}$$

$\boldsymbol{HG}_{01}$:

$$\boldsymbol{E}(\rho,\varphi,z) = \frac{ikf^2}{2w_0}\sqrt{\frac{n_1}{n_2}}A_0 e^{-ikf}\begin{pmatrix} i(I_{11}+2I_{12})\sin\varphi + iI_{14}\sin 3\varphi \\ -iI_{12}\cos\varphi - iI_{14}\cos 3\varphi \\ 2I_{13}\sin 2\varphi \end{pmatrix} \tag{3.33}$$

It is interesting to note that the presence or absence of longitudinal electric field on the optical axis can be quickly deducted from the form of the integrals defined in Eqs. 3.23 to 3.30 that contain Bessel functions of different orders. Only the zeroth-order Bessel function has a non-zero value at its origin. Therefore, so far, only the HG_{10} mode shows a longitudinal field (E_z) component on the optical axis, whereas the two others have off-axis E_z fields. For instance, Fig. 3.2 shows the calculated spatial distribution of the electric focal fields for each Cartesian component of the focused HG_{00} and HG_{10} modes, important in this Thesis.

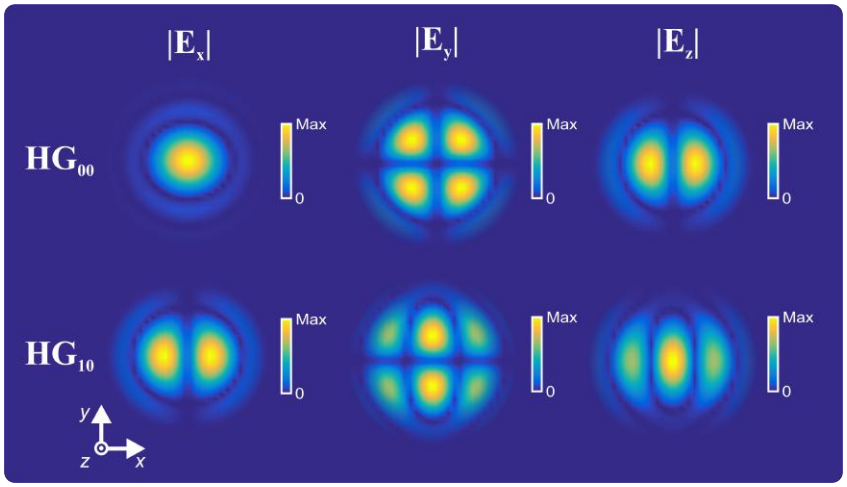

Figure 3.2 *Transverse spatial distribution of focal electric field components of tightly focused x-polarized HG_{00} and HG_{10} modes.*

We can now have a look at the 3D focal field components of RP and AP beams and see the important implications that such inhomogeneous SOPs bring in terms of longitudinal fields. As described in Eqs. 2.29 and 2.30, the RP and AP modes can be generated by superposition of HG_{10} and HG_{01} modes. Their Cartesian focal field components can then be expressed as follows:

RP mode:

$$\boldsymbol{E}(\rho,\varphi,z) = \frac{ikf^2}{2w_0}\sqrt{\frac{n_1}{n_2}}A_0 e^{-ikf}\begin{pmatrix} i(I_{11}-I_{12})\cos\varphi \\ i(I_{11}-I_{12})\sin\varphi \\ -4I_{10}\end{pmatrix} \tag{3.34}$$

AP mode:

$$\boldsymbol{E}(\rho,\varphi,z) = \frac{ikf^2}{2w_0}\sqrt{\frac{n_1}{n_2}}A_0 e^{-ikf}\begin{pmatrix} i(I_{11}+3I_{12})\sin\varphi \\ -i(I_{11}+3I_{12})\cos\varphi \\ 0\end{pmatrix} \tag{3.35}$$

Due to the polarization distribution of an RP beam, its tight focusing generates a strong on-axis longitudinal electric field. On the other hand, an AP beam does not possess any longitudinal electric field at focus. However, the latter actually shows a strong on-axis magnetic field, due to the orthogonal orientation of the electric field in the far-field compared to a radial beam. Fig. 3.3 shows the calculated norm of the electric focal fields for each Cartesian component for RP and AP beams.

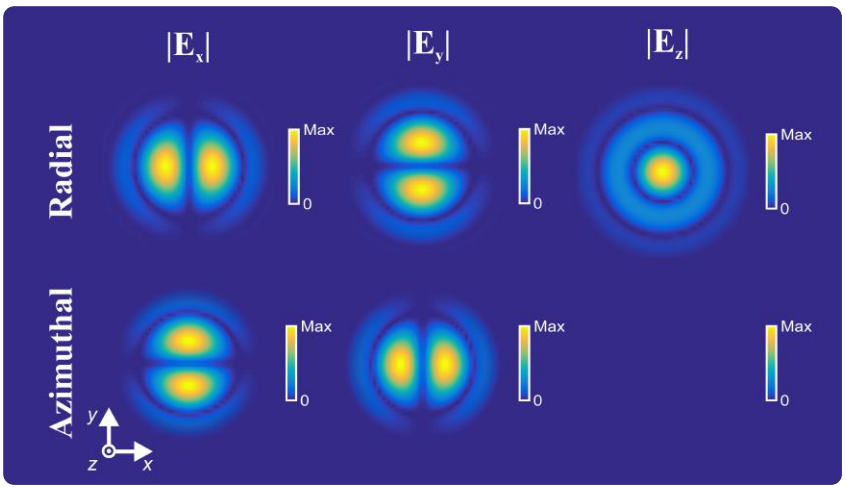

Figure 3.3 *Transverse spatial distribution of focal electric field components of tightly focused RP and AP modes.*

We did not provided representations of the norm of the total electric field at focus because the form of the total electric field depends on the strength of each Cartesian component of the electric field at focus, which depends on the focusing angle [10, 111].

3.3 Tailoring and verification of electric field components at focus

Due to the major implications of laser modes and polarization for various areas of optics, progress has recently been made towards better spatial control of polarization over the beam cross section. Such techniques are often based on the manipulation of laser modes with inhomogeneous polarization to achieve polarization control at focus. We shall focus here on techniques which have for goal to tailor the polarization landscape at focus or focal electric field components. Other techniques that do not consider polarization will not be treated here. In order to experimentally demonstrate such 3D polarization control capabilities, methods to probe the focal fields components or polarization at focus have also been developed and will be discussed in this Section.

3.3.1 Tailored polarization at focus using vector beams

Vector beams form the basis for the 3D control of polarization at focus. In order to have control on the state of polarization at focus, one needs to tailor the input light beam before focusing as the 3D components at focus are linked to the input beam amplitude, phase, and polarization, as already shown in Section 3.2. Various works have suggested methods for achieving full 3D control of polarization at focus [38–40, 42, 112] or for creating complex polarization architecture [41].

The first method directly makes use of AP and RP beams [39]. By superimposing these two beams and by controlling the apodization function at the back aperture of a microscope objective, one can in principle produce arbitrary 3D polarization orientations. Several polarization orientation at focus were demonstrated using polarization-sensitive melting of gold nanorods and their subsequent two-photon fluorescence. This method, however, requires the generation of two separate vector beams that have to be combined later.

A more versatile and programmable design relies on the use of SLMs [42, 113]. The aim, similar to the previous method, is to control the orientation of the polarization at focus at any transverse plane. In order to generate a focused beam with arbitrary homogeneous polarization at focus, this technique provides the required amplitude and polarization properties of the input field at the pupil plane of a high NA objective

lens by solving an inverse problem with the set of equations described in Section 3.2. A major drawback of this method is its rather low-efficiency due to the multiple use of SLMs, but it is highly programmable and re-configurable.

Interestingly, because closely related to the phase-shaping principles used in this Thesis, spatial phase-shaping of various SOPs has been theoretically implemented to tailor the transverse and longitudinal spatial distribution of focal field components at focus, using designed binary phase elements before focusing or more complex SLM phase masks [37, 114].

Among the techniques mentioned above, some have seen their capabilities hindered by the difficulty to characterize the electric field components at focus. The most relevant techniques are thus described in the next Section.

3.3.2 Measurements of optical field components at focus

A major part of controlling 3D polarization at focus involves capabilities to verify and experimentally probe such focal field components. These techniques allow for more or less direct reconstruction of electric field components within the focal volume.

A rather new reconstruction method is based on nanointerferometry [47]. The beam whose focal fields are to be determined is focused onto a spherical gold nanoparticles. The total transmitted scattered signal at the back focal plane of the collecting objective is imaged by a pixelated camera, and this for each position of the particle across the focused beam. By applying a specific reconstruction algorithm, one can then retrieve the amplitude and the phase of each Cartesian component of the focal fields. Several factors limit, however, the applicability of this technique. Among these, the nanoparticle chosen needs to have appropriate dimensions that have to be determined precisely beforehand, as such dimensions will be directly used in the reconstruction algorithm.

Near-field methods can also be used to map focal fields. Near-field scanning optical microscopy (NSOM) is, for instance, a method capable of characterizing focal fields [44]. However, the collected signals from most probes often represents a mixture of information from different field components, and the fields detected depend on the material as well as geometry of the probe. Modified schemes of NSOM have, however,

shown to be able to unambiguously map focal fields in 3D [44, 115]. Another near-field method is based on the collection of scattered fields from a nano-tip that is scanned across the focused beam [43]. It was shown to be a reliable technique to unambiguously probe longitudinal electric fields.

Single molecules with fixed dipole orientation also allow for focal field mapping [23]. By recording a raster scan image of the fluorescence rate from single molecules with a determined orientation, one can determine the Cartesian components of the electric field of a focused beam. For instance, molecules lying in the transverse plane map the transverse electric field components at focus, whereas molecules oriented orthogonal to the transverse plane map the longitudinal electric field components at focus. On the other hand, if one knows the electric field distribution at focus, one can determine the orientation of single molecules.

The work presented in this Thesis includes an alternative method, based on SHG of vertically aligned GaAs nanowires, which offers a direct method for mapping longitudinal electric fields within the focal volume. It is based on the preference of such nanowires for longitudinal electric field in SHG. More details about the technique appear in Section 5.3.

4. ROLE OF LONGITUDINAL FIELDS IN NONLINEAR OPTICAL MICROSCOPY

Tight focusing often occurs in optical microscopy due to the use of high NA objectives. It is then essential to consider the properties of optical fields within the focal volume, especially in nonlinear microscopy due to the tensorial character of the nonlinear response of materials. In this Chapter, we introduce the nonlinear wave equation and focus on SHG. We also detail the impact of 3D focal fields in the context of SHG microscopy and provide an overview for other nonlinear microscopy techniques. It is important to note that the term microscopy might be strictly used when it implies the formation of a magnified image of a microscopic sample. Here, we will use the term microscopy in a broader sense, including the detection of signals from nano-objects using light focused by a microscope objective. The image formed by raster-scanning may then not be a magnified image of the nano-object itself, but contains other useful information.

4.1 Nonlinear wave equation

We are now interested in the light-matter interaction between a focused laser beam and a nonlinear material. Therefore, the free space wave equation described in Eq.(2.12) needs to be adjusted and more parameters need to be taken into account. When the electric field is strong enough, the induced polarization does not depend anymore linearly on the input electric field. The induced polarization is crucial in a nonlinear material and therefore cannot be taken as zero to describe the propagation of an optical wave. Therefore, we need to take into account that $\tilde{\boldsymbol{D}} = \epsilon_0 \tilde{\boldsymbol{E}} + \tilde{\boldsymbol{P}}$ with $\tilde{\boldsymbol{P}} \neq 0$. According to the notation used in Boyd's book [7], the wave equation transforms then to:

$$\nabla^2 \tilde{\boldsymbol{E}} - \frac{1}{c^2} \frac{\partial^2 \tilde{\boldsymbol{E}}}{\partial t^2} = \frac{1}{\epsilon_0 c^2} \frac{\partial^2 \tilde{\boldsymbol{P}}}{\partial t^2} \tag{4.1}$$

or, by using Eq.(2.5):

$$\nabla^2 \tilde{\boldsymbol{E}} - \frac{1}{\epsilon_0 c^2} \frac{\partial^2 \tilde{\boldsymbol{D}}}{\partial t^2} = 0 \tag{4.2}$$

It is relevant to separate the linear and nonlinear contributions to the polarization $\tilde{\boldsymbol{P}}$ and electric displacement field $\tilde{\boldsymbol{D}}$ using the following relations:

$$\tilde{\boldsymbol{P}} = \tilde{\boldsymbol{P}}^{(1)} + \tilde{\boldsymbol{P}}^{NL} \tag{4.3}$$

$$\tilde{\boldsymbol{D}} = \tilde{\boldsymbol{D}}^{(1)} + \tilde{\boldsymbol{P}}^{NL} \tag{4.4}$$

$$\tilde{\boldsymbol{D}}^{(1)} = \epsilon_0 \tilde{\boldsymbol{E}} + \tilde{\boldsymbol{P}}^{(1)} \tag{4.5}$$

where $\tilde{\boldsymbol{P}}^{(1)}$ and $\tilde{\boldsymbol{D}}^{(1)}$ represent the linear polarization and linear electric field displacement, respectively, and $\tilde{\boldsymbol{P}}^{NL}$ represents the nonlinear polarization. Using the above mentioned relations, Eq.(4.1) becomes:

$$\nabla^2 \tilde{\boldsymbol{E}} - \frac{1}{\epsilon_0 c^2} \frac{\partial^2 \tilde{\boldsymbol{D}}^{(1)}}{\partial t^2} = \frac{1}{\epsilon_0 c^2} \frac{\partial^2 \tilde{\boldsymbol{P}}^{NL}}{\partial t^2} \tag{4.6}$$

This equation forms a wave equation where the nonlinear response of the medium acts as a source for the electric field generated. This equation can be used further to describe specific nonlinear optical effects in various materials.

4.2 Second-harmonic generation

As mentioned before, when the strong electric field of an input beam interacts with matter, the induced polarization does not respond linearly anymore with respect to the input electric field. If this electric field is sufficiently strong, the polarization of the medium can be described using a power series:

$$\tilde{P}(t) = \epsilon_0 [\chi^{(1)} \tilde{E}(t) + \chi^{(2)} \tilde{E}^2(t) + \chi^{(3)} \tilde{E}^3(t) + ...] \tag{4.7}$$

where $\chi^{(i)}$ represents the ith-order susceptibility, characterizing the optical properties of a specific medium. Due to the form of the electric field and from 4.7 and 4.6, we see that such polarization response leads to the generation of electric fields at new optical frequencies. In this Section, we shall focus on second-order nonlinear effects, like SHG, most relevant considering the work in this Thesis. This process, represented in Fig. 4.1 is known to be parametric, that is to say, the energy is conserved and therefore no energy from the input photons is deposited into the ma-

terial. Hence, nondestructive and label-free imaging can be performed using SHG [4, 116].

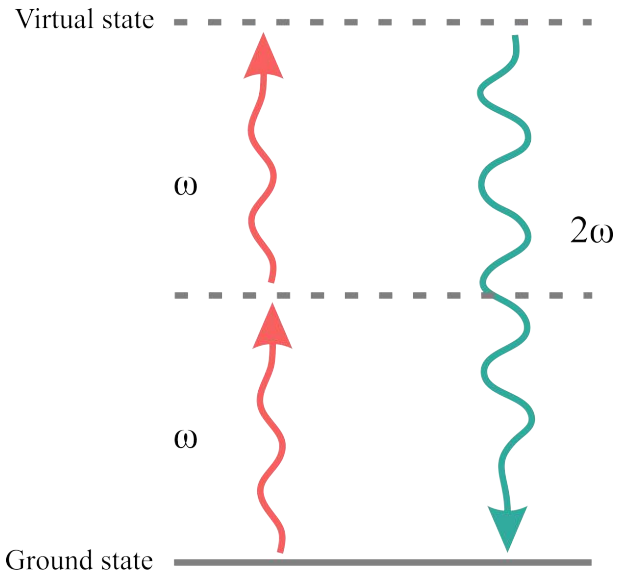

Figure 4.1 *Photon diagram of SHG process. Two photons at frequency ω are annihilated and one photon at 2ω is generated.*

In the most general case, the amplitude of the second-order nonlinear polarization is linked to the product of field amplitudes through the tensor $\chi^{(2)}_{ijk}(\omega_n + \omega_m, \omega_n, \omega_m)$, known as the second-order nonlinear optical susceptibility, as follows:

$$P_i(\omega_n + \omega_m) = \epsilon_0 \sum_{jk} \sum_{(nm)} \chi^{(2)}_{ijk}(\omega_n + \omega_m, \omega_n, \omega_m) E_j(\omega_n) E_k(\omega_m) \tag{4.8}$$

where ijk represent the Cartesian coordinates and the (nm) notation states that the summation over n and m allows for ω_n and ω_m to vary as long as $\omega_n + \omega_m$ is held constant. It is therefore crucial to know the components of the tensor $\chi^{(2)}_{ijk}(\omega_n + \omega_m, \omega_n, \omega_m)$.

In principle, many values need to be determined. Luckily, several restrictions on the second-order susceptibility allow us to reduce the amount of components required to describe the nonlinear polarization. First, the *reality of the fields* implies that:

$$\chi^{(2)}_{ijk}(-\omega_n - \omega_m, -\omega_n, -\omega_m) = \chi^{(2)}_{ijk}(\omega_n + \omega_m, \omega_n, \omega_m)^* \tag{4.9}$$

Then, the *intrinsic permutation symmetry*, physically meaning that the order of the product $E_j(\omega_n)E_k(\omega_m)$ does not affect the physical outcome of the process, allows

us to write that:

$$\chi^{(2)}_{ijk}(\omega_n + \omega_m, \omega_n, \omega_m) = \chi^{(2)}_{ikj}(\omega_n + \omega_m, \omega_m, \omega_n) \tag{4.10}$$

A new tensor containing the components of the second-order susceptibility is often used. It is defined as follows:

$$d_{ijk} = \frac{1}{2}\chi^{(2)}_{ijk} \tag{4.11}$$

and contains in principle 27 independent components according to the assumptions detailed before. If we now consider the case of SHG, we see that $\omega_n = \omega_m = \omega$, which allows us to introduce new indices il in place of ijk with the following index correspondence:

$$\begin{array}{cccccccc} jk: & 11 & 22 & 33 & 23,32 & 31,13 & 12,21 \\ l: & 1 & 2 & 3 & 4 & 5 & 6 \end{array} \tag{4.12}$$

We see that for SHG, the number of independent components to be determined is further reduced to 18. All in all, and by using Eq.(4.8), the Cartesian components of the nonlinear polarization for SHG can be summarized as follows:

$$\begin{pmatrix} P_x(2\omega) \\ P_y(2\omega) \\ P_z(2\omega) \end{pmatrix} = 2\epsilon_0 \begin{pmatrix} d_{11} & d_{12} & d_{13} & d_{14} & d_{15} & d_{16} \\ d_{21} & d_{22} & d_{23} & d_{24} & d_{25} & d_{26} \\ d_{31} & d_{32} & d_{33} & d_{34} & d_{35} & d_{36} \end{pmatrix} \begin{pmatrix} E_x^2(\omega) \\ E_y^2(\omega) \\ E_z^2(\omega) \\ 2E_y(\omega)E_z(\omega) \\ 2E_x(\omega)E_z(\omega) \\ 2E_x(\omega)E_y(\omega) \end{pmatrix} \tag{4.13}$$

So far, we have considered only physical properties of the SHG process itself to limit the number of tensor components needed. However, symmetry properties of the optical medium can reduce even further the number of independent susceptibility components. This can be understood by the fact that some materials show after spatial transformation similar properties before and after this transformation.

A particular type of symmetry reduces the number of materials eligible for second-

order processes, hence SHG. It is known as inversion symmetry or *centrosymmety*. If a material possesses an inversion center, the second-order susceptibility must vanish identically. One can easily show this property for SHG if we assume an instantaneous response of the nonlinear medium to the electric field:

$$\tilde{P}(t) = \epsilon_0 \chi^{(2)} \tilde{E}^2(t) \tag{4.14}$$

For a centrosymmetric material, a change in the sign of the electric field implies a change in the sign of the induced polarization:

$$-\tilde{P}(t) = \epsilon_0 \chi^{(2)} [-\tilde{E}]^2(t) = \epsilon_0 \chi^{(2)} \tilde{E}^2(t) \tag{4.15}$$

The latter equation is valid, only if:

$$\chi^{(2)} = 0 \tag{4.16}$$

This selectivity makes SHG a powerful nonlinear optical process. In addition, it is important to note that whenever the centrosymmetry is broken, for instance at the surface or interface, second-order effects are possible [117].

It is important also to note that other spatial symmetry properties of the material considered can help to identify the allowed form of the susceptibility tensor. For instance, let us consider the case of GaAs, important for the work in this Thesis. The common lattice structure of GaAs is cubic. However, in its zinc-blende form, GaAs belongs to the $\bar{4}3m$ crystal point group and therefore shows noncentrosymmetry due to the relative position of the Ga and As atoms in the lattice. In the end, the second-order susceptibility tensor of GaAs possesses only three components, which happen to be equal: $d_{36} = d_{25} = d_{14}$. The zinc-blende structure and the second-order nonlinear tensor of GaAs are described in Fig. 4.2.

It is important to note that GaAs can also grow in a hexagonal structure. This form is known as *wurzite* and also shows a second-order nonlinear response [118, 119]. However, this crystal configuration belongs to the $6mm$ crystal point group and therefore the components of the second-order nonlinear tensor are different compared to the zinc-blende form [7] (p. 49).

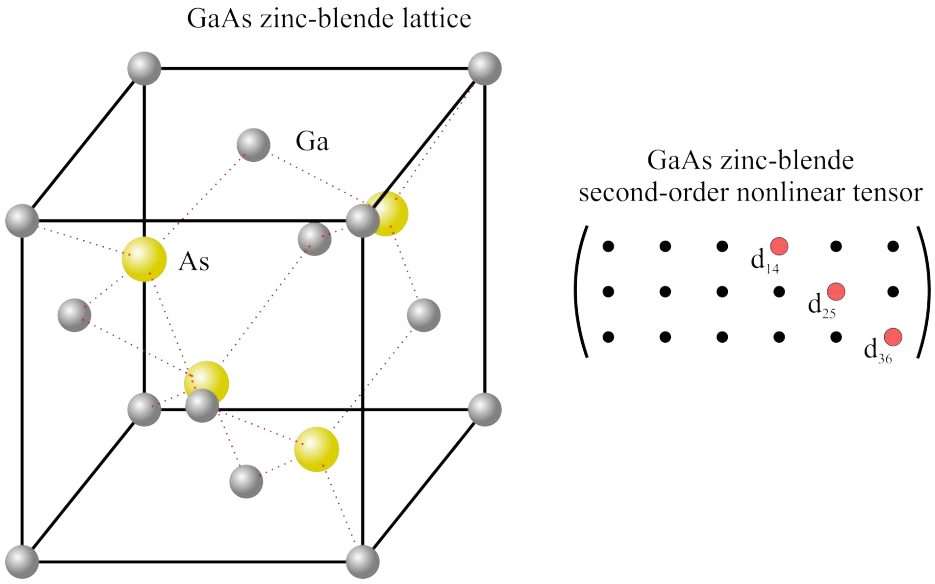

Figure 4.2 *Crystal lattice of GaAs in its zinc-blende form and its associated second-order nonlinear tensor.*

4.3 Vector beams in nonlinear microscopy

In this Section, we justify the importance of developing methods to control the longitudinal field component at focus by presenting the benefits of such fields in the context of SHG microscopy. We also provide a short overview of recent demonstrations of the importance of 3D SOPs in the context of other nonlinear microscopy techniques.

4.3.1 Longitudinal electric fields in SHG microscopy

The particular polarization properties of vector beams and the selection rules of the SHG process makes the combination of the two a great tool for microscopy. Above all, the 3D SOP of light at focus and especially the longitudinal fields have tremendous effects on the SHG from nano-objects. The importance of longitudinal electric fields at focus was already pointed out for SHG in bulk crystals even under weak focusing using LP light [120]. These results showed that the longitudinal electric field component of the input field has consequences on the SHG response of a nonlinear crystal, even when such fields are often neglected due to weak focusing conditions. The longitudinal electric fields also play a rather important role in SHG from thin films. Since the latter exhibit a strong out-of-plane SHG response,

longitudinal electric field components are then highly desirable. An RP beam can be used to induce a confined and strong longitudinal field component at focus to drive SHG [121]. Finally, and more related to this Thesis, longitudinal electric fields have shown to have significant consequences for SHG microscopy of single and tailored nanostructures.

Coupling vector beams that provide such 3D SOPs at focus to the selectivity offered by the second-order nonlinear tensor of materials is a formidable tool for imaging and characterizing nano-objects. Depending on their shape, orientation, and symmetry, such nano-objects will respond differently to the 3D behavior of the electric field within the focal volume, where both transverse and longitudinal field components play a role. For instance, longitudinal fields are important for enhanced SHG from metal nanocones supporting plasmonic oscillations along the cone axis [30, 32, 34]. The response is therefore highly dependent on the respective strength of transverse and longitudinal fields at focus, and this in turn directly linked to the input state of polarization [32, 33]. Biological imaging can also depend on 3D optical fields. It was shown numerically and experimentally that the longitudinal field component of an RP beam improves SHG signals from collagen fibers [27, 28, 35, 122]. SHG imaging using AP and RP beams also helps to determine molecular orientations in such fibers [123]. It is important to note here that the improvement in SHG signals observed using RP beam is highly dependent on the 3D fiber orientation. Thus, fibers aligned along the longitudinal field created by the RP beam showed higher SHG signals, but one would expect that fibers aligned perpendicular to the longitudinal direction would be more sensitive to the transverse fields of an AP beam.

Another very interesting aspect of the combination vector beams and SHG forms the basic principle on which the work presented in Thesis relies. It has been pointed out that studying SHG of designed nanostructures allows for the spatial mapping of longitudinal electric fields [34, 36]. This feature highlights two important points: first, it confirms the importance of longitudinal electric fields for exciting efficiently certain types of nano-objects, and secondly, it provides a technique for direct imaging of the spatial distribution of the longitudinal field component of an input beam at focus. This last point is crucial considering that there are very few methods available to determine the longitudinal field distribution at focus.

4.3.2 Focused vector beams in other nonlinear microscopy techniques

We detailed the influence and benefits of the 3D SOPs within the focal volume, highlighting the importance of longitudinal electric fields, in the context of SHG considering the work performed in this Thesis. However, other nonlinear microscopy techniques can also benefit from vectorial fields at focus and should be mentioned here. This overview provides insights on other nonlinear microscopy techniques but is not exhaustive. Thorough and well-constructed reviews are found elsewhere [5, 31].

Third-harmonic generation (THG) microscopy uses THG as the main source of contrast, where three photons at frequency ω generate a photon at frequency 3ω. Such process is really sensitive to material inhomogeneities. This technique has been used for material characterization [2, 15, 124, 125] but also for nanostructures [126]. Regarding the benefits of vectorial focal fields, they remain limited compared to SHG. However, some works have suggested to use vector beams to increase the transverse resolution of THG microscopy [127, 128] or to even use THG to characterize the spatially varying polarization state distribution at focus [129]. Interestingly, similarly to SHG microscopy, THG microscopy is sensitive to the 3D structure of the sample imaged and controlling 3D focal fields could bring more opportunities in this context [30, 130].

Coherent-Anti-Stokes Raman scattering (CARS) microscopy also benefits from 3D focal fields. In CARS, a four-wave mixing process, two laser beams at frequency ω_1 and $\omega_2 < \omega_1$ interact in a medium. From this interaction, a new frequency at $2\omega_1 - \omega_2$ is generated. If the difference $\omega_1 - \omega_2$ corresponds to the vibrational frequency ω_v of the material, the nonlinear response exhibits a resonance. Due to this, CARS is often used for probing molecular structures [14, 131–133]. Even though CARS microscopy is more challenging in its implementation than SHG or THG due to the precise tuning of two input beams, the use of vector beams has been spreading quite much in CARS microscopy. The main reason for this is that CARS microscopy suffers from a nonresonant background signal that limits the contrast achievable. It appears that engineering the 3D SOP at focus can improve this contrast [134–136]. This enhanced contrast is in most cases a direct consequence of the pronounced longitudinal electric field at focus [29, 136].

Finally, *two-photon excited fluorescence and luminescence* (TPF, TPL) constitute a non-negligible part of nonlinear optical microscopy. Contrast here is achieved through the absorption of two photons by labels or dyes and their relaxation with emission of a photon through fluorescence. TPF and TPL are, however, incoherent processes. In this context, resolution has been increased by using vector beams [137–139]. Similarly to SHG, TPF can be also used for orientation imaging [39, 140, 141].

In this Thesis, we aim to provide tools for further development of controllable longitudinal electric field components but also 3D SOPs within the focal volume in general. A direct demonstration of such tailored focal fields is shown using SHG, but previous paragraphs show that our technique can find further applications in other nonlinear microscopy fields.

5. MANIPULATION AND VERIFICATION OF LONGITUDINAL ELECTRIC FIELDS

In the present and following chapters, we shall present the experimental details composing the techniques used for controlling the 3D parameters of longitudinal electric fields through phase-shaping and the method used for verifying such longitudinal field at focus. The experimental details of the phase-shaping techniques will be presented in Section 5.2. Section 5.3, on the other hand, will provide details about the sample used to probe and verify the longitudinal electric field component at focus.

5.1 General setup

In all the publications included in this Thesis, the same basic optical setup was used and only a few components were different between experiments. This setup is described in Fig. 5.1 and includes two main parts. The first part contains the filtering and phase-shaping components used to control longitudinal electric fields. The second part is about detecting such longitudinal electric fields. This part remained unchanged, whereas the phase-shaping part, where the excitation beam was prepared, was varied.

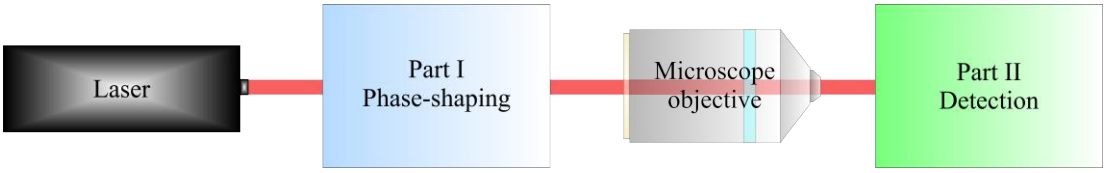

Figure 5.1 *General optical setup used in the experiments.*

A mode-locked femtosecond laser at the wavelength of 1060 nm with a 140 fs pulse length and a 80 MHz repetition rate was used as the excitation source. The laser beam, after filtering and shaping described in Section 5.2, was directed to an infinity-corrected microscope objective with NA of 0.8. This objective was used to tightly

focus the excitation beam in order to allow for the possible generation of significant longitudinal electric field components, the latter highly dependent on the input beam SOP. Such fields were probed in the detection part described in Section 5.3.

5.2 Phase-shaping techniques

This Section describes the various phase-shaping techniques used to achieve longitudinal field control at focus. The first part is dedicated to the spatial phase-shaping of an HG_{10} mode and the second part presents the methods used to generated vector Bessel beams.

5.2.1 Phase-shaping using HG_{10} modes

As mentioned in previous chapters, an important parameter that affects the electric field distribution at focus is the polarization distribution across the input beam before focusing. The relationship between each local SOP across the beam can be controlled by adding a spatially designed phase across part of the input beam. In order to do this, we looked for the most versatile and programmable technique to apply precise phase delays over a determined area of the input beam.

SLMs appeared to be the best option for us. They are nowadays widely used and have become an essential component for optical manipulation [142–144], beam shaping [77, 93, 113, 145, 146], microfabrication [147–149], microscopy [150, 151], and nonlinear optics [152, 153]. SLMs come in different types, but we shall focus on the one used in our experiments. Phase-reflective SLMs are devices composed of a liquid-crystal display (LCD), where each pixel can be controlled independently. Due to the birefringence of LC and their arrangement, one can apply an additional phase delay pixel-by-pixel to a horizontally polarized beam reflecting from the display. Usually, the SLM is used as a second display monitor plugged to a computer. The phase control is achieved by displaying a gray level map with values between 0 and 255 on the computer screen. Those values are then converted into voltage via a graphic card to tilt the LC composing the LCD. Depending on the voltage, directly linked to the gray value of the pixel, one can apply delays from 0 to over 2π depending on the input wavelength. Even though SLMs offer flexibility in terms of programmability, they might also show some disadvantages like low efficiency, or nonlinearities of the phase response. Another undesirable feature comes from

the space between the pixels, characteristic of a non-perfect fill factor, leading to the generation of an undiffracted component. In **Paper I** and **Paper II**, an 8-bit Hamamatsu SLM with a pixel resolution of 792 × 600 and a fill factor of 98% was used, dramatically limiting the amount of undesirable undiffracted component.

Both our SLMs experienced a nonlinear phase response with respect to the gray levels applied. Such artifact gave us the opportunity to design and develop a homemade calibration technique. This technique is based on the study of focal field intensity variations of a LP Gaussian beam observed when applying increasing phase delays on one half of the SLM. By correlation of numerical and experimental data, we were able to retrieve the nonlinear phase curve and apply a compensated gray level function on our SLM phase masks to linearize the phase variations for gray levels ranging between 0 and 255. The result of our phase calibration method is summarized in Fig. 5.2, and compared with the traditional interferometric method used for SLM phase calibration.

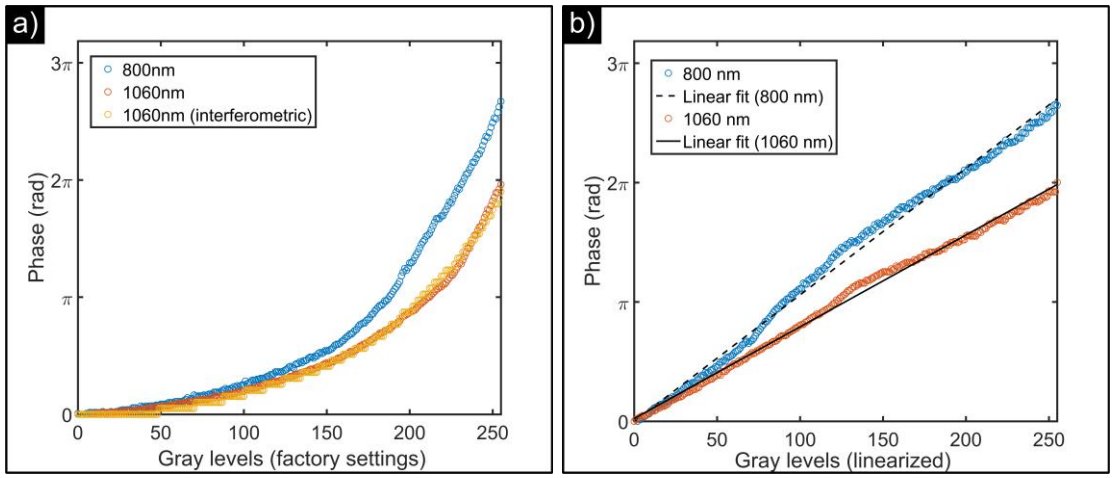

Figure 5.2 *Phase response curve of our Hamamatsu SLM a) before and b) after phase linearization for two different input wavelengths using our own phase calibration method.*

We chose to use an HG_{10} mode as an input beam for several reasons. First, it shows a strong longitudinal field on axis at focus [34]. Hence, signals from each individual nanowire excited with the HG_{10} mode would then constitute a reference before applying our phase-shaping scheme and help us locate each nanowire. Then, remembering that the SLM accepts only horizontally polarized light as input, a horizontally polarized HG_{10} mode was suitable for this configuration. Finally, its two-lobe spatial distribution was interesting because the window of the SLM could then be electronically separated into two sub-windows dedicated to each lobe, with

the phase discontinuity situated between the two lobes of the mode. Then, two different phase delays could be applied on each lobe of the HG_{10} mode. In **Paper I**, the HG_{10} mode was generated by discriminating the horizontally polarized part of an RP beam using a linear polarizer. The RP beam was generated using a radial converter which transforms a LP input beam into an RP or AP beam, as described in Section 2.3.1. In **Paper II**, the HG_{10} mode was generated using a π-phase plate, fabricated by collaborators at TUT, converting a HG_{00} into HG_{10} [154]. It might be relevant to note that the HG_{10} could have been generated using the SLM itself [67], but the availability of the radial converter or π-phase plate made it straightforward to generate the HG_{10} mode.

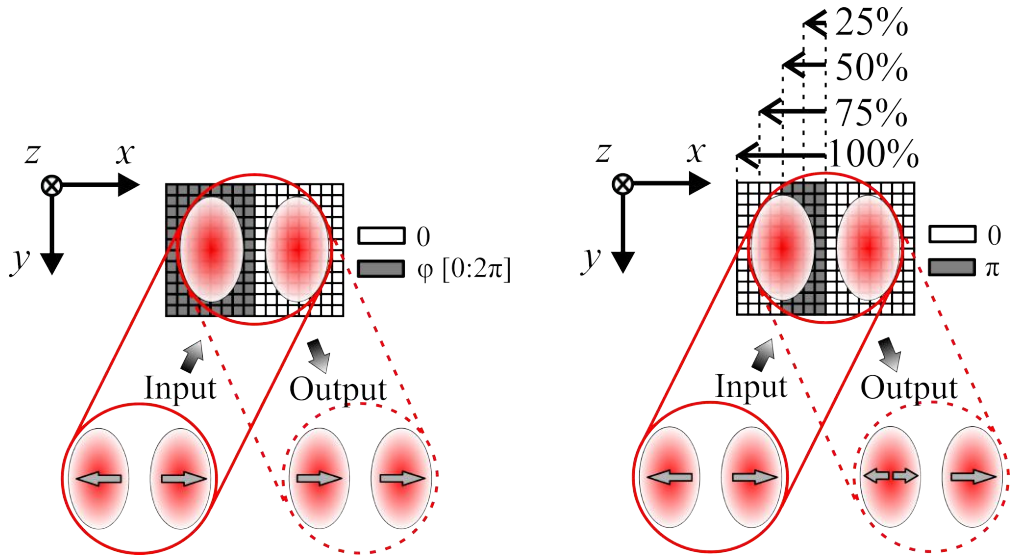

Figure 5.3 *Schematic diagram of spatial phase-shaping of an HG_{10} mode with the SLM using the two different techniques described in* ***Paper I*** *and* ***Paper II****. φ represents a varying phase delay applied on the SLM. Figures adapted, with permission, from* ***Paper I*** *and* ***Paper II****.*

Two phase-shaping designs were considered to control the longitudinal electric field distribution at focus. In **Paper I**, we gradually applied phase delays from 0 to 2π on a full lobe of the HG_{10} mode and collected SHG from GaAs nanowires for each phase value chosen. In this context, the electric field of each lobe of the HG_{10} mode would oscillate in opposite phase for no additional phase and in phase for π additional phase delay applied on one of the lobe, and finally back to opposite phase for 2π. This phase-shaping scheme is described in Fig. 5.3, left side. In **Paper II**, the principle is fundamentally different because we chose to apply only an additional π phase delay but this time over a varying area of one lobe of the HG_{10} mode. Only

0 and π phases were involved and therefore such technique is often referred as binary phase-shaping [37]. In our experiment, π phase delays were applied over quarters of this lobe (0%, 25%, 50%, 75%, 100%), as described on the right side of Fig. 5.3, whereas the other lobe remained unaltered. The cases where the coverage is 0% and 100% correspond to settings similar to the ones presented in **Paper I**.

5.2.2 Bessel beam generation

To gain further control over the longitudinal extent of the longitudinal electric field at focus, we focused our interest on Bessel beams. As a proof of principle, we decided to generate first a LPBG beam. For this, we used a LP HG_{00} beam as input on the SLM. We displayed an axicon phase wrapped between 0 and 2π on the SLM and is described in Fig. 5.4. In this case, we used a SLM from Holoeye with high pixel resolution but with a smaller fill factor (93%).

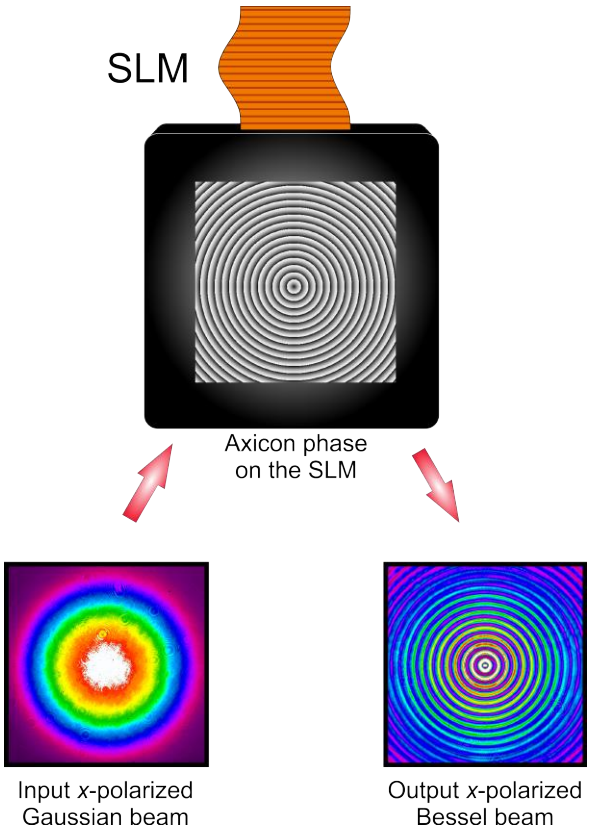

Figure 5.4 *Experimental input LP Gaussian beam and LPBG beam, captured with a beam profiling camera, generated using an axicon phase displayed on the SLM. Figure adapted, with permission, from* ***Paper III****.*

The choice of the SLM for generating the LPBG beam was justified in Section 2.3.2, among which polarization of the input beam and programmability of the SLM used made us lean towards such arrangement. As mentioned before, a Bessel beam forms a really thin ring at the focus of a lens which facilitated the filtering of the on-axis undiffracted component due to the imperfect fill factor of the SLM using a physical block at the focus. After collimation, we placed another lens before the microscope objective in order to create a ring at the back focal plane of the microscope objective. This led to the formation of a Bessel beam at focus.

For the generation of an RPBG or APBG beam, the optical setup was a bit modified, due to fundamental limitations, and is described in Fig. 5.5. To achieve pure phase-shaping, the SLM indeed requires horizontally polarized light as input. Therefore, using an RP beam as input on the SLM would have not led to an RPBG beam. We had to switch method and opted for an axicon. We mentioned in Section 2.3.2 the reasons for this choice, mostly related to efficiency and to the aim to attain. The collimated RP beam entered the axicon to form an RPBG beam. Similarly to a LPBG beam, a set of lenses was then used to create an RP ring at the back focal plane of the microscope objective to recover the RPBG beam at focus. After the axicon, or at the focal plane of the microscope objective, it is interesting to note that the intensity distribution of an RPBG beam shows a doughnut shape with many rings around it, whereas the recorded intensity distribution of a LPBG beam shows a spot on-axis with many rings around it [100]. This observation confirms the mathematical description of BG and vector BG beams provided earlier in this Thesis.

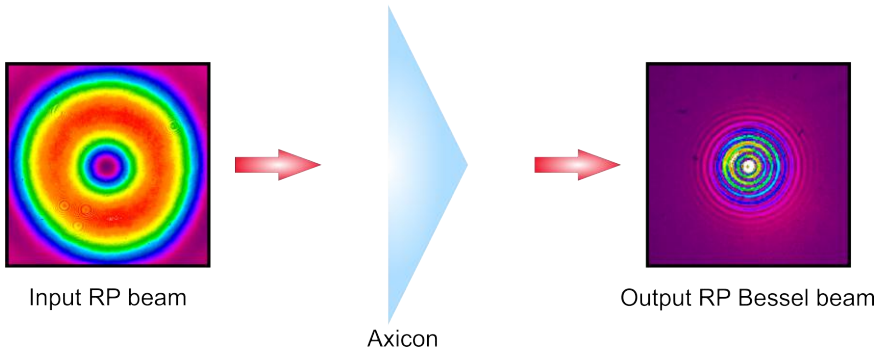

Figure 5.5 *Experimental input RP beam and output RPBG beam, captured with a beam profiling camera, generated using an axicon.*

5.3 Verification of longitudinal electric fields

In this Section, we describe the method used to probe the spatial distribution of longitudinal electric fields at focus. It is based on SHG collected from vertically aligned GaAs nanowires. Such nano-objects have been shown to be sensitive to only longitudinal electric field excitation. We first present the sample and then described the methods used to collect SHG signals and map the longitudinal electric fields.

5.3.1 GaAs nanowires

All the experiments performed in the laboratory and described in this Thesis are based on SHG imaging of vertically standing semiconductor nanowires. They were fabricated and characterized by collaborators at Aalto University. Such nanowires are composed of a semiconductor material which here is GaAs. The nanowires were grown on a GaAs substrate. In a nutshell, the fabrication consisted of forming a mask with periodic holes through which GaAs could only grow vertically. Such a process is known as selective-area metallo-organic vapour-phase epitaxy (SA-MOVPE). First, a GaAs substrate of growth orientation [111]B, according to Miller's indices [155](p. 8), was covered by an amorphous silicon oxide layer of 40 nm thickness using plasma-enhanced chemical vapour deposition. This layer was then patterned with holes in a periodic triangular lattice. The pitch of the lattice used in our experiments is between 2.4 and 2.5 μm, but can be smaller if required. These holes were made using electron-beam lithography and reactive ion etching, forming holes of about 55 nm diameter. From this point, the growth of the nanowires can start. Two phases, the solid substrate and the vapor precursors carrying Ga and As atoms, react together. The temperature, kept below the melting point of the substrate, allows the gaseous precursors to attach to the substrate and therefore Ga and As atoms will take their respective positions in the crystal lattice. This process is copied to subsequent layers and epitaxial growth occurs. The nanowires formed have an average length of 2 to 2.5 μm and an average diameter of 55 nm. This diameter can be slightly larger than the diameter of the holes due to possible, but limited, radial growth.

After the nanowires were grown, their exact dimensions were determined using scanning and transmission electron microscopy (SEM, TEM) and crystallinity using electron diffraction (ED). These experiments were performed also by collaborators at

Aalto University. According to Fig. 5.6, the nanowires show an exceptional structural quality. They are well separated and well standing on the substrate. Even though the crystallinity is not perfect, showing several stacking faults, it shows a predominant zinc-blende structure.

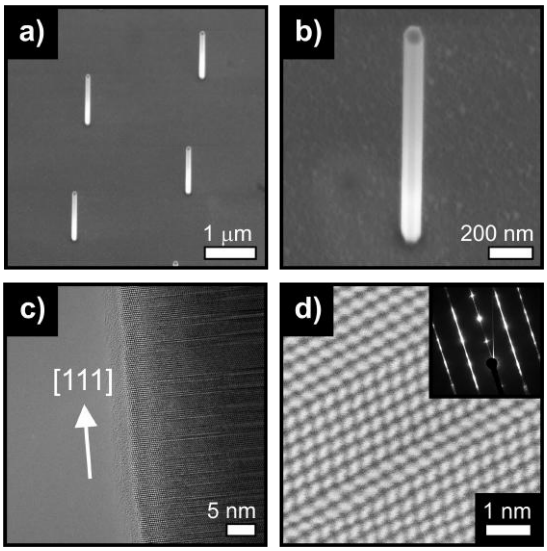

Figure 5.6 *SEM (a,b), TEM (c,d), and ED (inset) images of the vertically aligned GaAs nanowires used in our experiments. Figure adapted, with permission, from* ***Paper I****.*

5.3.2 Detection of SHG signals

As discussed in Section 4.2, GaAs possesses a second-order bulk response when in its common zinc-blende form. For the nanowires grown along the [111] crystal direction, the second-order susceptibility has only three equal non-vanishing tensor components $\chi^{(2)}_{xyz}$, $\chi^{(2)}_{yxz}$, and $\chi^{(2)}_{zxy}$, with x, y, and z referring to the coordinate system of the crystal. In this case, it has been shown that electric field components parallel to the growth axis of the nanowires primarily drive SHG in GaAs nanowires [36], which can also be monitored in 3D [156]. Therefore, generating longitudinal electric fields at focus is highly desirable for efficient SHG and enhanced contrast, but most of all, such nano-objects allow us to probe the longitudinal electric field of a focused beam at focus.

The sample containing the GaAs nanowires was placed on a three-axis piezo-scanning stage, controlled via a computer. SHG signals from nanowires were collected in epi-detection through the same microscope objective and measured using a photomultiplier tube sensitive to the SHG wavelength of 530 nm. The final SHG images

were formed by raster scanning, i.e., by recording the total intensity pixel-by-pixel. This technique therefore allows mapping of the longitudinal electric field at focus considering that each single nanowire acts as a probe. The separation between fundamental and frequency doubled signals was performed using appropriate dichroic and band pass filters. In all experiments, input power levels between 1 and 2 mW were used, enough to get a high contrast in terms of signals from the nanowires, but low enough to avoid destruction of the nanowires.

6. TRANSVERSE DISTRIBUTION CONTROL OF LONGITUDINAL ELECTRIC FIELDS

This Chapter presents and discusses the results obtained in **Paper I** and **Paper II** using the phase-shaping schemes mentioned above. Here, we shall have a look at the SHG raster scan images collected for various input beam polarizations and phase-shaping parameters.

6.1 Experimental results

First, and as presented in **Paper I**, we imaged the GaAs nanowires using reference beams such as a horizontally polarized HG_{00} mode, an RP and AP beam, and a HG_{10} mode without additional phase delay (unshaped beam). The results are in Fig. 6.1. As expected, SHG from GaAs nanowires is strong only when the input polarization shows non-vanishing longitudinal electric field components at focus. For instance, using an RP beam at the input gives rise to the strongest SHG signal, and this due to the significant longitudinal electric field component at focus for this beam. On the other hand, using an AP beam with the same input power does not lead to SHG from these nanowires. The reason for this is that a tightly focused AP does not generate longitudinal electric field components at focus and the local SOP remains transverse even at focus. Then, using an HG_{00} and HG_{10} mode as input, the SHG image of a single nanowire, respectively, exhibits a two-lobed and three-lobed intensity pattern, resembling the longitudinal field of the respective focal fields, as seen in Fig. 3.2. The spot-like distribution of the longitudinal electric field of an RP beam predicted in Fig. 3.3 is also confirmed here. The results obtained here for using an HG_{00}, an AP, and an RP mode strengthen the data presented in Ref. [36] and the data obtained using an HG_{10} mode is reminiscent of the results presented in Ref. [34]. This set of data confirms the role of GaAs nanowires for probing the spatial distribution of longitudinal electric field at focus using point-scanning SHG microscopy.

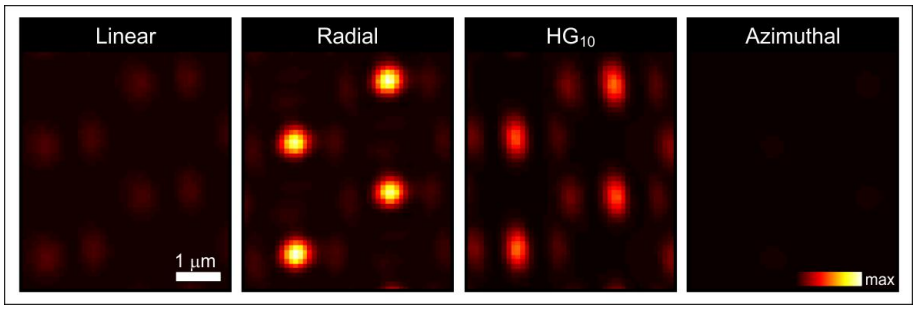

Figure 6.1 *Transverse SHG intensity maps from GaAs nanowires using reference vector beams. Figure adapted, with permission, from* ***Paper I****.*

We applied our phase-shaping scheme on the HG_{10} mode. As mentioned previously, even though an RP beam gives rise to maximum longitudinal electric fields at focus and therefore maximum SHG in our case, the polarization restriction of the SLM directed our choice towards the HG_{10} mode, which shows already a significant longitudinal electric field component at focus. In **Paper I**, we performed a set of SHG scans for different additional phase delays applied on one lobe of the HG_{10}. By doing this, the electric field of each lobe oscillates with a different relative phase depending on the additional phase applied on the lobe. The results are summarized in Fig. 6.2. Without phase delay, the beam is unshaped and the SHG from a single nanowire shows the three-lobed distribution observed already in Fig. 6.1. For a 2π delay, we also recover the same SHG distribution and this is as expected considering that the input beam shows two lobes oscillating in opposite phase, just like the unshaped HG_{10} mode. For delays increasing from 0 to π, the three-lobed distribution slowly switches to two off-axis lobes with lower intensities. This can be understood due to the two lobes of the HG_{10} beam oscillating in phase before focusing for a π delay. For this setting, the phase shaped HG_{10} mode now resembles a LP beam [157, 158], however retaining its two-lobed spatial distribution before focusing. For this reason, a π phase shaped HG_{10} and a LP HG_{00} show similar longitudinal field distributions at focus, confirmed by SHG signals but also simulations, available in the supplementary material of **Paper I**. This observation is especially interesting because it shows that one can modify the longitudinal electric field distribution at focus by simple phase-shaping without switching the input beam mode using more cumbersome methods. We then applied additional phase delays between π and 2π and observed symmetric SHG variations compared to the 0 and π range. In addition to these experiments, we verified that applying the same phase delay on both lobes preserved the three-lobed distribution of the SHG signal, thus the longitudinal electric field distribution of the unshaped HG_{10} at focus. This is expected because

the important parameter is the relative phase delay between the two lobes of the input beam, and not the absolute phase.

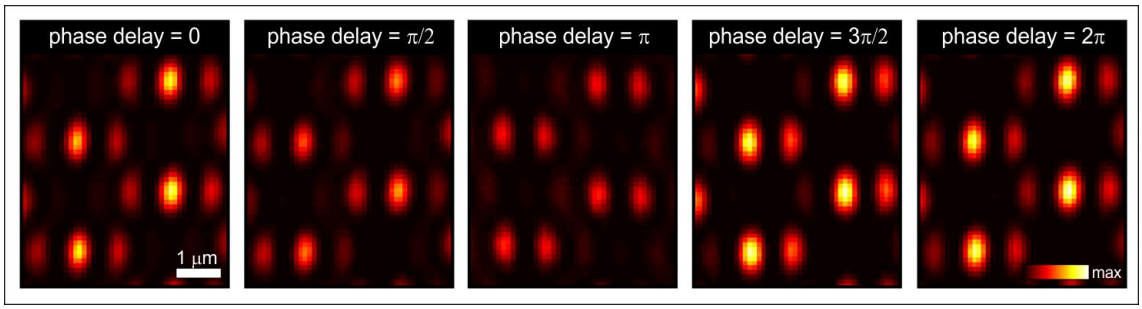

Figure 6.2 *Transverse SHG intensity maps from GaAs nanowires after applying additional phase delays on one lobe of the HG_{10} mode. Figure adapted, with permission, from* ***Paper I****.*

In **Paper II**, we performed similar experiments but this time by applying the phase-shaping scheme described on the right side of Fig. 5.3. We used only a π additional phase delay on part of one lobe of the HG_{10} mode and collected SHG for different spatial coverages (0%, 25%, 50%, 75%, 100%) of the delay. The results are summarized in Fig. 6.3 where a line cut across the SHG distribution of a single nanowire is plotted for each coverage. As expected, 0% and 100% π phase-shaping in **Paper II** match similar settings and SHG results of **Paper I** for 0 and π phase delays. The idea behind this binary phase-shaping, involving only a π addtional phase delay, was to gradually increase the strength of the electric field of one lobe of the HG_{10} to oscillate in phase with the other lobe and approach the polarization distribution of a LP HG_{00} mode, therefore switching from a three-lobed to a two-lobed longitudinal field distribution at focus. To ensure that variations in SHG at focus emerged from pure phase-shaping of the input beam, we applied a 2π delay for an arbitrary coverage value, 50% in our case, on one lobe and observed no changes in the SHG distribution from a single nanowire compared to SHG signals using an unshaped HG_{10}. For intermediate coverages (25%, 50%, and 75%), we notice a gradual shift of the center peak of the SHG distribution to the right to finally form the two-lobed distribution characteristic to the longitudinal field distribution of a tightly focused LP beam. Therefore, by increasing the amount of the lobe that is π phase delayed, we switch from a strong to a really weak longitudinal field component on the optical axis.

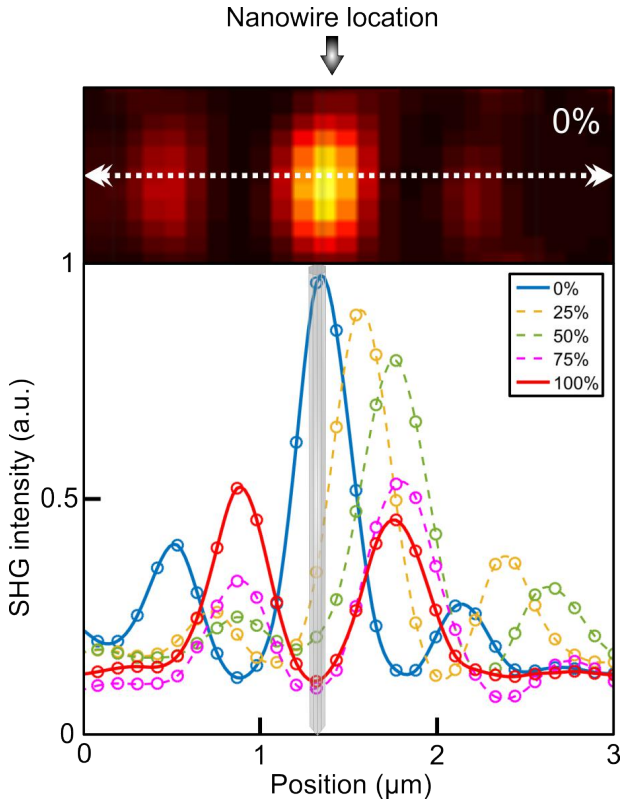

Figure 6.3 *Transverse SHG intensity map from a single GaAs nanowire by applying additional π phase delays on one lobe of the HG_{10} mode with varying coverage. Figure adapted, with permission, from* ***Paper II****.*

6.2 Discussion

The two techniques presented above both show that one can achieve precise control over the spatial distribution and strength of longitudinal electric fields at focus by simply phase-shaping the input beam. This is interesting because the laser alignment is in no way altered and no optical component is moved or added into the optical setup in order to modify the longitudinal electric field distribution at focus. The only parameter tuned is the phase map or level displayed on the SLM, which is done by duplicating a gray level image from a computer screen onto the SLM display. These experiments also directly demonstrate that SHG from a single and well-defined nano-structure can be controlled at will. For instance, one can instantaneously switch from strong to weak longitudinal electric field on the optical axis, therefore switching on and off SHG at the location of the nanowire. The gradual spatial shifting of the SHG main peak observed in **Paper II** might also be interesting for precise coupling of light into nano-structures close to each other [159] without mechanical intervention or sample displacement.

As of now, it is hard to link these two techniques even though variations in SHG distribution might show similarities for both phase-shaping schemes. It is indeed not straightforward to associate a certain phase applied over a full lobe in **Paper I** to a certain π coverage ratio over a lobe in **Paper II**. It is also important to note that the orientation of the GaAs nanowires allows us to probe only the longitudinal electric field distribution at focus, whereas transverse components cannot be probed in this configuration as demonstrated by the lack of SHG using an AP excitation beam (see Fig. 6.1). However, the local SOP within the focal volume has a 3D behavior, and transverse electric field components are often still dominant over the longitudinal one. Therefore, our technique allows for longitudinal field control but also suggests that we can achieve further control over the polarization orientation in 3D at focus [39, 42].

7. CONTROL OF THE DEPTH OF FIELD OF LONGITUDINAL ELECTRIC FIELDS

In the previous Chapter, we presented a simple phase-shaping scheme for controlling the spatial distribution of longitudinal electric fields at a given transverse plane at focus. In this Chapter, we discuss the results of **Paper III** and **Paper IV** that address the question of the longitudinal extent of longitudinal electric fields. We are interested in knowing if this extent could potentially be controlled. For this reason, we decided to investigate the properties of the longitudinal electric field components of Bessel beams, known to show extended depth of field. We first introduce the notion of Bessel beams and their potential use in optics. We then present the results obtained by exciting our GaAs nanowires with LP and RPBG beams and discuss the possible opportunities offered by extended longitudinal electric fields.

7.1 Experimental results

In this section, we describe the results of **Paper III** and **Paper IV**. We first report on the longitudinal electric field properties of a LPBG beam compared to a common LP Gaussian beam (HG_{00}). We then generate an RPBG beam to create an optical needle that is probed using SHG from GaAs nanowires. As mentioned before, the detection part remains the same, only the method used to generate Bessel beams with various polarizations changes.

7.1.1 Comparison of LP Gaussian and LPBG beams

We decided to first create a LPBG beam at the focus of our high NA microscope objective and compare its longitudinal electric field distribution to that of a LP Gaussian beam. The generation of the Bessel beam was described in Section 5.2.2. To probe the longitudinal electric fields generated at focus, we performed similar

SHG transverse scans as described previously for **Paper I** and **Paper II**. This time, we collected SHG from single GaAs nanowires for different axial planes, that is to say, for different positions of the sample along the longitudinal direction. The first set of scans was recorded using a LP Gaussian beam and a second set using a LPBG beam, this in order to compare their respective depths of field as well as the transverse spatial distribution of their longitudinal field component. The main results are presented in Fig. 7.1

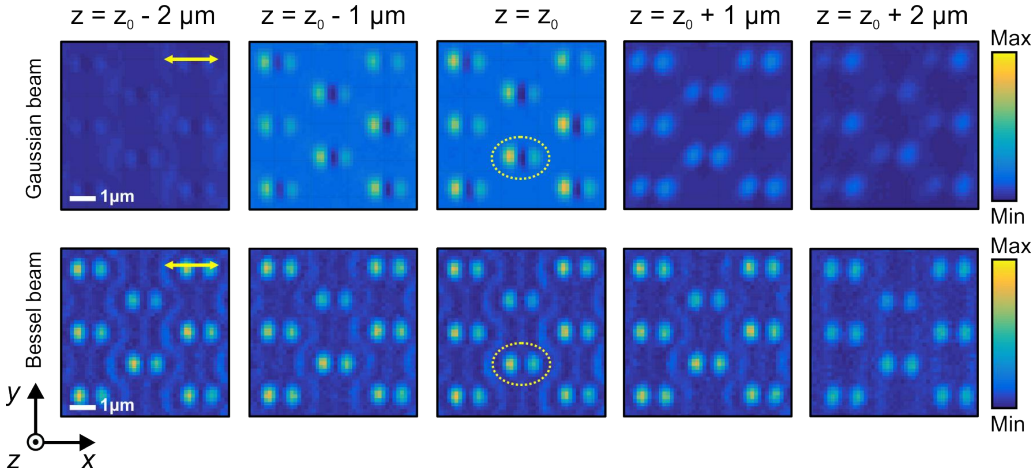

Figure 7.1 *Transverse SHG intensity maps, for different planes, from GaAs comparing the spatial distribution and depth of field of focused LP Gaussian and Bessel beams. Figure adapted, with permission, from* ***Paper III****.*

For each beam, we first acquired a SHG transverse scan for a plane where GaAs gave maximum signal (z_0). Using a LP Gaussian beam, we see that the two-lobed distribution of the longitudinal electric field observed in Figs. 6.2 and 6.3 is recovered in the top row of Fig. 7.1. Using a LPBG beam, the SHG intensity distribution from a single GaAs suggests that such a beam possesses a longitudinal electric field component at focus similar to a Gaussian beam with two off-axis lobes. Interestingly, we can notice two dimmer extra features next to the two main lobes on the SHG intensity maps using a Bessel beam, which can be explained by the high intensity first ring of the Bessel beam intensity profile, seen in Fig. 2.2, and confirmed by simulations [160]. From this position z_0, we then performed, for both beams, a series of transverse SHG scans for different axial planes before and after the position z_0. From these, we can already see that if we move more than $\pm 1 \mu m$ away from the position z_0, the contrast and the homogeneity of the two-lobed SHG from a single nanowires quickly deteriorates using a Gaussian beam. On the other hand, the two-lobed distribution is preserved over the axial range studied when using a Bessel

beam, suggesting the stability and extended depth of field of the longitudinal field component. In Fig. 7.2, we pushed the experiments further and tried to reach the limits of contrast. For the specific Bessel beam used in our experiments, the SHG signal distribution, directly linked to the longitudinal electric field distribution, is maintained over a 15 μm displacement, whereas the characteristic SHG signals from single GaAs nanowires disappear after a 6-8 μm range using a Gaussian beam.

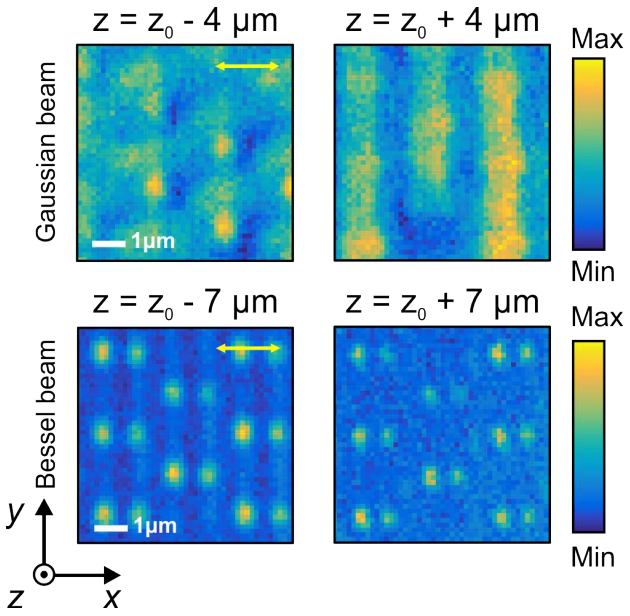

Figure 7.2 *Transverse SHG intensity maps from GaAs at the limit of contrast using focused LP Gaussian and Bessel beams. Figure adapted, with permission, from* ***Paper III****.*

7.1.2 Optical needle

After experimentally confirming the extended depth of the longitudinal electric field of LPBG beams and noticing their similar transverse spatial distribution with Gaussian beams with the same SOP, we decided to create RPBG beams to generate a spot-like extended longitudinal electric field, defined as optical needle. Optical needle is a term used to denote longitudinal electric fields, showing spot-like and sub-wavelength transverse resolution, that can be maintained over a distance of several λ. It is important to note that the precise definition of an "optical needle" can, however, have several meanings in the literature and can also be applied to extended transversely polarized electric fields [161, 162].

Methods, based on RP beams, have theoretically predicted the generation of optical needles using well-designed amplitude or phase belt-filters [163–167] to favor

constructive and destructive interferences at focus. In our case, we were interested in using RPBG beams to generate such optical needle, with techniques already described in Section 2.3.2, this in order to demonstrate the possibility to generate strong longitudinal electric field on the optical axis with tunable extent.

Regarding the experimental process, we probed the longitudinal field component using SHG from GaAs nanowires. We first imaged our GaAs nanowires using a common RP doughnut beam [36, 168] to have a reference. We performed a transverse xy raster scan and chose a set of three aligned nanowires to perform a longitudinal scan in the plane containing these nanowires (xz plane) as seen in Fig. 7.3 top row. The spot-like transverse distribution of SHG for the longitudinal field distribution of a tightly focused RP beam was recovered. The xz scan allowed us to probe the extent of the longitudinal electric field for each beam considered. For an RP beam, the full width at half maximum (FWHM) along the longitudinal axis is about $2\mu m$.

We then switched to an RPBG beam and completed the very same raster scans, with results displayed in Fig. 7.3 middle row. As expected, RP doughnut beam and RPBG beam show the same spot-like distribution of longitudinal electric field at focus. The characteristic first extra ring of an RPBG beam can be clearly seen in the SHG intensity map [169]. On the other hand, the xz SHG scan reveals that the longitudinal electric field distribution is perfectly maintained over the full 15 μm range with very good homogeneity without sacrificing the transverse resolution.

To further demonstrate that the optical needle generated by the RPBG beam was formed by mostly longitudinal electric field components, we performed the same SHG scans but this time using an APBG beam. To do so, we simply switched from RP to AP beam before the axicon using the radial converter. The goal here was to show, in analogy to **Paper I** and **Paper II**, that an APBG beam does not show longitudinal electric field components at focus [170] and that the optical needle generated using the RPBG beam was therefore purely longitudinally polarized on the optical axis. The results of this set of experiments are shown in Fig. 7.3 bottom row. As expected, GaAs nanowires did not respond to such excitation beam that shows only transverse field components at focus.

After successfully generating and probing such an extended longitudinal field, we decided to perform a scan over a broader range to observe the full extent of the longitudinal field created by our RPBG beam. In Fig. 7.4, which we display rotated by 90° to save space, we can see that the SHG response is rather constant over a

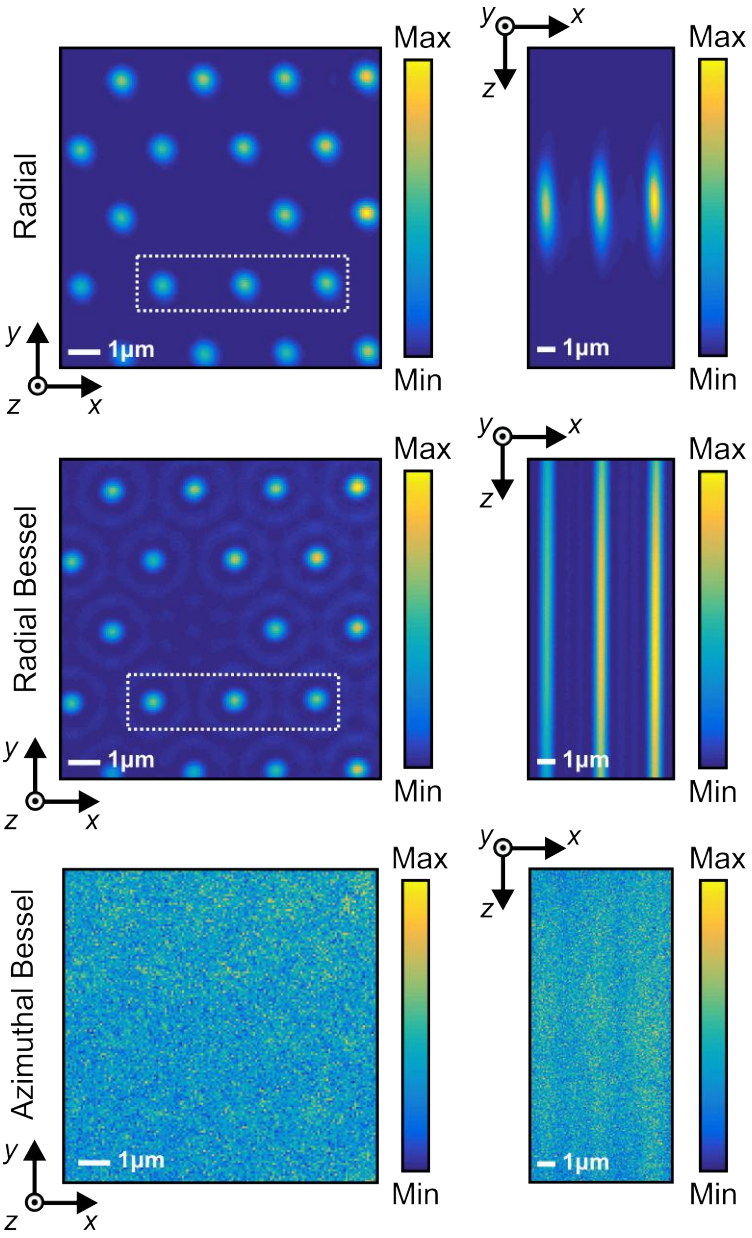

Figure 7.3 *SHG intensity maps of GaAs nanowires for xy and xz scans using RP doughnut beam, RPBG beam, and APBG beam. Figures adapted, with permission, from* ***Paper IV****.*

range of up to 50 μm, the maximum scan range available with our stage-scanner, suggesting the existence of a very long and longitudinally polarized optical needle. It is hard to evaluate the FWHM as some minor inhomogeneities can be observed along the needle, but it is reasonable to say that it is approximately in the 30 μm range.

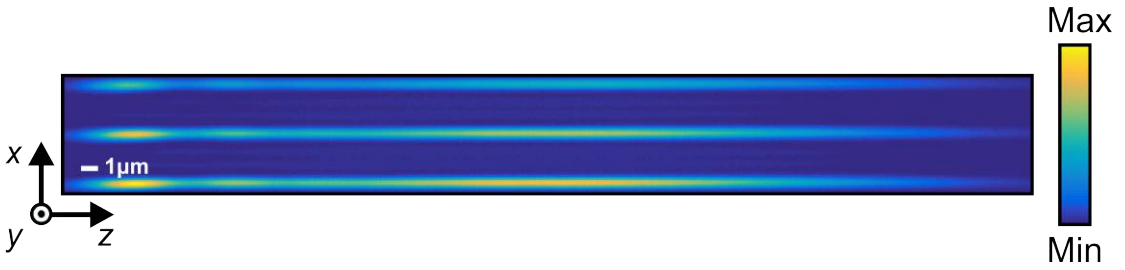

Figure 7.4 *Full range longitudinal SHG intensity maps of GaAs nanowires using an RPBG beam. Figure adapted, with permission, from* ***Paper IV****.*

7.2 Discussion

The results presented in **Paper III** and **Paper IV** extend the work of **Paper I** and **Paper II** by showing that the longitudinal electric field component can be controlled along the longitudinal direction itself by using special beams with different SOPs. By tuning the parameters of the generated Bessel beam at focus, one can control the extent of the longitudinal electric field at focus and even switch from weak on-axis longitudinal field using a LPBG beam to a pure longitudinally polarized optical needle on-axis using an RPBG beam.

It is important to note that the necessity to extend the depth of the longitudinal electric field component obviously depends on the application and might not always be beneficial. For instance in our experiments, we studied GaAs nanowires with an approximate length of 2 μm. First, this parameter determines the accuracy with which the actual depth of field at focus can be probed. Then, whether a LP or RPBG beam was used, SHG signals were always lower compared to their non-Bessel counterparts (Gaussian and RP doughnut beams). This can be explained by the depths of field of the non-Bessel beams to be almost ideal for the length of the GaAs nanowires at stake, the energy of such beams being concentrated roughly over 2 μm. On the other hand, their Bessel counterparts showed dramatically extended depths of field, the energy being therefore spread over a longer distance and thus reducing the efficiency of SHG in our case. However, it seems that the proportion of the longitudinal field components with respect to the transverse components is higher for Bessel beams than for non-Bessel beams [171], which would make one lean towards the use of a Bessel beam for exciting nano-objects sensitive to longitudinal electric fields. It would be interesting to study the influence of using longer nanowires on the SHG signal intensity and see if exciting these nanowires with an RPBG beam would turn out to provide higher SHG conversion than its non-Bessel counterpart.

Another interesting result comes from the full longitudinal scan of Fig. 7.4. We see that even though the needle generated is long, it shows some inhomogeneities. These variations have been modeled and explained in the literature by possible roundness of the axicon tip [91, 172]. Moreover, the interaction between the optical needle created and the GaAs nanowires might affect the homogenity of the optical needle probed. It is also important to remember that we probed the longitudinal electric field by the SHG response of GaAs. This means that the pixel-by-pixel SHG intensity detected and the local electric field of the fundamental beam at focus are linked by the relation $I(2\omega) \propto E(\omega)^4$. Thus, any small variation of $E(\omega)$ leads to noticeable variations in the SHG intensity. In our case, those variations, or oscillations, are contained in the 20% range in terms of SHG intensity, which means that the variations are contained in the 5% range in terms of electric field. This result suggests that the longitudinally polarized optical needle generated using the RPBG beam is of high quality and homogeneity.

It is important to remember that experimentally producing an infinitely long optical needle with sub-diffraction resolution is impossible due to physical limitations. Therefore, real Bessel beams are always approximated with a Gaussian profile in experiments, hence the name of BG or vector BG beams. In the end, the length of the optical needle and its structure can be tailored or affected by several parameters that can be tuned to achieve a specific goal. These include the NA of the microscope objective used to form the RPBG beam at focus, the thickness of the ring generated at the back focal plane, its size compared to the entrance pupil, and the precision with which it is situated at the back focal plane of the microscope objective. the influence of such parameters are well-described by Dehez [171]. These parameters also need to be considered if the goal is to create an optical needle where most of the total input electric field is converted into longitudinal field components at focus, with very little energy left in the transverse components. In our case, the needle is only formed by the longitudinal electric field on the optical axis, as transverse field components form a doughnut around the optical axis at focus [173]. However, it is hard to probe precisely the amount of remaining transverse field as our vertically aligned GaAs nanowires are not sensitive to such components.

Generally speaking, the demonstration of longitudinally polarized optical needles is interesting in the context of optical data storage where a long depth of field can provide larger data density as well as better tolerance for beam focusing [174, 175]. In the context of micromanipulation, a possible extension to previous works could

be to use a longitudinally polarized optical needle to trap several metallic particles [81]. The longitudinally polarized needle constitutes a field that does not propagate along the apparent main direction of propagation. It therefore does not contribute to the energy flow and allows for a stable trap for metallic particles, now free from scattering/absorption forces pushing them out of focus.

8. CONCLUSIONS AND OUTLOOK

In this Thesis, we have demonstrated the tailoring of longitudinal electric fields at the focus of a high NA microscope objective. We have demonstrated methods to tune the parameters of an input beam before focusing using phase modulations of different types. The experimental verification of the tailored fields was performed by exploiting the SHG properties of vertically aligned GaAs nanowires and the preference of this process for longitudinal electric fields. It allowed us to probe the longitudinal electric field distribution of our tailored beams at focus.

Our results provide insights on various levels. First, it shows that the longitudinal electric field at focus, and further polarization in 3D, can be controlled through phase-shaping of the input beam. Secondly, it confirms that longitudinal electric fields play a major role in nonlinear microscopy and that such nonlinear effects can be controlled on-demand via beam shaping for various purposes. Finally, aside from the possible challenges of fabricating high quality nanowires, SHG of vertically standing GaAs nanowires seems to be a superior method to directly image the distribution of longitudinal electric fields at focus.

In **Paper I**, we introduced a technique involving spatial phase-shaping of an HG_{10} mode with a SLM. It was shown that we are able to vary the spatial distribution of the longitudinal electric field at focus, switching from a three to two-lobed distribution by adding phase modulation between 0 and π, with symmetrical variations observed with phase modulations between π and 2π. The technique developed in **Paper II** offered an alternative to the one introduced in **Paper I**, and was based on binary phase-shaping of the same HG_{10} mode with the π phase coverage of the input beam being the key factor. Both techniques showed similar results in terms of SHG intensity variations and therefore in terms of longitudinal field control, even though these techniques are fundamentally different in their nature. In terms of possible applications, one could use such a system to quickly switch from strong to weak longitudinal electric field on the optical axis to control SHG form a single parti-

cle without mechanical intervention. More interestingly, such phase-shaping scheme could also be relevant to selectively excite and collect information from nano-objects. This technique is also potentially able to perform all-optical 3D polarization control at focus.

In **Paper III** and **Paper IV**, we investigated possible ways to tune the extent of longitudinal electric fields along the optical axis. We started by using a LPBG beam, and pushed the study to generate a longitudinally polarized optical needle using an RPBG beam. Several methods have been suggested to generate such optical needles, the ultimate goal being to convert most of the input transverse electric field into longitudinal electric field at focus. Our work here can only claim to have generated longitudinally polarized optical needle on the optical axis and cannot give much information regarding the amount of transverse field off-axis. However, compared to previous works that only suggested such optical needles theoretically, our work provides reliable experimental demonstration of optical needles generated by RPBG beams. Our results also show direct implications for enhancing SHG of axially extended single particles or rapid volumetric imaging of thick samples excited preferentially with longitudinal electric fields. Our work also puts vector Bessel beams on a pedestal for further development in optical trapping and data storage.

The work presented in this Thesis already provides a lot of potential for further applications in various fields of optics, ranging from nonlinear optical microscopy to optical trapping or data encryption. This work also leaves a lot of room for further improvement and development. All the results reported in the publications that are included in this Thesis are intrinsically linked together and constitute the core for future techniques that combine all the aspects developed so far. Our interest in the future will be focused on possible ways to generate foci with random locations, polarization orientations, and tunable axial extents in 3D, which are based on our all-optical phase-shaping setup. For instance, a possible improvement of our phase shaping technique to achieve 3D polarization control at focus could come from implementing spatial phase shaping, using one or two SLMs, of HG_{10} and HG_{01} modes, to be then combined and tightly focused. Another possibility could be to apply spatial phase shaping with an SLM onto the LP beam before going through the radial converter. These implementations would allow us to manipulate the longitudinal electric field distribution and possibly the direction of polarization in 3D.

REFERENCES

[1] W. C. McCrone, L. B. McCrone, and J. G. Delly, *Polarized light microscopy.* Ann Arbor Science Publishers, 1978, p. 251.

[2] Y. Barad, H. Eisenberg, M. Horowitz, and Y. Silberberg, "Nonlinear scanning laser microscopy by third harmonic generation", *Applied Physics Letters*, vol. 70, p. 922, 1998.

[3] W. R. Zipfel, R. M. Williams, and W. W. Webb, "Nonlinear magic: multiphoton microscopy in the biosciences", *Nature Biotechnology*, vol. 21, pp. 1369–1377, 2003.

[4] P. Campagnola and L. Loew, "Second-harmonic imaging microscopy for visualizing biomolecular arrays in cells, tissues and organisms", *Nature Biotechnology*, vol. 21, pp. 1356–1360, 2003.

[5] S. Yue, M. Slipchenko, and J. Cheng, "Multimodal nonlinear optical microscopy", *Laser & Photonics Reviews*, vol. 5, pp. 496–512, 2011.

[6] Y. Wang, C.-Y. Lin, A. Nikolaenko, V. Raghunathan, and E. O. Potma, "Four-wave mixing microscopy of nanostructures", *Advances in Optics and Photonics*, vol. 3, pp. 1–52, 2011.

[7] R. W. Boyd, *Nonlinear Optics.* Academic, 2008, p. 613.

[8] D. G. Hall, "Vector-beam solutions of Maxwell's wave equation", *Optics Letters*, vol. 21, pp. 9–11, 1996.

[9] B. Richards and E. Wolf, "Electromagnetic diffraction in optical systems. II. Structure of the image field in an aplanatic system", *Proceedings of the Royal Society of London Ser. A:*, vol. 253, pp. 358–379, 1959.

[10] K. S. Youngworth and T. G. Brown, "Focusing of high numerical aperture cylindrical-vector beams", *Optics Express*, vol. 7, pp. 77–87, 2000.

[11] R. Dorn, S. Quabis, and G. Leuchs, "Sharper focus for a radially polarized light beam", *Physical Review Letters*, vol. 91, p. 233 901, 2003.

[12] Q. Zhan, "Cylindrical vector beams: from mathematical concepts to applications", *Advances in Optics and Photonics*, vol. 1, pp. 1–57, 2009.

[13] T. G. Brown, "Unconventional polarization states: beam propagation, focusing, and imaging", *Progress in Optics*, vol. 56, pp. 81–129, 2011.

[14] J.-X. Cheng, L. D. Book, and X. S. Xie, "Polarization coherent anti-Stokes Raman scattering microscopy", *Optics Letters*, vol. 26, pp. 1341–1343, 2001.

[15] D. Oron, E. Tal, and Y. Silberberg, "Depth-resolved multiphoton polarization microscopy by third-harmonic generation", *Optics Letters*, vol. 28, pp. 2315–2317, 2003.

[16] N. Olivier, F. Aptel, K. Plamann, M.-C. Schanne-Klein, and E. Beaurepaire, "Harmonic microscopy of isotropic and anisotropic microstructure of the human cornea", *Optics Express*, vol. 18, pp. 5028–5040, 2010.

[17] N. Olivier, M. A. Luengo-Oroz, L. Duloquin, E. Faure, T. Savy, I. Veilleux, X. Solinas, D. Débarre, P. Bourgine, A. Santos, N. Peyriéras, and E. Beaurepaire, "Cell lineage reconstruction of early zebrafish embryos using label-free nonlinear microscopy", *Science*, vol. 329, pp. 967–971, 2010.

[18] F. Munhoz, H. Rigneault, and S. Brasselet, "High order symmetry structural properties of vibrational resonances using multiple-field polarization coherent anti-Stokes Raman spectroscopy microscopy", *Physical Review Letters*, vol. 105, p. 123 903, 2010.

[19] M. J. Huttunen, G. Bautista, M. Decker, S. Linden, M. Wegener, and M. Kauranen, "Nonlinear chiral imaging of subwavelength-sized twisted-cross gold nanodimers", *Optical Materials Express*, vol. 1, pp. 46–56, 2011.

[20] M. Zimmerley, P. Mahou, D. Débarre, M.-C. Schanne-Klein, and E. Beaurepaire, "Probing ordered lipid assemblies with polarized third-harmonic generation microscopy", *Physical Review X*, vol. 3, p. 011 002, 2013.

[21] G. Bautista, S. G. Pfisterer, M. J. Huttunen, S. Ranjan, K. Kanerva, E. Ikonen, and M. Kauranen, "Polarized THG microscopy identifies compositionally different lipid droplets in mammalian cells", *Biophysical Journal*, vol. 107, pp. 2230–2236, 2014.

[22] Y. Han, J. Hsu, N.-H. Ge, and E. O. Potma, "Polarization-sensitive sum-frequency generation microscopy of collagen fibers", *The Journal of Physical Chemistry B*, vol. 119, pp. 3356–3365, 2015.

[23] L. Novotny, M. R. Beversluis, K. S. Youngworth, and T. G. Brown, "Longitudinal field modes probed by single molecules", *Physical Review Letters*, vol. 86, p. 5251, 2001.

[24] A. V. Failla, H. Qian, H. Qian, A. Hartschuh, and A. J. Meixner, "Orientational imaging of subwavelength Au particles with higher order laser modes", *Nano Letters*, vol. 6, pp. 1374–1378, 2006.

[25] M. Fleischer, C. Stanciu, F. Stade, J. Stadler, K. Braun, A. Heeren, M. Häffner, D. P. Kern, and A. J. Meixner, "Three-dimensional optical antennas: Nanocones in an apertureless scanning near-field microscope", *Applied Physics Letters*, vol. 93, p. 111 114, 2008.

[26] H. Ishitobi, I. Nakamura, N. Hayazawa, Z. Sekkat, and S. Kawata, "Orientational imaging of single molecules by using azimuthal and radial polarizations", *The Journal of Physical Chemistry B*, vol. 114, pp. 2565–2571, 2010.

[27] K. Yoshiki, M. Hashimoto, and T. Araki, "Second-harmonic generation microscopy using excitation beam with controlled polarization pattern to determine three-dimensional molecular orientation", *Japanese Journal of Applied Physics*, vol. 44, pp. L1066–L1068, 2005.

[28] E. Yew and C. Sheppard, "Second harmonic generation polarization microscopy with tightly focused linearly and radially polarized beams", *Optics Communications*, vol. 275, pp. 453–457, 2007.

[29] F. Lu, W. Zheng, and Z. Huang, "Coherent anti-Stokes Raman scattering microscopy using tightly focused radially polarized light", *Optics Letters*, vol. 34, pp. 1870–1872, 2009.

[30] G. Bautista, M. J. Huttunen, J. M. Kontio, J. Simonen, and M. Kauranen, "Third- and second-harmonic generation microscopy of individual metal nanocones using cylindrical vector beams", *Optics Express*, vol. 21, pp. 21 918–21 923, 2013.

[31] G. Bautista and M. Kauranen, "Vector-field nonlinear microscopy of nanostructures", *ACS Photonics*, vol. 3, pp. 1351–1370, 2016.

[32] G. Bautista, M. J. Huttunen, J. Mäkitalo, J. M. Kontio, J. Simonen, and M. Kauranen, "Second-harmonic generation imaging of metal nano-objects with cylindrical vector beams", *Nano Letters*, vol. 12, pp. 3207–3212, 2012.

[33] G. Bautista, C. Dreser, X. Zang, D. P. Kern, M. Kauranen, and M. Fleischer, "Collective effects in second-harmonic generation from plasmonic oligomers", *Nano Letters*, vol. 18, pp. 2571–2580, 2018.

[34] A. Bouhelier, M. Beversluis, A. Hartschuh, and L. Novotny, "Near-field second-harmonic generation induced by local field enhancement", *Physical Review Letters*, vol. 90, p. 013 903, 2003.

[35] E. Yew and C. Sheppard, "Effects of axial field components on second harmonic generation microscopy", *Optics Express*, vol. 14, pp. 1167–1174, 2006.

[36] G. Bautista, J. Mäkitalo, Y. Chen, V. Dhaka, M. Grasso, L. Karvonen, H. Jiang, M. J. Huttunen, T. Huhtio, H. Lipsanen, and M. Kauranen, "Second-harmonic generation imaging of semiconductor nanowires with focused vector beams", *Nano Letters*, vol. 15, pp. 1564–1569, 2015.

[37] S. N. Khonina and S. G. Volotovsky, "Controlling the contribution of the electric field components to the focus of a high-aperture lens using binary phase structures", *Journal of the Optical Society of America A*, vol. 27, pp. 2188–2197, 2010.

[38] F. Kenny, D. Lara, O. G. Rodríguez-Herrera, and C. Dainty, "Complete polarization and phase control for focus-shaping in high-NA microscopy", *Optics Express*, vol. 20, pp. 14 015–14 029, 2012.

[39] X. Li, T.-H. Lan, C.-H. Tien, and M. Gu, "Three-dimensional orientation-unlimited polarization encryption by a single optically configured vectorial beam", *Nature Communications*, vol. 3, p. 998, 2012.

[40] W. Zhu and W. She, "Generation of tunable three-dimensional polarization in 4Pi focusing system", *Optics Express*, vol. 21, pp. 17 265–17 274, 2013.

[41] T. Bauer, P. Banzer, E. Karimi, S. Orlov, A. Rubano, L. Marrucci, E. Santamato, R. W. Boyd, and G. Leuchs, "Observation of optical polarization Mobius strips", *Science*, vol. 347, pp. 964–966, 2015.

[42] G. Rui, J. Chen, X. Wang, B. Gu, Y. Cui, and Q. Zhan, "Synthesis of focused beam with controllable arbitrary homogeneous polarization using engineered vectorial optical fields", *Optics Express*, vol. 24, pp. 23 667–23 676, 2016.

[43] A. Bouhelier, M. R. Beversluis, and L. Novotny, "Near-field scattering of longitudinal fields", *Applied Physics Letters*, vol. 82, pp. 4596–4598, 2003.

[44] K. G. Lee, H. W. Kihm, J. E. Kihm, W. J. Choi, H. Kim, C. Ropers, D. J. Park, Y. C. Yoon, S. B. Choi, D. H. Woo, J. Kim, B. Lee, Q. H. Park, C. Lienau, and D. S. Kim, "Vector field microscopic imaging of light", *Nature Photonics*, vol. 1, pp. 53–56, 2007.

[45] T. Grosjean, I. A. Ibrahim, M. A. Suarez, G. W. Burr, M. Mivelle, and D. Charraut, "Full vectorial imaging of electromagnetic light at subwavelength scale", *Optics Express*, vol. 18, pp. 5809–5824, 2010.

[46] S. Quabis, R. Dorn, M. Eberler, O. Glöckl, and G. Leuchs, "The focus of light - theoretical calculation and experimental tomographic reconstruction", *Applied Physics B*, vol. 72, pp. 109–113, 2014.

[47] T. Bauer, S. Orlov, U. Peschel, P. Banzer, and G. Leuchs, "Nanointerferometric amplitude and phase reconstruction of tightly focused vector beams", *Nature Photonics*, vol. 8, pp. 23–27, 2014.

[48] J. C. Maxwell, "A dynamical theory of the electromagnetic Field", *Philosophical Transactions of the Royal Society of London*, vol. 155, pp. 459–512, 1865.

[49] O. Heaviside, *Electromagnetic theory*. London, "The Electrician" printing and publishing company, limited, 1894.

[50] W. H. McMaster, "Polarization and the Stokes Parameters", *American Journal of Physics*, vol. 22, pp. 351–362, 1954.

[51] H. Kogelnik and T. Li, "Laser beams and resonators", *Applied Optics*, vol. 5, pp. 1550–1567, 1966.

[52] S. C. Tidwell, D. H. Ford, and W. D. Kimura, "Generating radially polarized beams interferometrically", *Applied Optics*, vol. 29, pp. 2234–2239, 1990.

[53] S. Tripathi and K. Toussaint, "Versatile generation of optical vector fields and vector beams using a non-interferometric approach", *Optics Express*, vol. 20, pp. 10 788–10 795, 2012.

[54] D. Pohl, "Operation of a ruby laser in the purely transverse electric mode TE01", *Applied Physics Letters*, vol. 20, pp. 266–267, 1972.

[55] R. Oron, S. Blit, N. Davidson, A. A. Friesem, Z. Bomzon, and E. Hasman, "The formation of laser beams with pure azimuthal or radial polarization", *Applied Physics Letters*, vol. 77, p. 3322, 2000.

[56] Y. Kozawa and S. Sato, "Generation of a radially polarized laser beam by use of a conical Brewster prism", *Optics Letters*, vol. 30, pp. 3063–3065, 2005.

[57] K. Yonezawa, Y. Kozawa, and S. Sato, "Generation of a radially polarized laser beam by use of the birefringence of a c-cut Nd:YVO4 crystal", *Optics Letters*, vol. 31, pp. 2151–2153, 2006.

[58] G. Machavariani, Y. Lumer, I. Moshe, A. Meir, S. Jackel, and N. Davidson, "Birefringence-induced bifocusing for selection of radially or azimuthally polarized laser modes", *Applied Optics*, vol. 46, pp. 3304–3310, 2007.

[59] D. Naidoo, F. S. Roux, A. Dudley, I. Litvin, B. Piccirillo, L. Marrucci, and A. Forbes, "Controlled generation of higher-order Poincaré sphere beams from a laser", *Nature Photonics*, vol. 10, pp. 327–332, 2016.

[60] M. Stalder and M. Schadt, "Linearly polarized light with axial symmetry generated by liquid-crystal polarization converters", *Optics Letters*, vol. 21, pp. 1948–1950, 1996.

[61] T. Grosjean, D. Courjon, and M. Spajer, "An all-fiber device for generating radially and other polarized light beams", *Optics Communications*, vol. 203, pp. 1–5, 2002.

[62] G. Machavariani, Y. Lumer, I. Moshe, A. Meir, and S. Jackel, "Spatially-variable retardation plate for efficient generation of radially- and azimuthally-polarized beams", *Optics Communications*, vol. 281, pp. 732–738, 2008.

[63] M. Beresna, M. Gecevičius, P. G. Kazansky, and T. Gertus, "Radially polarized optical vortex converter created by femtosecond laser nanostructuring of glass", *Applied Physics Letters*, vol. 98, p. 201 101, 2011.

[64] F. Cardano, E. Karimi, S. Slussarenko, L. Marrucci, C. de Lisio, and E. Santamato, "Polarization pattern of vector vortex beams generated by q-plates with different topological charges", *Applied Optics*, vol. 51, pp. C1–C6, 2012.

[65] K. C. Toussaint, S. Park, J. E. Jureller, and N. F. Scherer, "Generation of optical vector beams with a diffractive optical element interferometer", *Optics Letters*, vol. 30, pp. 2846–2848, 2005.

[66] N. Passilly, F. Treussart, R. Hierle, R. de Saint Denis, K. Aït-Ameur, and J.-F. Roch, "Simple interferometric technique for generation of a radially polarized light beam", *Journal of the Optical Society of America A*, vol. 22, pp. 984–991, 2005.

[67] C. Maurer, A. Jesacher, S. Fürhapter, S. Bernet, and M. Ritsch-Marte, "Tailoring of arbitrary optical vector beams", *New Journal of Physics*, vol. 9, p. 78, 2007.

[68] T. Wang, S. Fu, S. Zhang, C. Gao, and F. He, "A Sagnac-like interferometer for the generation of vector beams", *Applied Physics B*, vol. 122, p. 231, 2016.

[69] B. Perez-Garcia, C. López-Mariscal, R. I. Hernandez-Aranda, and J. C. Gutiérrez-Vega, "On-demand tailored vector beams", *Applied Optics*, vol. 56, pp. 6967–6972, 2017.

[70] R. Yamaguchi, T. Nose, and S. Sato, "Liquid crystal polarizers with axially symmetrical properties", *Japanese Journal of Applied Physics*, vol. 28, pp. 1730–1731, 1989.

[71] L. Marrucci, C. Manzo, and D. Paparo, "Optical spin-to-orbital angular momentum conversion in inhomogeneous anisotropic media", *Physical Review Letters*, vol. 96, p. 163 905, 2006.

[72] S. Slussarenko, A. Murauski, T. Du, V. Chigrinov, L. Marrucci, and E. Santamato, "Tunable liquid crystal q-plates with arbitrary topological charge", *Optics Express*, vol. 19, pp. 4085–4090, 2011.

[73] E. Karimi, B. Piccirillo, E. Nagali, L. Marrucci, and E. Santamato, "Efficient generation and sorting of orbital angular momentum eigenmodes of light by thermally tuned q-plates", *Applied Physics Letters*, vol. 94, p. 231 124, 2009.

[74] V. D'Ambrosio, F. Baccari, S. Slussarenko, L. Marrucci, and F. Sciarrino, "Arbitrary, direct and deterministic manipulation of vector beams via electrically-tuned q-plates", *Scientific Reports*, vol. 5, p. 7840, 2015.

[75] J. A. Davis, N. Hashimoto, M. Kurihara, E. Hurtado, M. Pierce, M. M. Sánchez-López, K. Badham, and I. Moreno, "Analysis of a segmented q-plate tunable retarder for the generation of first-order vector beams", *Applied Optics*, vol. 54, pp. 9583–9590, 2015.

[76] Y. Shimotsuma, P. G. Kazansky, J. Qiu, and K. Hirao, "Self-organized nanogratings in glass irradiated by ultrashort light pulses", *Physical Review Letters*, vol. 91, p. 247 405, 2003.

[77] W. Han, Y. Yang, W. Cheng, and Q. Zhan, "Vectorial optical field generator for the creation of arbitrarily complex fields", *Optics Express*, vol. 21, pp. 20 692–20 706, 2013.

[78] S. Zhou, S. Wang, J. Chen, G. Rui, and Q. Zhan, "Creation of radially polarized optical fields with multiple controllable parameters using a vectorial optical field generator", *Photonics Research*, vol. 4, B35–B39, 2016.

[79] S. Liu, S. Qi, Y. Zhang, P. Li, D. Wu, L. Han, and J. Zhao, "Highly efficient generation of arbitrary vector beams with tunable polarization, phase, and amplitude", *Photonics Research*, vol. 6, pp. 228–233, 2018.

[80] A. Arbabi, Y. Horie, M. Bagheri, and A. Faraon, "Dielectric metasurfaces for complete control of phase and polarization with subwavelength spatial resolution and high transmission", *Nature Nanotechnology*, vol. 10, pp. 937–943, 2015.

[81] Q. Zhan, "Trapping metallic Rayleigh particles with radial polarization", *Optics Express*, vol. 12, pp. 3377–3382, 2004.

[82] Y. Kozawa and S. Sato, "Optical trapping of micrometer-sized dielectric particles by cylindrical vector beams", *Optics Express*, vol. 18, pp. 10 828–10 833, 2010.

[83] V. G. Niziev and A. V. Nesterov, "Influence of beam polarization on laser cutting efficiency", *Journal of Physics D: Applied Physics*, vol. 32, pp. 1455–1461, 1999.

[84] Y. Zhao and J. Wang, "High-base vector beam encoding/decoding for visible-light communications", EN, *Optics Letters*, vol. 40, p. 48 434 846, 2015.

[85] C. Sheppard and T. Wilson, "Gaussian-beam theory of lenses with annular aperture", *IEE Journal on Microwaves, Optics and Acoustics*, vol. 2, p. 105, 1978.

[86] J. Durnin, "Exact solutions for nondiffracting beams I The scalar theory", *Journal of the Optical Society of America A*, vol. 4, pp. 651–654, 1987.

[87] J. Durnin, J. Miceli, and J. H. Eberly, "Diffraction-free beams", *Physical Review Letters*, vol. 58, pp. 1499–1501, 1987.

[88] J. H. McLeod, "The axicon: A new type of optical element", *Journal of the Optical Society of America*, vol. 44, pp. 592–597, 1954.

[89] G. Indebetouw, "Nondiffracting optical fields: some remarks on their analysis and synthesis", *Journal of the Optical Society of America A*, vol. 6, pp. 150–152, 1989.

[90] G. Scott, "Efficient generation of nearly diffraction-free beams using an axicon", *Optical Engineering*, vol. 31, p. 2640, 1992.

[91] O. Brzobohatý, T. Cižmár, and P. Zemánek, "High quality quasi-Bessel beam generated by round-tip axicon", *Optics Express*, vol. 16, pp. 12 688–12 700, 2008.

[92] A. Vasara, J. Turunen, and A. T. Friberg, "Realization of general nondiffracting beams with computer-generated holograms", *Journal of the Optical Society of America A*, vol. 6, pp. 1748–1754, 1989.

[93] N. Chattrapiban, E. A. Rogers, D. Cofield, W. T. Hill III, and R. Roy, "Generation of nondiffracting Bessel beams by use of a spatial light modulator", *Optics Letters*, vol. 28, pp. 2183–2185, 2003.

[94] J. A. Davis, J. Guertin, and D. M. Cottrell, "Diffraction-free beams generated with programmable spatial light modulators", *Applied Optics*, vol. 32, pp. 6368–6370, 1993.

[95] I. Moreno, J. A. Davis, M. M. Sánchez-López, K. Badham, and D. M. Cottrell, "Nondiffracting Bessel beams with polarization state that varies with propagation distance", *Optics Letters*, vol. 40, pp. 5451–5454, 2015.

[96] R. H. Jordan and D. G. Hall, "Free-space azimuthal paraxial wave equation: the azimuthal BesselâGauss beam solution", *Optics Letters*, vol. 19, pp. 427–429, 1994.

[97] Z. Bouchal and M. Olivík, "Non-diffractive vector Bessel beams", *Journal of Modern Optics*, vol. 42, pp. 1555–1566, 1995.

[98] A. Dudley, Y. Li, T. Mhlanga, M. Escuti, and A. Forbes, "Generating and measuring nondiffracting vector Bessel beams", *Optics Letters*, vol. 38, pp. 3429–3432, 2013.

[99] G. Wu, F. Wang, and Y. Cai, "Generation and self-healing of a radially polarized Bessel-Gauss beam", *Physical Review A*, vol. 89, p. 043 807, 2014.

[100] G. Milione, A. Dudley, T. A. Nguyen, O. Chakraborty, E. Karimi, A. Forbes, and R. R. Alfano, "Measuring the self-healing of the spatially inhomogeneous states of polarization of vector Bessel beams", *Journal of Optics*, vol. 17, p. 035 617, 2015.

[101] Y. Zhang, L. Wang, and C. Zheng, "Vector propagation of radially polarized Gaussian beams diffracted by an axicon", *Journal of the Optical Society of America A*, vol. 22, pp. 2542–2546, 2005.

[102] D. N. Schimpf, W. P. Putnam, M. D. W. Grogan, S. Ramachandran, and F. X. Kärtner, "Radially polarized Bessel-Gauss beams: decentered Gaussian beam analysis and experimental verification", *Optics Express*, vol. 21, pp. 18 469–18 483, 2013.

[103] J. Arlt, V. Garces-Chavez, W. Sibbett, and K. Dholakia, "Optical micromanipulation using a Bessel light beam", *Optics Communications*, vol. 197, pp. 239–245, 2001.

[104] F. Courvoisier, J. Zhang, M. K. Bhuyan, M. Jacquot, and J. M. Dudley, "Applications of femtosecond Bessel beams to laser ablation", *Applied Physics A: Materials Science and Processing*, vol. 112, pp. 29–34, 2013.

[105] C. Yu, M. R. Wang, A. J. Varela, and B. Chen, "High-density non-diffracting beam array for optical interconnection", *Optics Communications*, vol. 177, pp. 369–376, 2000.

[106] F. O. Fahrbach, P. Simon, and A. Rohrbach, "Microscopy with self-reconstructing beams", *Nature Photonics*, vol. 4, pp. 780–785, 2010.

[107] L. Gao, L. Shao, B.-C. Chen, and E. Betzig, "3D live fluorescence imaging of cellular dynamics using Bessel beam plane illumination microscopy", *Nature Protocols*, vol. 9, pp. 1083–1101, 2014.

[108] N. Olivier, D. Débarre, P. Mahou, and E. Beaurepaire, "Third-harmonic generation microscopy with Bessel beams: a numerical study", *Optics Express*, vol. 20, pp. 14 703–14 715, 2012.

[109] G. Thériault, Y. De Koninck, and N. McCarthy, "Extended depth of field microscopy for rapid volumetric two-photon imaging", *Optics Express*, vol. 21, pp. 10 095–10 104, 2013.

[110] N. Vuillemin, P. Mahou, D. Débarre, T. Gacoin, P.-L. Tharaux, M.-C. Schanne-Klein, W. Supatto, and E. Beaurepaire, "Efficient second-harmonic imaging of collagen in histological slides using Bessel beam excitation", *Scientific Reports*, vol. 6, p. 29 863, 2016.

[111] L. Novotny and B. Hecht, *Principles of Nano-Optics*. Cambridge University, 2012, p. 564.

[112] A. F. Abouraddy and K. C. Toussaint, "Three-dimensional polarization control in microscopy", *Physical Review Letters*, vol. 96, p. 153 901, 2006.

[113] M. R. Beversluis, L. Novotny, and S. J. Stranick, "Programmable vector point-spread function engineering", *Optics Express*, vol. 14, pp. 2650–2656, 2006.

[114] L. Zhu, M. Sun, D. Zhang, J. Yu, J. Wen, and J. Chen, "Multifocal array with controllable polarization in each focal spot", *Optics Express*, vol. 23, pp. 24 688–24 698, 2015.

[115] T. Grosjean and D. Courjon, "Photopolymers as vectorial sensors of the electric field", *Optics Express*, vol. 14, pp. 2203–2210, 2006.

[116] S. Brasselet, "Polarization-resolved nonlinear microscopy: application to structural molecular and biological imaging", *Advances in Optics and Photonics*, vol. 3, pp. 205–271, 2011.

[117] Y. R. Shen, "Surface properties probed by second-harmonic and sum-frequency generation", *Nature*, vol. 337, pp. 519–525, 1989.

[118] M. Moewe, L. C. Chuang, S. Crankshaw, C. Chase, and C. Chang-Hasnain, "Atomically sharp catalyst-free wurtzite GaAs/AlGaAs nanoneedles grown on silicon", *Applied Physics Letters*, vol. 93, p. 023 116, 2008.

[119] R. Chen, S. Crankshaw, T. Tran, L. C. Chuang, M. Moewe, and C. Chang-Hasnain, "Second-harmonic generation from a single wurtzite GaAs nanoneedle", *Applied Physics Letters*, vol. 96, p. 051 110, 2010.

[120] S. Carrasco, B. E. A. Saleh, M. C. Teich, and J. T. Fourkas, "Second- and third-harmonic generation with vector Gaussian beams", *Journal of the Optical Society of America B*, vol. 23, pp. 2134–2141, 2006.

[121] D. P. Biss and T. G. Brown, "Polarization-vortex-driven second-harmonic generation", *Optics Letters*, vol. 28, pp. 923–925, 2003.

[122] K. Yoshiki, K. Ryosuke, M. Hashimoto, N. Hashimoto, and T. Araki, "Second-harmonic-generation microscope using eight-segment polarization-mode converter to observe three-dimensional molecular orientation", *Optics Letters*, vol. 32, pp. 1680–1682, 2007.

[123] T. Ehmke, T. H. Nitzsche, A. Knebl, and A. Heisterkamp, "Molecular orientation sensitive second harmonic microscopy by radially and azimuthally polarized light", *Biomedical Optics Express*, vol. 5, pp. 2231–2246, 2014.

[124] J. A. Squier, M. Müller, G. J. Brakenhoff, and K. R. Wilson, "Third harmonic generation microscopy", *Optics Express*, vol. 3, pp. 315–324, 1998.

[125] D. Débarre, W. Supatto, A.-M. Pena, A. Fabre, T. Tordjmann, L. Combettes, M.-C. Schanne-Klein, and E. Beaurepaire, "Imaging lipid bodies in cells and tissues using third-harmonic generation microscopy", *Nature Methods*, vol. 3, pp. 47–53, 2006.

[126] O. Schwartz and D. Oron, "Background-free third-harmonic imaging of gold nanorods", *Nano Letters*, vol. 9, pp. 4093–4097, 2009.

[127] O. Masihzadeh, P. Schlup, and R. A. Bartels, "Enhanced spatial resolution in third-harmonic microscopy through polarization switching", *Optics Letters*, vol. 34, pp. 1240–1242, 2009.

[128] S. Yang and Q. Zhan, "Third-harmonic generation microscopy with tightly focused radial polarization", *Journal of Optics A: Pure and Applied Optics*, vol. 10, p. 125 103, 2008.

[129] O. Masihzadeh, P. Schlup, and R. A. Bartels, "Control and measurement of spatially inhomogeneous polarization distributions in third-harmonic generation microscopy", *Optics Letters*, vol. 34, pp. 1090–1092, 2009.

[130] N. Olivier and E. Beaurepaire, "Third-harmonic generation microscopy with focus-engineered beams: a numerical study", *Optics Express*, vol. 16, pp. 14 703–14 715, 2008.

[131] M. M. And and J. M. Schins, "Imaging the thermodynamic state of lipid membranes with multiplex CARS microscopy", *Journal of Physical Chemistry B*, vol. 106, pp. 3715–3723, 2002.

[132] C. L. Evans, X. Xu, S. Kesari, X. S. Xie, S. T. C. S. T. Wong, and G. S. Young, "Chemically-selective imaging of brain structures with CARS microscopy", EN, *Optics Express*, vol. 15, p. 12 076, 2007.

[133] J. P. Pezacki, J. A. Blake, D. C. Danielson, D. C. Kennedy, R. K. Lyn, and R. Singaravelu, "Chemical contrast for imaging living systems: molecular vibrations drive CARS microscopy", *Nature Chemical Biology*, vol. 7, pp. 137–145, 2011.

[134] V. V. Krishnamachari and E. O. Potma, "Focus-engineered coherent anti-Stokes Raman scattering microscopy: a numerical investigation", *Journal of the Optical Society of America A*, vol. 24, pp. 1138–1147, 2007.

[135] J. Lin, K. Zi Jian Er, W. Zheng, and Z. Huang, "Radially polarized tip-enhanced near-field coherent anti-Stokes Raman scattering microscopy for vibrational nano-imaging", *Applied Physics Letters*, vol. 103, p. 083 705, 2013.

[136] J. Lin, F. Lu, H. Wang, W. Zheng, C. J. Sheppard, and Z. Huang, "Improved contrast radially polarized coherent anti-Stokes Raman scattering microscopy using annular aperture detection", *Applied Physics Letters*, vol. 95, p. 133 703, 2009.

[137] H. Dehez, M. Piché, and Y. De Koninck, "Enhanced resolution in two-photon imaging using a TM01 laser beam at a dielectric interface", *Optics Letters*, vol. 34, pp. 3601–3603, 2009.

[138] Y. Kozawa, D. Matsunaga, and S. Sato, "Superresolution imaging via superoscillation focusing of a radially polarized beam", *Optica*, vol. 5, pp. 86–92, 2018.

[139] H. Dehez, M. Piché, and Y. De Koninck, "Resolution and contrast enhancement in laser scanning microscopy using dark beam imaging", *Optics Express*, vol. 21, pp. 15 912–15 925, 2013.

[140] H. Kang, B. Jia, J. Li, D. Morrish, and M. Gu, "Enhanced photothermal therapy assisted with gold nanorods using a radially polarized beam", *Applied Physics Letters*, vol. 96, p. 063 702, 2010.

[141] M. Gu, H. Lin, and X. Li, "Parallel multiphoton microscopy with cylindrically polarized multifocal arrays", *Optics Letters*, vol. 38, pp. 3627–3630, 2013.

[142] D. G. Grier, "A revolution in optical manipulation", *Nature*, vol. 424, pp. 810–816, 2003.

[143] R. Lynge Eriksen, V. Ricardo Daria, J. Glückstad, R. Eriksen, V. Daria, and J. Gluckstad, "Fully dynamic multiple-beam optical tweezers", *Optics Express*, vol. 10, pp. 597–602, 2002.

[144] J. Leach, G. Sinclair, P. Jordan, J. Courtial, M. J. Padgett, J. Cooper, and Z. J. Laczik, "3D manipulation of particles into crystal structures using holographic optical tweezers", *Optics Express*, vol. 12, pp. 220–226, 2004.

[145] H. Ono, H. Wakabayashi, T. Sasaki, A. Emoto, T. Shioda, and N. Kawatsuki, "Vector holograms using radially polarized light", *Applied Physics Letters*, vol. 94, p. 071 114, 2009.

[146] J. A. Davis, D. E. McNamara, D. M. Cottrell, and T. Sonehara, "Two-dimensional polarization encoding with a phase-only liquid-crystal spatial light modulator", *Applied Optics*, vol. 39, pp. 1549–1554, 2000.

[147] G. Bautista, M. J. Romero, G. Tapang, and V. R. Daria, "Parallel two-photon photopolymerization of microgear patterns", *Optics Communications*, vol. 282, pp. 3746–3750, 2009.

[148] H. Lin, B. Jia, and M. Gu, "Dynamic generation of Debye diffraction-limited multifocal arrays for direct laser printing nanofabrication", *Optics Letters*, vol. 36, pp. 406–408, 2011.

[149] P. Kunwar, L. Turquet, J. Hassinen, R. H. A. Ras, J. Toivonen, and G. Bautista, "Holographic patterning of fluorescent microstructures comprising silver nanoclusters", *Optical Materials Express*, vol. 6, pp. 946–951, 2016.

[150] C. Maurer, A. Jesacher, S. Bernet, and M. Ritsch-Marte, "What spatial light modulators can do for optical microscopy", *Laser & Photonics Reviews*, vol. 5, pp. 81–101, 2011.

[151] M. J. Booth, "Adaptive optical microscopy: the ongoing quest for a perfect image", *Light: Science & Applications*, vol. 3, e165, 2014.

[152] V. R. Daria, C. Stricker, R. Bowman, S. Redman, and H.-A. Bachor, "Arbitrary multisite two-photon excitation in four dimensions", *Applied Physics Letters*, vol. 95, p. 093 701, 2009.

[153] A. Libster-Hershko, S. Trajtenberg-Mills, and A. Arie, "Dynamic control of light beams in second harmonic generation", *Optics Letters*, vol. 40, pp. 1944–1947, 2015.

[154] L. Novotny, E. J. Sánchez, and X. Sunney Xie, "Near-field optical imaging using metal tips illuminated by higher-order Hermite-Gaussian beams", *Ultramicroscopy*, vol. 71, pp. 21–29, 1998.

[155] S. M. Sze and K. K. Ng, *Physics of semiconductor devices*. Wiley-Interscience, 2007, p. 815.

[156] G. Bautista, J.-P. Kakko, V. Dhaka, X. Zang, L. Karvonen, H. Jiang, E. Kauppinen, H. Lipsanen, and M. Kauranen, "Nonlinear microscopy using cylindrical vector beams: Applications to three-dimensional imaging of nanostructures", *Optics Express*, vol. 25, pp. 12 463–12 468, 2017.

[157] G. Machavariani, N. Davidson, A. A. Ishaaya, A. A. Friesem, and E. Hasman, "Efficient formation of a high-quality beam from a pure high-order Hermite-Gaussian mode", *Optics Letters*, vol. 27, pp. 1501–1503, 2002.

[158] A. A. Ishaaya, G. Machavariani, N. Davidson, A. A. Friesem, and E. Hasman, "Conversion of a high-order mode beam into a nearly Gaussian beam by use of a single interferometric element", *Optics Letters*, vol. 28, pp. 504–506, 2003.

[159] J.-P. Kakko, T. Haggrén, V. Dhaka, T. Huhtio, A. Peltonen, H. Jiang, E. Kauppinen, and H. Lipsanen, "Fabrication of dual-type nanowire arrays on a single substrate", *Nano Letters*, vol. 15, pp. 1679–1683, 2015.

[160] S. N. Khonina, S. V. Karpeev, S. V. Alferov, D. A. Savelyev, J. Laukkanen, and J. Turunen, "Experimental demonstration of the generation of the longitudinal E-field component on the optical axis with high-numerical-aperture binary axicons illuminated by linearly and circularly polarized beams", *Journal of Optics*, vol. 15, p. 085 704, 2013.

[161] F. Qin, K. Huang, J. Wu, J. Jiao, X. Luo, C. Qiu, and M. Hong, "Shaping a Subwavelength Needle with Ultra-long Focal Length by Focusing Azimuthally Polarized Light", *Scientific Reports*, vol. 5, p. 9977, 2015.

[162] Z. Man, C. Min, L. Du, Y. Zhang, S. Zhu, and X. Yuan, "Sub-wavelength sized transversely polarized optical needle with exceptionally suppressed sidelobes", *Optics Express*, vol. 24, pp. 874–882, 2016.

[163] H. Wang, L. Shi, B. Lukyanchuk, C. Sheppard, and C. T. Chong, "Creation of a needle of longitudinally polarized light in vacuum using binary optics", *Nature Photonics*, vol. 2, pp. 501–505, 2008.

[164] K. Huang, P. Shi, X.-l. Kang, X. Zhang, and Y.-p. Li, "Design of DOE for generating a needle of a strong longitudinally polarized field", *Optics Letters*, vol. 35, pp. 965–967, 2010.

[165] K. Rajesh, N. V. Suresh, P. Anbarasan, K. Gokulakrishnan, and G. Mahadevan, "Tight focusing of double ring shaped radially polarized beam with high NA lens axicon", *Optics & Laser Technology*, vol. 43, pp. 1037–1040, 2011.

[166] Y. Zha, J. Wei, H. Wang, and F. Gan, "Creation of an ultra-long depth of focus super-resolution longitudinally polarized beam with a ternary optical element", *Journal of Optics*, vol. 15, p. 075 703, 2013.

[167] Z. Nie, G. Shi, X. Zhang, Y. Wang, and Y. Song, "Generation of super-resolution longitudinally polarized beam with ultra-long depth of focus using radially polarized hollow Gaussian beam", *Optics Communications*, vol. 331, pp. 87–93, 2014.

[168] L. Turquet, J.-P. Kakko, X. Zang, L. Naskali, L. Karvonen, H. Jiang, T. Huhtio, E. Kauppinen, H. Lipsanen, M. Kauranen, and G. Bautista, "Tailorable second-harmonic generation from an individual nanowire using spatially phase-shaped beams", *Laser & Photonics Reviews*, vol. 11, p. 1 600 175, 2017.

[169] T. Grosjean and D. Courjon, "Smallest focal spots", *Optics Communications*, vol. 272, pp. 314–319, 2007.

[170] M. Ornigotti and A. Aiello, "Radially and azimuthally polarized nonparaxial Bessel beams made simple", *Optics Express*, vol. 21, pp. 15 530–15 537, 2013.

[171] H. Dehez, A. April, and M. Piché, "Needles of longitudinally polarized light: guidelines for minimum spot size and tunable axial extent", *Optics Express*, vol. 20, pp. 14 891–14 905, 2012.

[172] T. Čižmár and K. Dholakia, "Tunable Bessel light modes: engineering the axial propagation", *Optics Express*, vol. 17, pp. 15 558–15 570, 2009.

[173] Z. Nie, G. Shi, D. Li, X. Zhang, Y. Wang, and Y. Song, "Tight focusing of a radially polarized Laguerre-Bessel-Gaussian beam and its application to manipulation of two types of particles", *Physics Letters A*, vol. 379, pp. 857–863, 2015.

[174] T. Grosjean, D. Courjon, and C. Bainier, "Smallest lithographic marks generated by optical focusing systems", *Optics Letters*, vol. 32, pp. 976–978, 2007.

[175] Y. Zhang and J. Bai, "Improving the recording ability of a near-field optical storage system by higher-order radially polarized beams", *Optics Express*, vol. 17, pp. 3698–3706, 2009.

ORIGINAL PAPERS

I

Tailorable second-harmonic generation from an individual nanowire using spatially phase-shaped beams

by

Léo Turquet, Joona-Pekko Kakko, Xiaorun Zang, Liisa Naskali, Lasse Karvonen, Hua Jiang, Teppo Huhtio, Esko Kauppinen, Harri Lipsanen, Martti Kauranen, and Godofredo Bautista, 2017

Laser & Photonics Reviews vol. 11, p. 1600175

LASER
& PHOTONICS
REVIEWS

Laser Photonics Rev. **11,** No. 1, 1600175 (2017) / **DOI** 10.1002/lpor.201600175

Abstract The ability to control the optical field in the vicinity of an individual nano-object is an obvious stepping-stone in the tailoring of light-matter interactions at the nanoscale. Earlier reports on tailoring light fields in the vicinity of a nano-object have been restricted by their dependence on cumbersome optical or fabrication techniques, have relied mostly on in-plane electric field polarizations, and have been demonstrated only for bulk materials and structures with strong in-plane anisotropies. In addition, traditional methods for manipulating the longitudinal electric fields are significantly hindered by the lack of appropriate probes that can be used to unambiguously measure or calibrate the light coupling efficiency to nano-objects. Here, we demonstrate such a possibility for the specific case of optical second-harmonic generation (SHG). Our technique relies on spatial phase-shaping of a high-order laser beam to tailor the longitudinal fields at the beam focus and allows SHG from an individual and well-defined vertically-aligned GaAs nanowire to be manipulated on demand. Our technique is applicable to tailoring the efficiency of nonlinear emission on the nanoscale and to arbitrary polarization control at the beam focus in general.

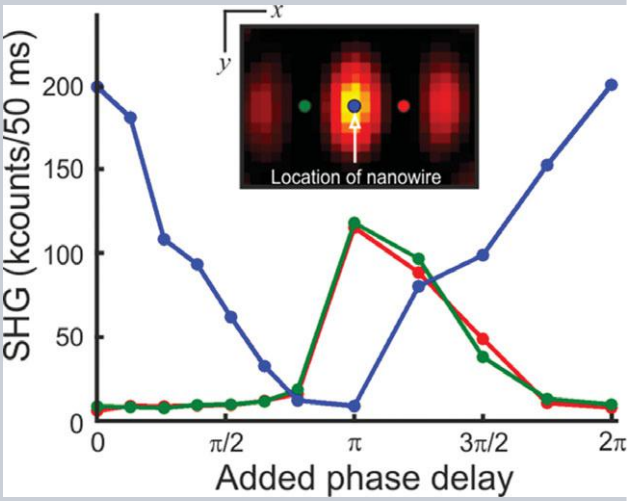

ORIGINAL PAPER

Tailorable second-harmonic generation from an individual nanowire using spatially phase-shaped beams

Léo Turquet[1], Joona-Pekko Kakko[2], Xiaorun Zang[1], Liisa Naskali[1], Lasse Karvonen[2], Hua Jiang[3], Teppo Huhtio[2], Esko Kauppinen[3], Harri Lipsanen[2], Martti Kauranen[1], and Godofredo Bautista[1,*]

1. Introduction

The control of optical excitations is expected to revolutionize light-matter interactions on the nanoscale. With the use of optical antennas [1, 2], light can now be confined to subwavelength-sized regions [3], frequency converted [4, 5], and even spatially redirected [6, 7]. An emerging way to control optical excitations is based on engineering the incident light field before it impinges on the nano-object. Indeed, it has been reported that tailoring the properties of optical fields [8–15], can be used to spatially confine light in the vicinity of nano-objects or enhance emission from such structures. Beam shaping schemes for tuning the linear and nonlinear optical effects in nano-objects are becoming more common, as demonstrated for nonlinear crystals [16–19], metasurfaces [20], nanoholes [21–24], metamaterials [25, 26], metal tips [27], as well as coupled [28, 29], and single [30, 31] nano-objects with strong in-plane anisotropies. However, tailoring the nonlinear emission from a single nano-object at the subwavelength scale using simple all-optical methods and without the need of modifying the physical properties of the sample remains a big challenge.

For years, there has been a tremendous amount of fundamental and applied research on semiconductor nanowires due to their intriguing properties [32, 33]. Prior studies have shown that efficient coupling of light into a nanowire usually requires an electric field component along the long axis of the wire [33–35]. Recently, we have shown that a convenient way to excite and address individual vertically-aligned nanowires, corresponding to their native growth environment, is through the use of cylindrically symmetric vector beams [36] such as radially polarized beams [37]. Tight focusing of radial polarization leads to a strong electric field component along the direction of beam propagation, usually referred to as the longitudinal component [38–42], which has been particularly favorable for several linear and nonlinear imaging modalities that rely on molecular orientation or symmetry as the source of contrast [43–49]. Beyond imaging applications, it is also worth noting that the longitudinal fields produced by focusing radial polarization and other high-order beams, such as

[1] Department of Physics, Tampere University of Technology, P.O. Box 692, FI-33101 Tampere, Finland
[2] Department of Micro and Nanosciences, Aalto University, P.O. Box 13500, FI-00076 Aalto, Finland
[3] Department of Applied Physics and Nanomicroscopy Center, Aalto University, P.O. Box 15100, FI-00076 Aalto, Finland
*Corresponding author: E-mail: godofredo.bautista@tut.fi

linearly polarized Hermite-Gaussian beams of order (1,0) (HG_{10}), can be used to optically trap microparticles [50], process subwavelength-sized features in metals [51], induce mass transport in solid films [52], accelerate particles along the beam propagation axis [53], and influence nonlinear phenomena [54–56].

It is evident that methods to manipulate the longitudinal field at the beam focus are gaining increasing importance. For example, by using another type of cylindrically symmetric vector beam with azimuthal polarization, the longitudinal field can be fully suppressed [57]. Indeed, it has been shown that symmetry-selective nonlinear optical processes such as second-harmonic generation (SHG) from a nano-object can be selectively turned "on" or "off" by focusing radial or azimuthal polarizations [37, 47]. More recently, discrimination of certain multipole resonances in dielectric nanoparticles have been made possible by a similar scheme [14]. So far, several approaches that are based on strong focusing [40, 58], annular illumination [39, 59, 60], inverse Cherenkov effect [61], plasmonic lenses [62, 63], and binary optics [64] have been developed to enhance the longitudinal field or to promote its coupling to the nano-object. Up to date, most of these techniques have been cumbersome and their efficiency difficult to calibrate in any meaningful way. Most importantly, the demonstrated techniques do not support on-demand control of the desired effect. Therefore, the ability to create and manipulate the longitudinal field or in general an arbitrary optical field at the beam focus whenever necessary is an obvious stepping-stone in the tailoring of light-matter interactions at the nanoscale.

In this work, we demonstrate a technique for tailoring SHG from an individual nano-object. We show that by spatially phase-shaping a HG_{10} beam, we can selectively control the efficiency of SHG from a vertically-oriented gallium arsenide (GaAs) nanowire at the beam focus with a 50-fold contrast ratio. Our work provides direct evidence that the longitudinal fields at the focal plane can be manipulated by spatial phase modulation. The technique therefore has broader implications for more general situations, where the coupling of light to nanoscale objects needs to be precisely controlled. The present work relies on our earlier demonstration that SHG from a vertically-oriented GaAs nanowire is driven primarily by the longitudinal fields at the beam focus [37]. We utilize this understanding of the origin of the SHG response of nanowires to demonstrate for the first time precise tailoring of SHG from a single nanowire based on controlling the longitudinal fields produced by focusing spatially phase-shaped beams. Furthermore, in the previous study, the SHG signals were not tailorable since the longitudinal fields produced by focusing conventional beam polarizations were not precisely or easily controllable and the nanowires exhibited significant variations [37]. The present work therefore provides a significant advance both in the technique and in the material system as it demonstrates that the longitudinal field-driven SHG signals from single and well-defined nanowires can be precisely controlled through simple phase shaping of the incident beam.

2. Materials and methods

In order to demonstrate the manipulation of longitudinal fields at the beam focus, this first demonstration was based on semiconducting nanowires that protrude out of the substrate. During their fabrication, such nanowires grow out of the substrate, implying that the protruding orientation provides their native environment. Such pristine nanowire systems have been shown to be highly promising platforms for energy management [65] and biological processes [66].

Our nanowire samples were grown with selective-area metallo-organic vapour phase epitaxy (SA-MOVPE) on GaAs (111)B substrates with a Thomas Swan system [67]. First, a 40 nm thick amorphous silicon oxide layer was deposited on a cleaned substrate with plasma-enhanced chemical vapour deposition (Oxford Systems Plasmalab 80Plus). The deposited layer acts as a growth mask. Subsequently, the oxide was patterned with arrays of holes in a triangular lattice with the pitch of 2.45 μm and the diameter of 55 nm. Electron beam lithography (EBL) (Vistec EPBG500pEs) and reactive ion etching (Oxford Systems Plasmalab 80Plus) were used to pattern the holes. Prior to the nanowire growth, the sample was annealed at the growth temperature for 5 min under tertiary-butyl arsine (TBAs) flow. H_2 was used as the carrier gas and the total flow rate was fixed to 5 slm. The nanowire growth was performed at 760 °C for 5 min, with trimethylgallium (TMGa) and TBAs as the precursors for Ga and As, respectively. The TMGa and TBAs flows were fixed to 0.8 μmol min^{-1} and 227.0 μmol min^{-1} during the nanowire growth, respectively. Scanning electron microscopy (SEM), high resolution (scanning) transmission electron microscopy (TEM/STEM), and electron diffraction (ED) were used to determine the dimensions and crystallinity of the fabricated nanowires. TEM/STEM and ED experiments were carried out with a double aberration-corrected JEOL-2200FS microscope (JEOL Ltd.) operated at 200 kV. The microscope is equipped with a Gatan 4k × 4k UltraScan 4000 CCD camera and a high-angle annular dark-field (HAADF) detector. The SEM images of the nanowires used in the SHG experiments are depicted in Figs. 1a and 1b. SEM showed that the fabricated nanowires are well-separated and have a diameter of 90 nm and length of 2.6 μm. TEM/STEM and ED revealed that the nanowires in the array are predominantly zinc-blende with numerous twin defects (Figs. 1c and 1d).

In order to evaluate the influence of tailored high-order beams on the SHG response of individual nanowires, we used a custom-built point-scanning epi-detection SHG microscope equipped with a mode-locked femtosecond laser (wavelength of 1060 nm, pulse length of 140 fs, repetition rate of 80 MHz) [37, 47]. After beam collimation and appropriate conditioning (see below), the beam was directed to an infinity-corrected (numerical aperture of 0.8, 50×) microscope objective. We overfilled the back-aperture of the objective in order to maximize the desired polarization components at the beam focus [58]. The objective was used to focus the beam onto the sample that was mounted

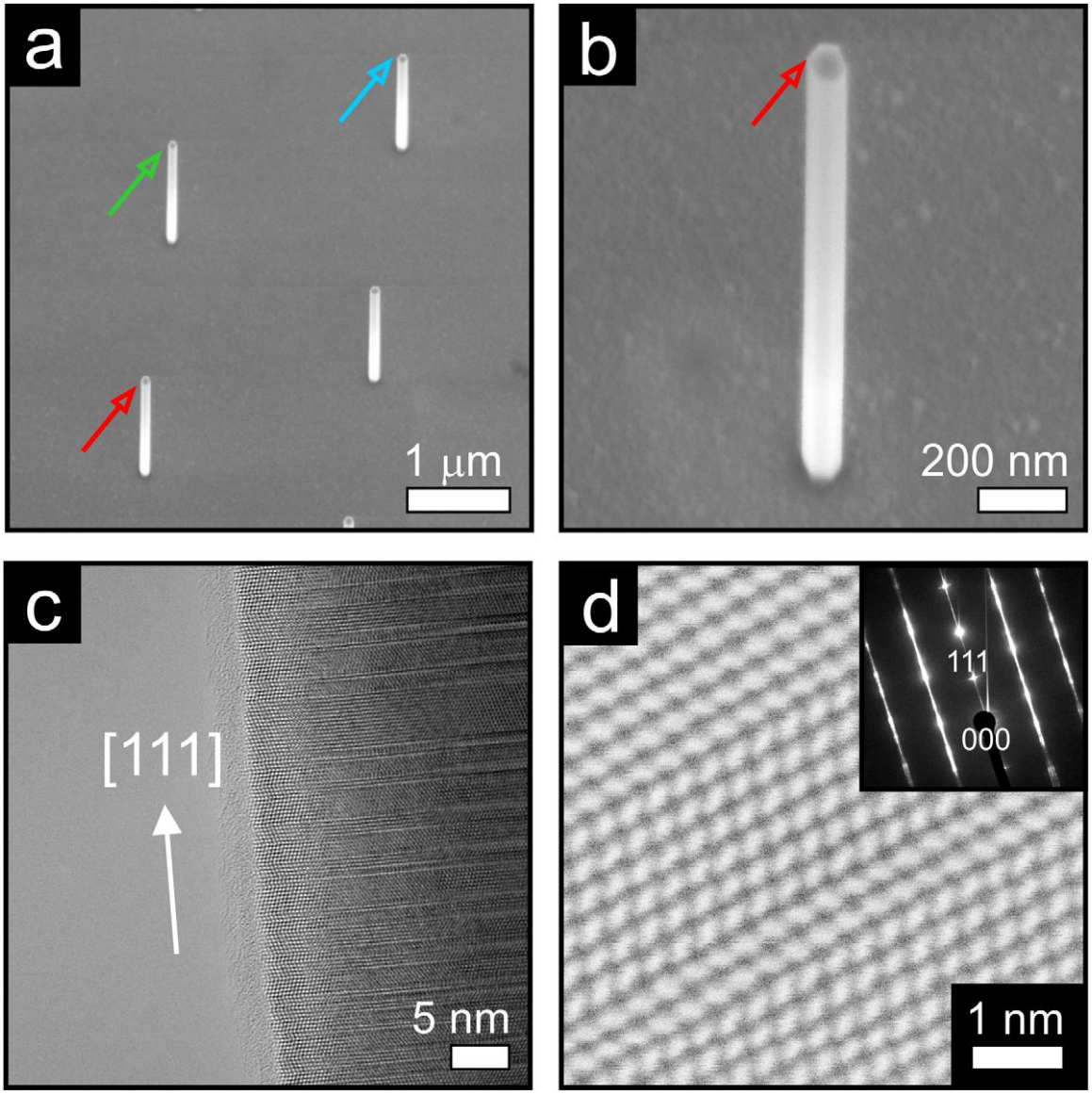

Figure 1 (**a**,**b**) Tilted SEM images of the vertically-aligned GaAs nanowires which were used in the SHG experiments. The nanowires have a typical diameter of 90 nm and a length of 2.6 μm. The relative locations of the nanowires are color-marked for clarity. Representative aberration-corrected high-resolution TEM (**c**) and STEM HAADF (**d**) images of a nanowire in the same array and its indexed ED pattern (inset in d). The nanowire grows along the [111] direction with plenty of microtwinned structure on the (111) planes.

on a computer-controlled three-axis piezo-scanning stage. All polarization components of the SHG signal were collected by the same objective, discriminated by appropriate dichroic filters from the fundamental excitation wavelength and directed onto a cooled photomultiplier tube. In order to acquire a point- or raster-scanned SHG image, the raw SHG signal is collected pixel-by-pixel and plotted as a function of spatial coordinates. Note that this scanning microscopy technique allows one to conveniently map the light distribution at the focal plane using appropriate optical probes [43]. In the present case, our nanowire probe is sensitive to the longitudinal field component. Equivalently, control of the longitudinal field allows the efficiency of SHG from individual nanowires to be controlled. All measurements were done at the average power level of 1 mW, a pixel dwell time of 50 ms, and room temperature. Data acquisition and analysis were performed using LabVIEW and MATLAB, accordingly. In our measurements, we have carefully considered the focusing geometry where the long axis of the nanowire is aligned in the direction of the resulting longitudinal electric field [37]. Furthermore, this focusing geometry allows the creation and subsequent manipulation of appropriate longitudinal fields that impinge on the nanowires. Prior to raster scan imaging, we verified that the SHG signal from an individual vertical GaAs nanowire exhibits the expected behavior in terms of routine nonlinear measurements such as power dependence, mode-lock dependence, spectral discrimination, and

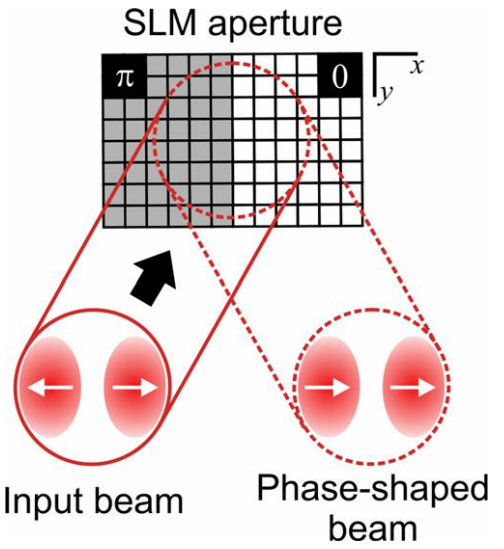

Figure 2 Spatial phase-shaping scheme that is based on a pixelated SLM and performed right before the excitation beam enters the microscope objective. Note that phase-only modulation is achieved by aligning the polarization of the incident light (along *x* or horizontal) with the orientation of the liquid crystal molecules of the SLM.

reproducibility (Figure S1). For reference and comparison, we restricted the scanning to a fixed region in the sample that contains a subset of nanowires (Fig. 1a).

Before entering the microscope objective, the excitation beam was manipulated in appropriate ways to create a linearly polarized HG_{10} beam of high purity. We first generated a radially-polarized doughnut beam using a polarization mode converter (Arcoptix, S.A.) and a spatial Fourier-filter in tandem and then selected from it the *x* linear polarization with a calcite Glan polarizer. Any slight deviation of the resulting HG_{10} beam from the ideal is attributed to impurities in the original doughnut mode. It is also important to note that other techniques exist to create an HG_{10} beam, but the chosen technique was most convenient to implement in our laboratory. The resulting HG_{10} beam was directed to the aperture of a reflective-type electrically-addressed phase-only spatial light modulator (SLM, Hamamatsu X10468-07) with a pixel resolution of 792×600, bit depth of 8, pixel pitch of 20 μm and fill factor of 98%. We opted for this approach because the SLM provides a high degree of flexibility as it eliminates the need for a variety of diffractive optical elements to achieve the desired shaping effects.

In the subsequent experiments, the full aperture of the SLM was artificially divided into two identical sub-apertures. The lobes of the incident HG_{10} beam were assigned to impinge symmetrically on the two sub-apertures (Fig. 2). After phase calibration at our fundamental wavelength of 1060 nm and careful alignment, appropriate phase delays ranging from 0 to 2π were applied between the two parts of the HG_{10} beam. For all of the phase levels used, we observed no changes in the beam profiles in propagation from the SLM to the back aperture of the microscope objective. This is as expected because the Rayleigh range of our beam is at least a factor of 100 longer than the distance between the SLM and the objective, and shows that we achieved pure phase modulation with the SLM. Consequently, independent control of the additional phase delays imparted on the two lobes of the incident HG_{10} beam permits us to demonstrate tuning of the resulting longitudinal field at the focus of the microscope objective. Although SLM's have been used to demonstrate phase and polarization shaping in a variety of nano-objects [8, 11–13, 18, 19, 21, 22, 24, 31], the application of SLMs to create and control the longitudinal field component at the beam focus and its coupling to an individual nano-object has not been demonstrated.

3. Results and discussion

It is well-known that the electric-dipole-allowed bulk response dominates SHG from noncentrosymmetric cubic media like GaAs [68]. The GaAs nanowire studied in our present work exhibits a zinc-blende symmetry and a growth axis along the [111] direction (Fig. 1c). In this case, the second-order susceptibility has only three nonvanishing tensor components: $\chi^{(2)}_{xyz}$, $\chi^{(2)}_{yzx}$ and $\chi^{(2)}_{zxy}$, where x, y, and z refer to the principal-axis system of the crystal ([100], [010], [001]). By performing appropriate coordinate transformations between the crystal and laboratory frames, we have shown previously that the electric field components parallel to the growth axis of the nanowire primarily drive its SHG [37]. Thus, in order to get an appreciable SHG signal from this nanowire configuration, nonvanishing longitudinal field components that arise from tight focusing geometry are needed. For reference, we first imaged the vertically-aligned GaAs nanowires using different tightly focused incident polarizations (Fig. 3). Here, the SLM was turned off and simply acted as a mirror. We also verified beforehand that this scheme reproduces the results obtained by bypassing the SLM at the otherwise same experimental settings.

As seen in Figs. 3a-c, the SHG signals from the nanowires are significantly higher than the background. For example, the SHG signals that are acquired from the GaAs substrate are $\sim$2 orders of magnitude lower than the SHG from the nanowires under radial polarization. These data agree with the previous results that SHG from GaAs nanowires is more efficient than from equivalent unstructured GaAs [37, 69–72]. In addition, strong SHG signals are only detected when the focusing geometry gives rise to nonvanishing longitudinal field components as expected from linear (Fig. 3a) and radial (Fig. 3b) polarizations [37] as well as a linearly-polarized HG_{10} beam (Fig. 3c). These SHG intensity maps were normalized according to the maximum SHG intensity that was detected using excitation with radial polarization, which produces the strongest longitudinal fields at the beam focus. Under linear (radial) polarization, the SHG image of the nanowire exhibits a two-lobed (spot-like) intensity pattern, resembling the longitudinal field

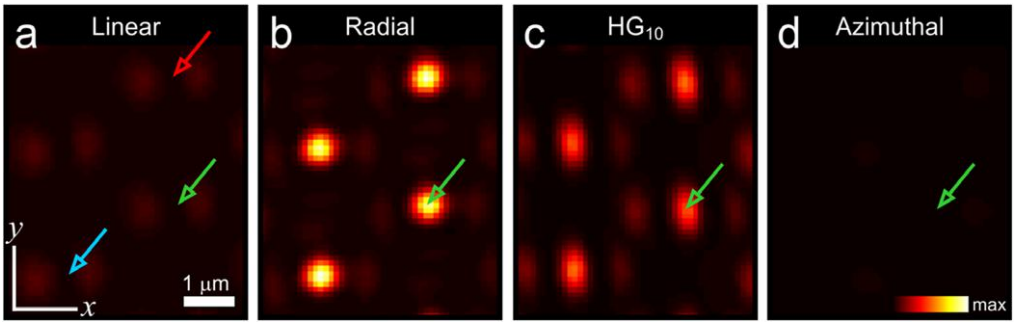

Figure 3 Raster-scanned SHG images from vertically-aligned GaAs nanowires (diameter of 90 nm, length of 2.6 μm) using focused (**a**) linear polarization along *x*, (**b**) radial polarization, (**c**) linearly-polarized HG_{10} beam with *x* polarization, and (**d**) azimuthal polarization under the same experimental settings. The relative locations of the nanowires are color-marked for clarity (see Fig. 1a for reference). The images are normalized to (b). The maximum SHG signal intensity is about 350,000 counts/50 ms under a 1 mW radially polarized beam.

distribution of the respective focal fields [38–40] (Figure S2). For further reference, we also acquired a SHG image of the same region using focused azimuthal polarization (Fig. 3d). The faintness of the signals here suggests that the resulting transverse field components at the focus of azimuthal polarization drive SHG from the nanowire only very weakly (Fig. S2). Under a HG_{10} beam, the SHG image of the nanowire resembles a three-lobed intensity pattern consisting of a bright central lobe and two additional lobes that are centered symmetrically with respect to the nanowire. This image qualitatively follows the predicted intensity distribution of the nonvanishing longitudinal fields of a HG_{10} beam along the beam axis as a consequence of strong focusing [27] (Figure S2). It should also be noted that even though the focused HG_{10} beam also contains transverse field components, they do not contribute significantly to SHG from the present nanowires. The resulting SHG intensity patterns in Fig. 3c are reminiscent of the observation of Bouhelier et al., who used SHG scattering from a metal tip to probe the intensity distribution of the longitudinal fields of a tightly focused HG_{10} beam [73]. Clearly, the highest signals from our data set are obtained using radial polarization since it provides the strongest longitudinal component at the beam focus.

Even though radial polarization provides the strongest longitudinal fields for coupling to our nanowires, we settled on using a linearly-polarized HG_{10} beam for this first proof-of-principle demonstration of phase shaping the incident beam. This is because, for phase-only modulation by the SLM, a fixed polarization is required. More importantly, a nonvanishing on-axis longitudinal field is always provided by a focused HG_{10} beam. We first examined the effects of uniformly phase-shaped HG_{10} beams on SHG from the same vertically-aligned nanowires. Upon reflection from the operational SLM, uniform phase delays were applied on the HG_{10} beam throughout its beam cross-section, i.e., the electric field components of the two lobes of the beam exhibit no relative phase delay. Shown in Fig. 4 are the SHG images for this series of experiments. For the additional phase delays of 0, π or 2π across the whole beam, the SHG image of an individual nanowire exhibits a three-lobed

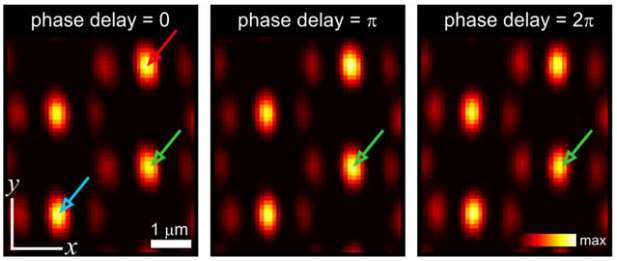

Figure 4 Raster-scanned SHG images of the same vertically-aligned nanowires illuminated by a focused *x*-polarized HG_{10} beam with uniform phase delays of 0, π or 2π applied simultaneously on the two lobes. The maximum SHG signal intensity is about 200,000 counts/50 ms under a 1 mW HG_{10} beam. The relative locations of the nanowires are color-marked for clarity (see Fig. 1a for reference).

intensity pattern [27,73], and remains unchanged compared to Fig. 3c. This is as expected, since there are no significant deviations in the optical field distributions of the two lobes of the incident HG_{10} beam. The longitudinal field produced at the beam focus is thus always nonvanishing, optimal, and remains the same for all additional phase delays.

Next, we illuminated the same nanowires using a spatially phase-shaped HG_{10} beam. Upon reflection from the SLM, only one lobe of the HG_{10} beam was imparted with an additional phase delay. In consequence, the electric field components of the two lobes oscillate at different phase when they enter the objective. Shown in Fig. 5 are the SHG images of the nanowires for this series of experiments. Again, when the additional phase delay between the two lobes is 0 or 2π, the SHG images resemble the results of Fig. 4 with maximum SHG intensity of about ~200,000 counts per 50 ms. Interestingly, when the additional phase delay between the two lobes is increased from 0 to π, the SHG image of a single nanowire changes from a three-lobed intensity pattern to a two-lobed intensity pattern. Moreover, unlike the uniformly phase-shaped beam cases (Fig. 4), the SHG image taken with an additional π phase delay between the two lobes now exhibits a minimum at the location of the

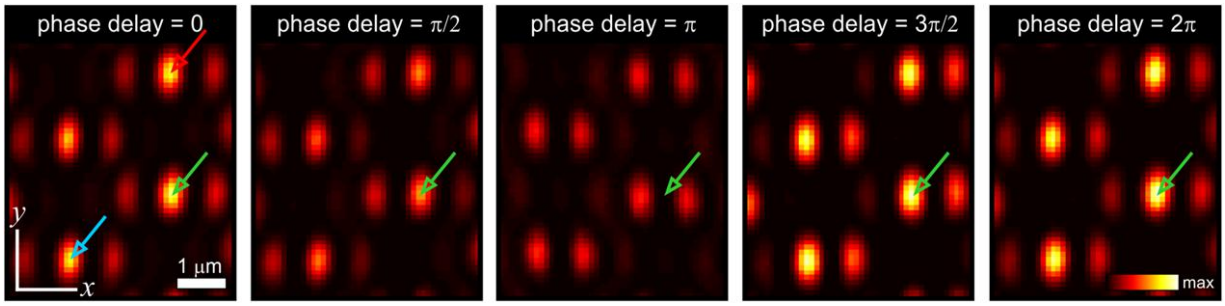

Figure 5 Raster-scanned SHG images of the same vertically-aligned nanowires for a focused *x*-polarized HG_{10} beam with varying additional phase delays between the two lobes. The reference beam is the unshaped HG_{10} mode, i.e., without an additional phase delay from the SLM. The relative locations of the nanowires are color-marked for clarity (see Fig. 1a for reference).

nanowire clearly indicating a drastic change in the coupling efficiency. We associate this reversal in the image contrast (∼50-fold) to the suppressed longitudinal field at the geometrical focus of the tailored beam. At this beam setting (with an additional π phase delay), the SHG signal at the center of the nanowires is at about the same level as the SHG signal from the substrate (∼4,000 counts per 50 ms).

Another important issue is that the two-lobed SHG intensity pattern achieved at an additional phase delay of π between the two lobes resembles the SHG intensity distribution due to the longitudinal fields at the focus of linear polarization (Fig. 3a). Note that under strong focusing conditions, the longitudinal field of a linearly polarized Gaussian beam is zero along the beam axis and is only nonvanishing at off-axis positions creating the two lobes at positions offset from the beam axis [58]. Actually, the application of an additional π phase delay between the two lobes of the incident HG_{10} converts our high-order beam back to a linearly-polarized beam, albeit with non-Gaussian transverse structure. Hence, its focusing properties should resemble those of an ordinary (HG_{00}) linearly-polarized Gaussian beam [74, 75]. Note, however, that switching between HG_{00} and HG_{10} would be much more cumbersome than controlling the relative phase of the lobes of a HG_{10} beam.

When the additional phase delay between the two lobes is further increased to 2π the three-lobed SHG intensity pattern with the maximum central lobe is recovered, suggesting that the longitudinal fields are again nonvanishing at the center and optimal (Fig. 5). Indeed, the behavior of longitudinal fields of focused spatially-phase shaped HG_{10} beams are reproduced well by numerical simulations based on the Debye approximation (Figure S3) [58, 76]. In the actual experiments, we used 12 additional phase delays from 0 to 2π but only show the SHG images corresponding to the intermediate phase delays of $\pi/2$ and $3\pi/2$ in Fig. 5 for clarity. We attribute the different SHG levels for the $\pi/2$ and $3\pi/2$ cases to local differences in the phase curve of the SLM which could have led to a slightly greater phase delay in practice. The observation of imbalanced SHG images for other intermediate tailored beams suggests that the strength of the longitudinal components and, more importantly, their spatial distribution at the focal plane can be manipulated at will (Fig. 6). Altogether, these results justify well the

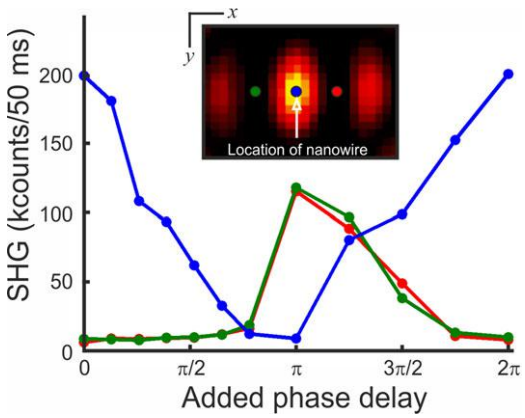

Figure 6 Variation of the SHG signal from a single vertically-aligned GaAs nanowire that is excited by a HG_{10} mode with different phase delays added to one of its lobes. The inset shows a typical raster-scanned SHG image of a GaAs nanowire that is excited by HG_{10} (along *x*) and the locations where the SHG signals were acquired. When an additional π-phase delay is added to one of the lobes, the SHG signal at the location of the nanowire is reduced as a direct consequence of the reduction of longitudinal fields at this location (blue dot). It also worth mentioning that the longitudinal fields for this beam setting (with an additional π-phase delay) were spatially redistributed as shown by the nonvanishing SHG signals at off-center locations (green and red dots).

picture of SHG light control from three-dimensional nanoobjects due to variations in the distribution of the resulting longitudinal electric fields at the focus.

It is also worth noting that the observed SHG signals in all experiments are homogenous even though the nanowires exhibit numerous stacking faults (Fig. 1d) that are known to influence the optoelectronic performance of semiconductor nanowires. This implies that the effective bulk second-order nonlinearity of the nanowires that is probed by the longitudinal fields at the focal volume remains unaltered for all cases and does not affect the reliability of the observed variations in the SHG coupling efficiency. As the form of the second-order susceptibility tensor dictates the polarization-dependent SHG response of the structure, we also expect that the SHG from semiconductor nanowires of

different symmetries, e.g., wurzite or its mixtures with zinc-blende, and of different diameters could also be exploited with vectorial fields to demonstrate additional tailoring effects [77–79]. Thus, both the effective nonlinearity within the focal volume and the focal fields are important in the optimization and subsequent tailoring of SHG from these structures.

We also note that the resolution of the SLM phase levels dictates the range of realizable field tuning parameters. The phase levels in this work were limited by the used SLM, but we anticipate that the use of more advanced SLMs will improve the tuning capability. We also emphasize that our technique will be very difficult to replicate with traditional diffractive optical elements as each distinct phase level would need a separately fabricated component, entails cumbersome alignment and will be susceptible to measurement discrepancies. In contrast, the present results show that the longitudinal field that drives the nonlinear emission from a vertically-aligned nanowire can be manipulated by simply imparting a spatial phase on a high-order input beam, being thus unhampered by any other mechanical or external complications.

4. Conclusion and outlook

We have demonstrated a technique for controlling SHG from a single and well-defined nano-object, which in our specific case was a vertically-oriented GaAs nanowire with zinc-blende structure. This was achieved by phase-shaping a high-order laser beam that drives the SHG process at the focus of a microscope objective, resulting in high contrast between the phase-dependent maxima and minima of the SHG signal strengths. Our work provides direct evidence that the longitudinal electric fields, which drive SHG from a vertically-aligned nanowire, can be controlled by spatial phase modulation. The technique is general and has direct implications to tailoring the efficiency of nanoscale sources, nonlinear imaging, nanospectroscopy, as well as arbitrary optical field control at the nanoscale.

To the best of our knowledge, our work provides the first demonstration of controlling the longitudinal field strength at the focus of a beam using a simple phase-shaping scheme. This will be crucial for future development of efficient all-optical platforms for selectively coupling light into nano-objects or molecular structures. For example, the tailored longitudinal field distributions in the focal region could be used to precisely switch and control the light coupling to two or more nearby nano-objects such as dual-type semiconductor nanowires [67], plasmonic nanowire dimers [80], coupled metal nanotubes [81] and three-dimensional nanoantennas [82]. We envisage this technique and its further developments to be useful for studying light-matter interactions that are free from any unwanted coupling between the sample and substrate thereby increasing also the sensitivity of traditional techniques such as optical encryption [15], Raman [83], and light trapping [84]. This technique could also have great potential in increasing the contrast achieved in nonlinear imaging in general. Although we have limited our study to SHG and semiconductor nanowires, we believe that other optical processes, both linear and nonlinear, in a variety of nanoscale systems [1–5, 54, 85] can also benefit from this technique. Using relevant samples that can act as optical field probes, we also expect that this technique opens an avenue towards the quantification of arbitrary focal fields in three dimensions with strong implications for studying scattering phenomena on the nanoscale. We also anticipate that our technique can be used as a basis for manipulating other complementary focal field properties such as the longitudinal magnetic field which can now be conveniently accessed by tightly focusing azimuthal polarization [86].

Supporting Information

Additional supporting information may be found in the online version of this article at the publisher's website.

Acknowledgements. This work was supported by Grants 267847 and 287651 from the Academy of Finland, the Strategy funding of the Tampere University of Technology (84010), the MOPPI project of Aalto Energy Efficiency Research Programme and the TEKES FiDiPro NP-Nano project. L.T. acknowledges the financial support from the Graduate School of Tampere University of Technology. Nanowire fabrication was performed at the Micronova Nanofabrication Centre of Aalto University. This work made use of the Aalto University Nanomicroscopy Center (Aalto-NMC) premises. This work was performed in the context of the European COST Action MP1302 Nanospectroscopy.

Received: 29 June 2016, **Revised:** 9 October 2016,
Accepted: 8 November 2016

Published online: 30 November 2016

Key words: Second-harmonic generation, nanowire, spatial light modulation, polarization, longitudinal electric field.

References

[1] P. Mühlschlegel, H.-J. Eisler, O. J. F. Martin, B. Hecht, and D. W. Pohl, Science **308**, 1607–1609 (2005).
[2] L. Novotny and N. van Hulst, Nat. Photonics **5**, 83–90 (2011).
[3] J. A. Schuller, E. S. Barnard, W. Cai, Y. C. Jun, J. S. White, and M. L. Brongersma, Nat. Mater. **9**, 193–204 (2010).
[4] M. Kauranen and A. Zayats, Nat. Photonics **6**, 737–748 (2012).
[5] M. Danckwerts and L. Novotny, Phys. Rev. Lett. **98**, 026104 (2007).
[6] H. J. Lezec, A. Degiron, E. Devaux, R. A. Linke, L. Martin-Moreno, F. J. Garcia-Vidal, and T. W. Ebbesen, Science **297**, 820–822 (2002).
[7] T. H. Taminiau, F. D. Stefani, F. B. Segerink, and N. F. van Hulst, Nat. Photonics **2**, 234–237 (2008).
[8] D. Meshulach and Y. Silberberg, Nature **396**, 239–242 (1998).

[9] N. Dudovich, D. Oron, and Y. Silberberg, Nature **418**, 512–514 (2002).
[10] M. I. Stockman, S. V. Faleev, and D. J. Bergman, Phys. Rev. Lett. **88**, 067402 (2002).
[11] M. Aeschlimann, M. Bauer, D. Bayer, T. Brixner, F. J. G. de Abajo, W. Pfeiffer, M. Rohmer, C. Spindler, and F. Steeb, Nature **446**, 301–304 (2007).
[12] O. Masihzadeh, P. Schlup, and R. A. Bartels, Opt. Lett. **34**, 1240–1242 (2009).
[13] M. R. Beversluis, L. Novotny, and S. J. Stranick, Opt. Express **14**, 2650–2656 (2006).
[14] P. Woźniak, P. Banzer, and G. Leuchs, Laser Photon. Rev. **9**, 231–240 (2015).
[15] X. Li, T.-H. Lan, C.-H. Tien, and M. Gu, Nat. Commun. **3**, 998 (2012).
[16] Z. Zheng and A. M. Weiner, Opt. Lett. **25**, 984–986 (2000).
[17] A. Shapira, R. Shiloh, I. Juwiler, and A. Arie, Opt. Lett. **37**, 2136–2138 (2012).
[18] A. Libster-Hershko, S. Trajtenberg-Mills, and A. Arie, Opt. Lett. **40**, 1944–1947 (2015).
[19] P. Wnuk, L. Le Xuan, A. Slablab, C. Tard, S. Perruchas, T. Gacoin, J.-F. Roch, D. Chauvat, and C. Radzewicz, Opt. Express **17**, 4652–4658 (2009).
[20] G. Li, S. Chen, N. Pholchai, B. Reineke, P. W. H. Wong, E. Y. B. Pun, K. W. Cheah, T. Zentgraf, and S. Zhang, Nat. Mater. **14**, 607–612 (2015).
[21] B. Gjonaj, J. Aulbach, P. M. Johnson, A. P. Mosk, L. Kuipers, and A. Lagendijk, Nat. Photonics **5**, 360–363 (2011).
[22] B. Gjonaj, J. Aulbach, P. M. Johnson, A. P. Mosk, L. Kuipers, and A. Lagendijk, Nano Lett. **12**, 546–550 (2012).
[23] E. Seo, J. Ahn, W. Choi, H. Lee, Y. M. Jhon, S. Lee, and W. Choi, Opt. Lett. **39**, 5838–5841 (2014).
[24] T. S. Kao, E. T. F. Rogers, J. Y. Ou, and N. I. Zheludev, Nano Lett. **12**, 2728–2731 (2012).
[25] J. Zhang, K. F. MacDonald, and N. I. Zheludev, Light Sci. Appl. **1**, e18 (2012).
[26] S. A. Mousavi, E. Plum, J. Shi, and N. I. Zheludev, Sci. Rep. **5**, 8977 (2015).
[27] L. Novotny, E. J. Sanchez, and X. S. Xie, Ultramicroscopy **71**, 21–29 (1998).
[28] G. Volpe, S. Cherukulappurath, R. J. Parramon, G. Molina-Terriza, and R. Quidant, Nano Lett. **9**, 3608–3611 (2009).
[29] M. Celebrano, X. Wu, M. Baselli, S. Großmann, P. Biagioni, A. Locatelli, C. De Angelis, G. Cerullo, R. Osellame, B. Hecht, L. Duò, F. Ciccacci, and M. Finazzi, Nat. Nanotechnol. **10**, 412–417 (2015).
[30] S. G. Rodrigo, H. Harutyunyan, and L. Novotny, Phys. Rev. Lett. **110**, 177405 (2013).
[31] N. Accanto, J. B. Nieder, L. Piatkowski, M. Castro-Lopez, F. Pastorelli, D. Brinks, and N. F. van Hulst, Light Sci. Appl. **3**, e143 (2014).
[32] M. H. Huang, S. Mao, H. Feick, H. Yan, Y. Wu, H. Kind, E. Weber, R. Russo, and P. Yang, Science **292**, 1897–1899 (2001).
[33] J. Wang, M. S. Gudiksen, X. Duan, Y. Cui, and C. M. Lieber, Science **293**, 1455–1457 (2001).
[34] V. Barzda, R. Cisek, T. L. Spencer, U. Philipose, H. E. Ruda, and A. Shik, Appl. Phys. Lett. **92**, 113111 (2008).
[35] H. E. Ruda and A. Shik, J. Appl. Phys. **101**, 034312 (2007).
[36] H. Kogelnik and T. Li, Appl. Opt. **5**, 1550–1567 (1966).
[37] G. Bautista, J. Mäkitalo, Y. Chen, V. Dhaka, M. Grasso, L. Karvonen, H. Jiang, M. J. Huttunen, T. Huhtio, H. Lipsanen, and M. Kauranen, Nano Lett. **15**, 1564−1569 (2015).
[38] S. Quabis, R. Dorn, M. Eberler, O. Glöckl, and G. Leuchs, Opt. Commun. **179**, 1–7 (2000).
[39] R. Dorn, S. Quabis, and G. Leuchs, Phys. Rev. Lett. **91**, 233901 (2003).
[40] K. S. Youngworth and T. Brown, Opt. Express **7**, 77–87 (2000).
[41] Q. Zhan, Adv. Opt. Photonics **1**, 1–57 (2009).
[42] D. P. Biss and T. G. Brown, Opt. Lett. **28**, 923–925 (2003).
[43] L. Novotny, M. R. Beversluis, K. S. Youngworth, and T. G. Brown, Phys. Rev. Lett. **86**, 5251–5254 (2001).
[44] A. V. Failla, H. Qian, H. Qian, A. Hartschuh, and A. J. Meixner, Nano Lett. **6**, 1374–1378 (2006).
[45] M. Fleischer, C. Stanciu, F. Stade, J. Stadler, K. Braun, A. Heeren, M. Häffner, D. P. Kern, and A. J. Meixner, Appl. Phys. Lett. **93**, 111114 (2008).
[46] E. Y. S. Yew and C. J. R. Sheppard, Opt. Commun. **275**, 453–457 (2007).
[47] G. Bautista, M. J. Huttunen, J. Mäkitalo, J. M. Kontio, J. Simonen, and M. Kauranen, Nano Lett. **12**, 3207–3212 (2012).
[48] M. J. Huttunen, K. Lindfors, D. Andriano, J. Mäkitalo, G. Bautista, M. Lippitz, and M. Kauranen, Opt. Lett. **39**, 3686–3689 (2014).
[49] G. Bautista, M. J. Huttunen, J. M. Kontio, J. Simonen, and M. Kauranen, Opt. Express **21**, 21918–21923 (2013).
[50] Q. Zhan, Opt. Express **12**, 3377–3382 (2004).
[51] M. Meier, V. Romano, and T. Feurer, Appl. Phys. A Mater. Sci. Process. **86**, 329–334 (2007).
[52] H. Ishitobi, I. Nakamura, T. Kobayashi, N. Hayazawa, Z. Sekkat, S. Kawata, and Y. Inouye, ACS Photonics **1**, 190–197 (2014).
[53] E. J. Bochove, G. T. Moore, and M. O. Scully, Phys. Rev. A **46**, 6640–6653 (1992).
[54] G. Bautista and M. Kauranen, ACS Photonics **3**, 1351–1370 (2016).
[55] E. Y. S. Yew and C. J. R. Sheppard, Opt. Express **14**, 1167–1174 (2006).
[56] M. A. Baghban and K. Gallo, APL Photonics **1**, 061302 (2016).
[57] C. J. Sheppard and S. Saghafi, Opt. Lett. **24**, 1543–1545 (1999).
[58] B. Richards and E. Wolf, Proc. R. Soc. London Ser. A **253**, 358–379 (1959).
[59] B. Sick, B. Hecht, and L. Novotny, Phys. Rev. Lett. **85**, 4482–4485 (2000).
[60] C. J. R. Sheppard and A. Choudhury, Appl. Opt. **43**, 4322–4327 (2004).
[61] J. R. Fontana and R. H. Pantell, J. Appl. Phys. **54**, 4285 (1983).
[62] G. M. Lerman, A. Yanai, and U. Levy, Nano Lett. **9**, 2139–2143 (2009).
[63] W. Chen, D. C. Abeysinghe, R. L. Nelson, and Q. Zhan, Nano Lett. **9**, 4320–4325 (2009).
[64] H. Wang, L. Shi, B. Lukyanchuk, C. Sheppard, and C. T. Chong, Nat. Photonics **2**, 501–505 (2008).
[65] J. B. Baxter and E. S. Aydil, Appl. Phys. Lett. **86**, 053114 (2005).

[66] A. K. Shalek, J. T. Robinson, E. S. Karp, J. S. Lee, D.-R. Ahn, M.-H. Yoon, A. Sutton, M. Jorgolli, R. S. Gertner, T. S. Gujral, G. MacBeath, E. G. Yang, and H. Park, Proc. Natl. Acad. Sci. U. S. A. **107**, 1870–1875 (2010).
[67] J.-P. P. Kakko, T. Haggrén, V. Dhaka, T. Huhtio, A. Peltonen, H. Jiang, E. Kauppinen, and H. Lipsanen, Nano Lett. **15**, 1679–1683 (2015).
[68] R. W. Boyd, Nonlinear Optics (Academic Press, 2008).
[69] H. He, X. Zhang, X. Yan, L. Huang, C. Gu, M.-L. Hu, X. Zhang, X. M. Ren, and C. Wang, Appl. Phys. Lett. **103**, 143110 (2013).
[70] R. Chen, S. Crankshaw, T. Tran, L. C. Chuang, M. Moewe, and C. Chang-Hasnain, Appl. Phys. Lett. **96**, 051110 (2010).
[71] A. Casadei, E. F. Pecora, J. Trevino, C. Forestiere, D. Rüffer, E. Russo-Averchi, F. Matteini, G. Tutuncuoglu, M. Heiss, A. Fontcuberta I Morral, and L. Dal Negro, Nano Lett. **14**, 2271–2278 (2014).
[72] R. Grange, G. Brönstrup, M. Kiometzis, A. Sergeyev, J. Richter, C. Leiterer, W. Fritzsche, C. Gutsche, A. Lysov, W. Prost, F. J. Tegude, T. Pertsch, A. Tünnermann, and S. Christiansen, Nano Lett. **12**, 5412–5417 (2012).
[73] A. Bouhelier, M. Beversluis, A. Hartschuh, and L. Novotny, Phys. Rev. Lett. **90**, 013903 (2003).
[74] G. Machavariani, N. Davidson, A. A. Ishaaya, A. A. Friesem, and E. Hasman, Opt. Lett. **27**, 1501–1503 (2002).
[75] A. A. Ishaaya, G. Machavariani, N. Davidson, A. A. Friesem, and E. Hasman, Opt. Lett. **28**, 504–506 (2003).
[76] S. N. Khonina and S. G. Volotovsky, J. Opt. Soc. Am. A **27**, 2188–2197 (2010).
[77] M. Timofeeva, A. Bouravleuv, G. Cirlin, I. Shtrom, I. Soshnikov, M. Reig Escalé, A. Sergeyev, and R. Grange, Nano Lett. (2016) DOI: 10.1021/acs.nanolett.6b02592.
[78] R. Sanatinia, M. Swillo, and S. Anand, Nano Lett. **12**, 820–826 (2012).
[79] R. Sanatinia, S. Anand, and M. Swillo, Nano Lett. **14**, 5376–5381 (2014).
[80] G. Toscano, S. Raza, A.-P. Jauho, N. A. Mortensen, and M. Wubs, Opt. Express **20**, 4176–4188 (2012).
[81] P. Zilio, M. Malerba, A. Toma, R. Zaccaria, A. Jacassi, and F. De Angelis, Nano Lett. **15**, 5200–5207 (2015).
[82] D. Dregely, R. Taubert, J. Dorfmüller, R. Vogelgesang, K. Kern, and H. Giessen, Nat. Commun. **2**, 267 (2011).
[83] R. La Rocca, G. C. Messina, M. Dipalo, V. Shalabaeva, and F. De Angelis, Small **11**, 4632–4637 (2015).
[84] W. Zhou and T. W. Odom, Nat. Nanotechnol. **6**, 423–427 (2011).
[85] G. Kurizki, M. Shapiro, and P. Brume, Phys. Rev. B **39**, 3435 (1989).
[86] M. Kasperczyk, S. Person, D. Ananias, L. D. Carlos, and L. Novotny, Phys. Rev. Lett. **114**, 163903 (2015).

II

Nonlinear imaging of nanostructures using beams with binary phase modulation

by
Léo Turquet, Joona-Pekko Kakko, Hua Jiang, Tero J. Isotalo, Teppo Huhtio, Tapio Niemi, Esko Kauppinen, Harri Lipsanen, Martti Kauranen, and Godofredo Bautista, 2017
Optics Express, vol. 25, pp. 10441-10448

III

Probing the longitudinal electric field of Bessel beams using second-harmonic generation from nano-objects

by
Léo Turquet, Joona-Pekko Kakko, Lasse Karvonen, Hua Jiang, Esko Kauppinen,
Harri Lipsanen, Martti Kauranen, and Godofredo Bautista, 2017
Journal of Optics, vol. 19, p. 084011

IV

Demonstration of longitudinally polarized optical needles

by
Léo Turquet, Xiaorun Zang, Joona-Pekko Kakko, Harri Lipsanen, Godofredo Bautista, and Martti Kauranen, 2018
Optics Express, vol. 26, pp. 27572-27584

Tampereen teknillinen yliopisto
PL 527
33101 Tampere

Tampere University of Technology
P.O.B. 527
FI-33101 Tampere, Finland

ISBN 978-952-15-4242-8
ISSN 1459-2045